Theoretical Calculations of Excited States and Fluorescence Spectroscopy using Density Functional Theory

Edward A. Briggs, MSci

Thesis submitted to the University of Nottingham for the degree of Doctor of Philosophy

June 2016

Abstract

Absorption and emission spectra from the lowest energy transition in BODIPY have been simulated in the gas and water phase using a quantum mechanics/molecular mechanics approach, with DFT and the maximum overlap method (MOM). A post-SCF spin-purification to MOM yields transition energies in agreement with experimental data. Spectral bands were simulated using structures from *ab initio* molecular dynamics simulations, in which the solvent water molecules are treated classically and DFT is used for BODIPY. The resulting spectra are consistent with experimental data, and demonstrate how absorption and emission spectra in solution can be simulated using a quantum mechanical treatment of the solute.

The electronic structure and photoinduced electron transfer (PET) processes in a fluorescent K^+ sensor have been studied using DFT and TDDFT to rationalise its function. Absorption and emission energies of the fluorophore-localised intense excitation are more accurately described using MOM than TDDFT. Analysis of molecular orbital energies from DFT calculations in different phases cannot account for the sensors function. It is necessary to consider the relative energies of the electronic states. The inclusion of implicit solvent lowers the energy of the charge transfer state making a reductive PET possible in the absence of K^+, while no such process is possible when the sensor is bound to K^+.

Binding within the ethene–argon and formaldehyde–methane complexes in ground and electronically excited states is studied with equations of motion coupled-cluster theory (EOM-CCSD), MP2 theory and dispersion-corrected DFT (DFT-D). MP2/MOM potential energy curves are in good agreement with EOM-CCSD calculations for the Rydberg and valence states studied. B3LYP-D3 calculations are in agreement with EOM-CCSD for ground and valence excited states, however for Rydberg states significant deviation is observed for a variety of DFT-D methods. Varying D2 dispersion parameters results in closer agreement with EOM-CCSD for Rydberg states.

Published Work

The work presented in this thesis has been published in part in the following refereed papers.

1. "QM/MM Excited State Molecular Dynamics and Fluorescence Spectroscopy of BODIPY"

   Edward A. Briggs, Nicholas A. Besley and David Robinson

   Journal of Physical Chemistry A, **117,** *12,* 2644-2650 (2013).

2. "Modelling Excited States of Weakly Bound Complexes with Density Functional Theory"

   Edward A. Briggs and Nicholas A. Besley

   Physical Chemistry Chemical Physics, **16,** *28,* 14455-14462 (2014).

3. "Density Functional Theory Based Analysis of Photoinduced Electron Transfer in a Triazacryptand based K^+ Sensor"

   Edward A. Briggs and Nicholas A. Besley

   Journal of Physical Chemistry A, **119,** *12,* 2902-2907 (2015).

4. "Unusual Spectroscopic and Photophysical Properties of meso-tert-butyl BODIPY in Comparison to Related Alkylated BODIPY Dyes"

   Lijuan Jiao, Changjiang Yu, Jun Wang, **Edward A. Briggs,** Nicholas A. Besley, David Robinson, María J. Ruedas-Rama, Angel Orte, Luis Crovetto, Eva M. Talavera, Jose M. Alvarez-Pez, Mark Van der Auweraerd and Noël Boens

   RSC Advances, **109,** *5,* 89375-89388 (2015).

Acknowledgements

I would like to thank Dr. Nick Besley for all of his help, support and guidance during my research, as well as Dr. David Robinson for his collaboration on the BODIPY work. I would also like to thank the Engineering and Physical Science Research Council (EPSRC) for their funding, and to the University of Nottingham for access to their High Performance Computing service. Finally I would like to thank my wife, Lauren, for her continued patience and support over the last four years.

List of Figures

List of Tables

Contents

1. Introduction

The work discussed in this thesis covers an in depth discussion of computational studies of electronically excited states and fluorescence spectroscopy using density functional theory, with later work detailing the weak interaction of excited states modelled using density functional theory. There are four main sections; firstly a detailed outline of the background theory to the computational methods covering a wide variety of methods used in the three main projects, outlining the history and methodology, along with how the various methods have been applied to the following work. This is followed by three chapters describing the work undertaken since commencing PhD studies, split into three distinct projects:

1. Quantum Mechanics/ Molecular Mechanics (QM/MM) Excited State Molecular Dynamics and Fluorescence Spectroscopy of BODIPY.
2. Density Functional Theory Based Analysis of Photoinduced Electron Transfer in a Triazacryptand based Potassium Ion (K^+) Sensor.
3. Modelling Excited States of Weakly Bound Complexes with Density Functional Theory Density Functional Theory.

The focus of the first project was to model the absorption and emission spectroscopy of the boron dipyrromethene fluorophore, commonly abbreviated to BODIPY, using theoretical methods. BODIPY is a fluorophore with a wide variety of practical applications, due to the tunability of photochemical and physical properties seen in BODIPY-containing derivatives. This is possible due to BODIPY's chemical structure, as substitution of a variety of moieties is possible at various positions on the molecule [1], which influences its fluorescent properties. Although the BODIPY fluorophore has been the subject of many experimental and synthetic studies, there has been little work

into calculating the absorption and emission spectra of BODIPY using quantum chemical methods. This work aimed to model the absorption and emission bands of the BODIPY fluorophore. Firstly, the structures of the BODIPY fluorophore along with several BODIPY derivatives were studied using density functional theory and complete active space second-order perturbation theory, along with the excitation energies using density functional methods. Density functional theory in conjunction with *ab initio* molecular dynamics was then used to generate multiple ground state and excited state structures, from which absorption and emission bands for the BODIPY fluorophore were calculated, in both the gas phase and solvent phase. Most of this work has been published in the *Journal of Physical Chemistry A*, with some of the structural analysis for *meso*-BODIPY derivatives presented as a part of a larger study published in *RSC Advances.*

The second project continues the theme of studying fluorescence of a molecule through density functional theory and other quantum chemical methods, with the focus of modelling photoinduced electron transfer (PET) in a potassium cation sensor. The potassium cation (K^+) is the most abundant intracellular ion in the human body, and is essential for maintaining good health. Chemically sensing K^+ within cells is therefore highly important, and one such sensor is a triazacryptand-based fluorescent sensor referred to as KS1 [2]. KS1 is a selective potassium cation sensor, with its relative fluorescence activity in the presence of K^+ being linked to a PET process. This work has set out to further study this process in the KS1 sensor, primarily using density functional theory with a range of functionals. The nature and energies of the relevant electronic states involved in fluorescence and charge-transfer processes were assessed, to determine whether PET occurs and under what conditions. This was done in two ways, firstly assessing the relative energies of the molecular orbitals of KS1, and

secondly by directly calculating the energies of relevant states using excited state density functional methods. This work has been published in the *Journal of Physical Chemistry A*.

The third project has a slightly different focus than the first two areas of interest, as it does not involve fluorescence spectroscopy, however the work still centres on the main theme of calculating excited states using density functional theory. Dispersion forces, where the dipole of one molecule induces a dipole on another molecule causing weak binding in non-polar systems, is not modelled correctly in standard exchange-correlation functionals using density functional theory. Several empirical additions to standard density functional energies have been suggested [3, 4], although these are parameterised for the electronic ground state. This work has looked at assessing the effectiveness of these methods when applied to an electronic excited state, by studying the binding energies in two weakly bound systems: ethene-argon and formaldehyde-methane. The binding in the ground state was compared with both valence and Rydberg states, using a variety of density functional methods and dispersion corrections, as well as highly accurate wavefunction-based quantum chemical methods. This work has been published in *Physical Chemistry Chemical Physics*.

2. Overview of Theoretical Methods

This chapter describes in detail the theoretical and computational methods encountered throughout this work. This includes the *ab initio* method Hartree-Fock theory, the post-Hartree-Fock methods Møller-Plesset perturbation theory and coupled cluster theory, complete active space perturbation theory and density functional theory. Also covered are the excited state methods time-dependent density functional theory and quantum mechanics/molecular mechanics (QM/MM) approaches used to study the systems in solution. The work comprising this chapter has been based on a number of sources, including:

- Levine, I. N. *Quantum Chemistry*, Pearson, 6th edn, **2008.**
- *Q-Chem User's Manual,* Version 4.1, **2013.**
- *The Sherrill Group Notes*, (http://vergil.chemistry.gatech.edu/notes/).

2.1. The Quantum Mechanical Approach

Properties of a molecular system over time can be defined using the time-dependent Schrödinger equation (2.1), where ħ is the reduced Planck constant ($\hbar = h / 2\pi$), t is time, Ψ is the system's wave function and $\hat{H}$ the Hamiltonian operator. i describes an imaginary unit.

$$i\hbar \frac{\partial}{\partial t} \Psi = \hat{H} \Psi \tag{2.1}$$

For situations where the Hamiltonian is not time-dependent, the system can then be described as stationary states of defined energies. In this case the time-independent Schrödinger equation (2.2) can be applied.

$$\hat{H}(\boldsymbol{r}) \Psi(\boldsymbol{r}) = E \Psi(\boldsymbol{r}) \tag{2.2}$$

Where $\boldsymbol{r}$ describes the coordinate vector of the system and E is the total energy of the system. The solutions to the time-independent Schrödinger equation for a system can be used to obtain that system's stationary state wavefunctions $\Psi_n(\boldsymbol{r})$ and energies E_n, which correspond to the different energy levels of a system. The lowest energy solution to Eq. (2.2) is known as the ground state, and higher energy solutions are excited states. To solve Eq. (2.2) one must first know the Hamiltonian operator of the system $\hat{H}$.

The Hamiltonian operator performs operations on the wavefunction of a system to give its energy, and therefore consists of both kinetic energy $(\hat{T})$ and potential energy $(\hat{V})$ terms. For an atomic and molecular system the Hamiltonian can be separated into these two terms as shown in Eq. (2.3), where $\hat{T}$ and $\hat{V}$ can be expressed as shown in Eqs. (2.4) and (2.5).

$$\hat{H} = \hat{T} + \hat{V} \tag{2.3}$$

$$\hat{T} = -\frac{1}{2}\sum_{A}\frac{1}{m_A}\nabla_A^2 - \frac{1}{2}\sum_{i}\nabla_i^2 \tag{2.4}$$

$$\hat{V} = \sum_{A>B}\frac{Z_A Z_B}{r_{AB}} - \sum_{Ai}\frac{Z_A}{r_{Ai}} + \sum_{i>j}\frac{1}{r_{ij}} \tag{2.5}$$

The terms of Eq. (2.4) describe the kinetic energy of a molecular system where A corresponds to a nucleus in the system, i to an electron in the system, and m_A to the mass of the nucleus A. As atomic units are used, the electron mass is equal to 1. For the potential energy equation (2.5), A and B describe atoms in the system, i and j electrons, and Z the charge of the nuclei. Relativistic effects are often ignored, as they are negligible for lighter elements of the periodic table. It is possible to consider relativistic effects for heavier elements, however in this thesis they are not relevant to the work undertaken. The parameters included in Eqs. (2.4) and (2.5) can be combined to give a complete molecular Hamiltonian (Eq. 2.6).

$$\hat{H} = -\frac{1}{2}\sum_{A}\frac{1}{m_A}\nabla_A^2 - \frac{1}{2}\sum_{i}\nabla_i^2 + \sum_{A>B}\frac{Z_A Z_B}{r_{AB}} - \sum_{Ai}\frac{Z_A}{r_{Ai}} + \sum_{i>j}\frac{1}{r_{ij}} \tag{2.6}$$

Since the nuclei of atomic systems are much heavier than electrons (a single proton is nearly 2000 times the mass of an electron) it is possible to use the Born-Oppenheimer approximation [5] and assume that the motion of a nucleus compared to an electron is so slow it is essentially fixed in position with respect to an electron. This allows the total wavefunction Ψ_{tot} to be split into separate nuclear Ψ_n and electronic Ψ_e wavefunctions,

$$\Psi_{tot}(\boldsymbol{R}, \boldsymbol{r}) = \Psi_e(\boldsymbol{R}, \boldsymbol{r})\Psi_n(\boldsymbol{R}) \tag{2.7}$$

Where $\boldsymbol{R}$ and $\boldsymbol{r}$ correspond to the spatial coordinate vector of the nuclei and electrons respectively. This allows the Hamiltonian to also be split into nuclear and electronic terms (Eq. 2.8), which gives an electronic Hamiltonian (Eq. 2.9) where the kinetic

energy of the nuclei is not included and the nuclear-nuclear repulsion $\hat{V}_{nn}$ is constant, and a separate nuclear Hamiltonian term $\hat{T}_n$ describes nuclear kinetic energy.

$$\hat{H}_{tot} = \hat{H}_e + \hat{T}_n + \hat{V}_{nn} \tag{2.8}$$

$$\hat{H}_e = -\frac{1}{2}\sum_i \nabla_i^2 - \sum_{Ai} \frac{Z_A}{r_{Ai}} + \sum_{i>j} \frac{1}{r_{ij}} \tag{2.9}$$

$$\hat{T}_n = -\frac{1}{2}\sum_A \frac{1}{m_A} \nabla_A^2 \tag{2.10}$$

This leads to an electronic Schrödinger equation (2.11) with the nuclear part shown in Eq. (2.12).

$$\hat{H}_e \hat{\Psi}_e(\boldsymbol{R}, \boldsymbol{r}) = E_e(\boldsymbol{R}) \Psi_e(\boldsymbol{R}, \boldsymbol{r}) \tag{2.11}$$

$$(\hat{T}_n + E_e(\boldsymbol{R})) \hat{\Psi}_n(\boldsymbol{R}) = E_{tot} \Psi_n(\boldsymbol{R}) \tag{2.12}$$

The electronic Schrödinger equation can then be used to find the potential energy surface (PES) of an atomic or molecular system, although for most systems calculations are restricted to energy minima and other low energy pathways. These energy minima correspond to nuclear positions that result in stable structures of a system, whereas low energy pathways between minima can allow study of chemical reactions. Sometimes the shape of all or part of a PES is of interest of whether it is of low energy for the system. In chapter 5 of this thesis the specifying of nuclear coordinates to obtain a potential energy curve for atom and molecule pairs will be studied.

Although the electronic Schrödinger equation should give exact results for the electronic energy of a molecular system, for any atom or molecule with more than one electron, solving Eq. (2.11) is impossible, due to the electron-electron interaction term which explicitly couples the motion of the electrons, requiring the separation distance of electrons which cannot be calculated. There are many theories developed that deal

with approximating the solution to Eq. (2.11), many based upon the Hartree-Fock method.

2.2. Hartree-Fock Theory

Hartree-Fock (HF) theory is a method that was developed to solve the electronic Schrödinger equation for systems (Eq. 2.11) with more than one electron [6, 7]. As the solutions to HF calculations are calculated without using any experimental or empirical data apart from fundamental constants, it is known as an *ab initio* method, Latin for *'from the beginning'*. The first component of the electronic Schrödinger equation to be looked at will be the wavefunction. The HF wavefunction is an approximate wavefunction of the ground state of an atomic or molecular system, known as a Slater determinant [8].

The Pauli principle asserts that the total wavefunction for two electrons is antisymmetric with respect to exchange of the electrons. This means the Slater determinant must change sign with exchange of electrons. This can be explained easily through the example of a two-electron system, where one could assume combining the product of single particle wavefunctions with their respective spatial coordinates will give the correct electronic wavefunction. This is shown in Eq. (2.13) and is known as the Hartree product. However, this is not the correct way to express the electronic wavefunction as it is not antisymmetric with respect to electron exchange. To make the overall electronic wavefunction satisfy the Pauli principle (2.14), one must take the linear combination of the original Hartree product and the Hartree product with electrons exchanged (2.15).

$$\Psi_e(1,2) = \psi_1(1)\psi_2(2) \tag{2.13}$$

$$\Psi_e(1,2) = -\Psi_e(2,1) \tag{2.14}$$

$$\Psi_e(1,2) = \frac{1}{\sqrt{2!}}\{\psi_1(1)\psi_2(2) - \psi_1(2)\psi_2(1)\} \tag{2.15}$$

$$\Psi_e(1,2) = \frac{1}{\sqrt{2!}}\begin{vmatrix}\psi_1(1) & \psi_2(1)\\ \psi_1(2) & \psi_2(2)\end{vmatrix} \tag{2.16}$$

This gives the determinant presented in (2.16) which can be expanded to an N electron system as shown in Eq. (2.17), where N is the number of electrons in a system, ψ_1 through to ψ_N are one electron molecular orbitals and (1) through to (N) are the spatial coordinates of the electrons.

$$\Psi_{SD} = \frac{1}{\sqrt{N!}}\begin{vmatrix}\psi_1(1) & \psi_2(1) & \cdots & \psi_N(1)\\ \psi_1(2) & \cdots & \cdots & \cdots\\ \cdots & \cdots & \cdots & \cdots\\ \psi_1(N) & \psi_2(N) & \cdots & \psi_N(N)\end{vmatrix} \tag{2.17}$$

The one electron molecular orbitals in the Slater determinant are known as *spin* orbitals, which are products of a spatial orbital with coordinates x, y, z and a spin function α or β with a spin coordinate ω. For the *i*-th molecular orbital depending on the coordinates of the *k*-th electron the form of the molecular orbital is as follows,

$$\psi_i(k) = \psi_i^{\alpha}(\boldsymbol{r}_k)\alpha(\omega_k) \tag{2.18}$$

where $\boldsymbol{r}_k$ describes the spatial coordinates of electron k in spatial orbital ψ_i^{α}, and the spin coordinate ω_k corresponds to the α spin function.

The atomic or molecular energy of a system can be given by expressing in terms of the total wavefunction, Ψ, and is calculated by integrating the product of the complex conjugate of the wavefunction Ψ^* with respect to three spatial coordinates and one spin coordinate for each electron. The time-independent Schrödinger equation (2.2) then takes the form seen in (2.19) and (2.20), where $d\tau$ represents the integration over all space and the spin coordinate.

$$E \int \Psi^* \Psi \, d\tau = \int \Psi^* \hat{H} \Psi \, d\tau \tag{2.19}$$

$$E = \frac{\int \Psi^* \hat{H} \Psi \, d\tau}{\int \Psi^* \Psi \, d\tau} \tag{2.20}$$

As the wavefunctions are normalised, $\int \Psi^* \Psi \, d\tau$ in Eq. (2.20) is equal to one, which means it can be rewritten in the more simple form of

$$E = \int \Psi^* \hat{H} \Psi \, d\tau \tag{2.21}$$

or using Dirac's notation for integrals it can be expressed as

$$E = \langle \Psi | \hat{H} | \Psi \rangle \tag{2.22}$$

Looking back at the electronic Hamiltonian in Eq. (2.9) it can be further separated into one-electron and two-electron terms, giving separate one- and two-electron Hamiltonians $h(i)$ and $v(i,j)$ where

$$h(i) = -\frac{1}{2}\nabla_i^2 - \sum_A \frac{Z_A}{r_{Ai}} \tag{2.23}$$

$$v(i,j) = \frac{1}{r_{ij}} \tag{2.24}$$

This allows the electronic Hamiltonian to be rearranged into a more simple form and have the nuclear-nuclear repulsion term V_{nn} (a constant) added to form the total Hamiltonian for an *N*-electron system, which can be presented as seen in (2.25). From this it is possible to solve the one-electron, two-electron and nuclear repulsion terms separately. The nuclear repulsion terms are assumed constant due to invoking the Born-Oppenheimer approximation. For the one-electron term for an electron *i* at position ***r*** the energy E_i is simply evaluated as a sum of one-electron integrals as it appears in Eq. (2.26)

$$\hat{H}_e = \sum_i^N h(i) + \sum_{i>j}^N v(i,j) + V_{nn} \tag{2.25}$$

$$E_i = \langle \psi_i | h(i) | \psi_i \rangle = \int \psi_i^* (\boldsymbol{r}) \left(-\frac{1}{2}\nabla_i^2 - \sum_A \frac{Z_A}{r_{Ai}} \right) \psi_i(\boldsymbol{r}) d\boldsymbol{r} \tag{2.26}$$

For the two electron terms with electrons i and j with positions $\boldsymbol{r}_1$ and $\boldsymbol{r}_2$ the energy is more complicated and is a sum of two different values; the Coulomb energy and the exchange energy. The Coulomb energy is evaluated as a sum of Coloumb integrals (for more than two electrons in a system) and the exchange energy is a sum of exchange integrals. The Coulomb integral takes the form

$$(ii|jj) = \int \int \frac{\psi_i^*(\boldsymbol{r}_1)\psi_i(\boldsymbol{r}_1)\psi_j^*(\boldsymbol{r}_2)\psi_j(\boldsymbol{r}_2)}{r_{12}} d\boldsymbol{r}_1 d\boldsymbol{r}_2 \tag{2.27}$$

and represents a positive contribution of energy (destabilisation) of a system due to electron-electron Coulombic repulsion. For an electron pair ij (2.27) represents an electron i at position $\boldsymbol{r}_1$ interacting with electron j at position $\boldsymbol{r}_2$. The exchange integrals are more complicated and take the form:

$$(ij|ij) = \int \int \frac{\psi_i^*(\boldsymbol{r}_1)\psi_j(\boldsymbol{r}_1)\psi_j^*(\boldsymbol{r}_2)\psi_i(\boldsymbol{r}_2)}{r_{12}} d\boldsymbol{r}_1 d\boldsymbol{r}_2 \tag{2.28}$$

The exchange integrals, unlike the Coulomb integrals, do not have a classical representation and refer to the exchange of electrons. It is possible now to write the HF energy as Eq. (2.29), in terms of the one- and two-electron terms.

$$E = \sum_i^N E_i + \sum_{i>j}^N \{(ii|jj) - (ij|ij)\} + V_{nn} \tag{2.29}$$

The Coulomb and exchange integrals can be rewritten as Coulomb and exchange operators that are often referred to as $\hat{J}$ and $\hat{K}$ respectively, and take the form seen in Eqs. (2.30) and (2.31).

$$\hat{J}\psi_i(\boldsymbol{r}_1) = \sum_j \int \frac{\psi_j^*(\boldsymbol{r}_2)\psi_j(\boldsymbol{r}_2)}{r_{12}} d\boldsymbol{r}_2 \psi_i(\boldsymbol{r}_1) \tag{2.30}$$

$$\hat{K}\psi_i(\boldsymbol{r}_1) = \sum_j \int \frac{\psi_j^*(\boldsymbol{r}_2)\psi_i(\boldsymbol{r}_2)}{r_{12}} d\boldsymbol{r}_2 \psi_j(\boldsymbol{r}_1) \tag{2.31}$$

This leads to a more convenient form of the HF energy from Eq. (2.29):

$$E = \sum_i^N E_i + \frac{1}{2}\sum_i^N \langle \psi_i | \hat{J} - \hat{K} | \psi_i \rangle \tag{2.32}$$

Now that the HF energy has been defined in terms of one- and two-electron terms, it must be made possible to solve in a computationally efficient way. First it is worth noting that HF theory follows the variational principle, which states that *energy calculated from the form seen in* (2.22) *must be either greater than or equal to the lowest energy solution (true ground-state energy) of the molecule.* This means any ground state energy calculated with the methods previously described in this section must be greater than or equal to the true energy of the molecule. This means the lower the energy calculated by the HF method the closer to the true value it is. The HF method aims to find the set of orbitals that minimise the energy to the lowest value.

Using the previous equations and the variational principle, the HF equations can be written as a set of one electron equations of the form

$$\hat{F}\psi_i(\boldsymbol{r}) = \varepsilon_i \psi_i(\boldsymbol{r}) \tag{2.33}$$

where ε_i are orbital energies and $\hat{F}$ is the Fock operator, which is an effective one-electron operator and takes the form of the one electron operators encountered in Eq. (2.29) to give

$$\hat{F}(1) = h(1) + \hat{J} - \hat{K} \tag{2.34}$$

These HF equations presented in Eq. (2.33) are known as pseudoeigenvalue equations, which means they take the form of an eigenvalue equation, where the Fock operator acts on a wavefunction to generate an energy value multiplied by the wave function. This is analogous to the time-independent Schrödinger equation (2.2). It is known as a pseudoeigenvalue equation because the Fock operator is not dependent on the wavefunction on which it acts. It can, however, be solved like a regular eigenvalue problem.

The HF equations allow the molecular orbitals ψ to be calculated as well as their energy levels ε. The HF method begins with 'guesses' of the molecular orbitals, which allows the Fock operator $\hat{F}$ to be constructed. The initial Fock operator can then operate on the guess molecular orbitals to give an approximate solution for the energy levels ε and thus new functions for improved molecular orbitals. This process can continue to minimise the energy until the energies and molecular orbitals converge to a certain degree of accuracy between iterations. This final pair of solutions is known as 'self-consistent', and allows a minimum energy to be obtained from an initial guess of molecular orbitals.

Although calculating the properties of an atomic or molecular system seems more viable at this point, the HF equations are not directly calculable due to the final converged orbitals being based on the 'guess' orbitals, the wavefunctions of which would be too complicated to calculate when considering molecular orbitals. As there are no appropriate templates for these molecular orbitals to be based on, it is possible to calculate close approximations of the molecular orbitals of a system by representing them as a linear combination of functions known as basis functions. This was first postulated by Roothan and Hall [9, 10]. These basis functions are usually based on

atomic orbitals, therefore this method is known as the linear combination of atomic orbitals (LCAO) approach and takes the following form:

$$\psi_i = \sum_{\alpha}^{N_b} c_{\alpha i}\, \chi_\alpha \tag{2.35}$$

where ψ_i describes the *i*-th molecular orbital in a system, $c_{\alpha i}$ is the coefficient corresponding to the α-th basis function of the molecular orbital and χ_α represents the α-th basis function. N_b is the total number of basis functions, which depends on the collection of specific basis functions being used, known as a basis set. Basis sets will be discussed further in section **2.3**.

Using the LCAO approach to forming molecular orbitals it is possible to combine with the HF equations (2.33) to give the following equation.

$$\sum_{\alpha}^{N_b} c_{\alpha i}\, \hat{F} \chi_\alpha = \varepsilon_i \sum_{\alpha}^{N_b} c_{\alpha i}\, \chi_\alpha \tag{2.36}$$

As the values $c_{\alpha i}$ are coefficients, F only operates on the basis functions χ_α, it is possible to multiply Eq. (2.36) by the basis function χ_β

$$\sum_{\alpha=1}^{N_b} c_{\alpha i}\, \chi_\beta \hat{F} \chi_\alpha = \varepsilon_i \sum_{\alpha=1}^{N_b} c_{\alpha i}\, \chi_\beta \chi_\alpha \tag{2.37}$$

and integrate,

$$\sum_{\alpha=1}^{N_b} c_{\alpha i} \left\langle \chi_\beta \middle| \hat{F} \middle| \chi_\alpha \right\rangle = \varepsilon_i \sum_{\alpha=1}^{N_b} c_{\alpha i} \left\langle \chi_\beta \middle| \chi_\alpha \right\rangle \tag{2.38}$$

which can be rewritten as

$$\sum_{\alpha=1}^{N_b} c_{\alpha i} \left(F_{\beta\alpha} - \varepsilon_i S_{\beta\alpha} \right) = 0 \tag{2.39}$$

where

$$F_{\beta\alpha} = \langle \chi_\beta | \hat{F} | \chi_\alpha \rangle \tag{2.40}$$

and

$$S_{\beta\alpha} = \langle \chi_\beta | \chi_\alpha \rangle \tag{2.41}$$

$S_{\beta\alpha}$ describes the overlap between basis functions, and is known as the overlap integrals. It is possible to rewrite Eq. (2.39) in matrix notation to give the form Eq. (2.42), where **F** is the Fock matrix, **C** is the coefficient matrix containing the basis function coefficients, **S** is the basis function's overlap matrix and ε is a diagonal matrix of the orbital energies of a system.

$$\mathbf{FC} = \mathbf{SC}\varepsilon \tag{2.42}$$

Solving this matrix problem requires the use of basis functions and their coefficients, as well as molecular orbital energy levels. Using a known basis set of basis functions it is possible to calculate the coefficients and therefore the molecular orbitals of the system ψ and their energy levels. These wavefunctions produce a Slater determinant which can be used to calculate the properties of the whole system defined by Ψ. This method follows the Self-Consistent Field (SCF) method outlined earlier, which is explained in more details in the following steps:

1. Obtain an initial guess of the orbitals using the coefficients $c_{\alpha i}$.
2. Calculate the necessary integrals for the system and form a Fock matrix and overlap matrix from these integrals.
3. Solve the Roothan-HF equations according to Eqs. (2.39) and (2.42) to give a new set of molecular orbitals.

4. Test for convergence according to a set of restraints, or convergence limit, which can be varied depending on the calculation method and the degree of accuracy required.
5. If convergence criteria have not been met, the calculation takes the new MOs and applies them to step 2, repeating steps 2-4 until the convergence limit is met.

Each step towards convergence in a HF calculation solves the Roothan-Hall equations, Eq. (2.39), which forms spatial molecular orbitals from N_b basis functions. This number of basis functions can vary from a minimum, which is equal to the number of doubly occupied MOs in the system, to effectively an infinite amount. The amount of basis functions can greatly affect the computational cost of these calculations, and one using these methods should always choose a basis set appropriate to the needs of the calculations. A more thorough description of basis sets can be found in section **2.3**. The most computationally expensive part of the SCF procedure outlined above is the evaluation of the two-electron Coulomb and exchange integrals, equations (2.30) and (2.31), due to these integrals having to be evaluated for all possible electron pairs in a system. This results in N_b^4 integrals in total which means Hartree-Fock calculations scale with the number of basis functions to the degree of N_b^4. This results in any system increasing in computational expense by 16 times for either doubling the size of the system within the same basis set, or doubling the number of basis functions in a basis set. Methods to speed up HF calculations, such as integral screening where not all integrals are evaluated, can lead to improved computational efficiency, however increasing the size of a system still increases computational expense. This scaling results in calculations on large systems becoming very computationally demanding, therefore most HF calculations are restricted to molecular systems no larger than around 100 atoms, although more is certainly possible.

One major drawback of HF theory is its inability to properly model electron-electron repulsion. The repulsion between electrons is included by having each electron move in an average electronic field with respect to the other electrons in the system. This means the probability of an electron being in one area in the system is only dependent on the average positions of other electrons. This, in theory, allows electrons in HF theory to be very close to each other. In reality, electron repulsion of one electron would cause the average electron cloud of the other electrons to change, so electrons would not occupy space close to one another. This results in HF theory modelling systems where the electrons on average are too close to one another, giving a value of electron-electron repulsion too large with respect to the real system, leading to an overestimation of energies in HF calculations. This error is known as the correlation energy and is represented as:

$$E_C = E_{EXACT} - E_{HF} \tag{2.43}$$

where E_C is the correlation energy, E_{EXACT} is the exact energy of the system within the basis set and E_{HF} is the calculated Hartree-Fock energy for a given basis set. As the correlation energy is usually too important to be neglected, HF alone is often not accurate enough and so-called post-Hartree-Fock (post-HF) methods must be employed, such as second-order Møller-Plesset perturbation theory (MP2) and coupled-cluster (CC) methods, which will be detailed in sections **2.4** and **2.5** respectively. Alternatively one can use other methods such as density functional theory (section **2.6**).

The HF method outlined above seeks to find energies and wavefunctions corresponding to closed-shell, ground state molecules, and the resulting Slater determinant applies to molecules where the electrons fill the lowest energy levels first, doubly occupying the molecular orbitals with opposing spin electrons. Systems are in an electronically excited state when one or more electrons have been moved into a higher energy molecular

orbital than its ground state occupancy. Methods to deal with quantum chemical calculations of excited state systems are described in section **2.7**. There are two main methods of applying HF theory to a molecule. Firstly, restricted Hartree-Fock, or RHF, studies closed-shell Slater determinants, and restricts electrons of different spins (α and β) to the same set of spatial orbitals. Unrestricted Hartree-Fock, or UHF, uses separate spatial orbitals for electrons with different spins, which gives two sets of molecular orbitals for a system. UHF is commonly used in conjunction with methods which study electronically excited states, such as the maximum overlap method (section **2.7.2**). The HF method, along with many other quantum chemical methods such as post-HF methods and density functional theory, rely on basis functions, which are defined as a collection of known functions known as basis sets.

2.3. Basis Sets

As described in Eq. (2.32), molecular orbitals for a system can be modelled as a linear combination of atomic orbitals, modelled as basis functions. These basis functions are mathematical functions, and can vary in their accuracy and computational cost of the resulting calculation. A defined set of these basis functions is known as a basis set.

There are several types of functions that can be used as basis functions to model electron distribution, and they often exist as a function of the radial behaviour of an electron with respect to the distance from an atomic nucleus. Functions can be directly based on the solution to the Schrödinger equation for hydrogen, as well as plane waves, Slater functions and Gaussian functions. As the Slater and Gaussian functions are the simplest variants whilst still providing a fairly accurate representation of atomic electron distribution, combinations of these functions are often used to form basis sets.

Slater functions provide a near-ideal representation of the radial distribution of electrons, and take the form $e^{-\alpha r}$ where α is a constant and r the radial distance. While accurate, Slater functions are not often used for *ab initio* methods, due to the high computational expense of calculating the two-electron integrals using Slater functions. Gaussian functions, on the other hand, provide a much easier function to calculate these two electron integrals from. Gaussian functions have the form $e^{-\alpha r^2}$ and can provide an approximation to the more accurate Slater functions. However, a single Gaussian function can differ significantly from the equivalent Slater function at short and long range, and on its own is a poor representation of the Slater function.

It is still possible to model a Slater type function using Gaussian functions, and this due to the idea of contracted basis functions. These involve the linear combination of several

Gaussian functions to form an approximate Slater function. The basis function $\chi(r)$ for a Slater-type function contracted from N Gaussian functions can be written as:

$$\chi(r) = \sum_{N} c_N \, e^{-a_N \boldsymbol{r}^2} \tag{2.44}$$

where c_N and a_N are constants relating to each Gaussian function N. It is possible to display how contracted basis functions resemble Slater orbitals, by comparing a Slater basis function with the single Gaussian (STO-1G) and the contracted three-Gaussian (STO-3G) basis functions for a single Hydrogen atom. The equations of each function are as follows, where Φ denotes an atomic orbital arising from the basis functions.

$$\Phi_{Slater} = \left(\frac{\zeta^3}{\pi}\right)^{\frac{1}{2}} e^{-\zeta r} = 0.779e^{-1.24r} \tag{2.45}$$

$$\Phi_{STO-1G} = \left(\frac{2a_1}{\pi}\right)^{\frac{3}{4}} e^{-a_1 r^2} = 0.370e^{-0.417r^2} \tag{2.46}$$

$$\begin{aligned} \Phi_{STO-3G} = {} & 0.445\left(\frac{2a_1}{\pi}\right)^{\frac{3}{4}} e^{-a_1 r^2} + 0.535\left(\frac{2a_2}{\pi}\right)^{\frac{3}{4}} e^{-a_2 r^2} \\ & + 0.154\left(\frac{2a_3}{\pi}\right)^{\frac{3}{4}} e^{-a_3 r^2} \\ = {} & 0.0835e^{-0.169r^2} + 0.268e^{-0.624r^2} + 0.278e^{-3.425r^2} \end{aligned} \tag{2.47}$$

If the preceding equations are plotted it can be shown that using the linear combination of Gaussian functions (STO-3G) provides a much better approximation to the Slater function when compared with the single Gaussian (STO-1G) function.

Among the most common basis sets used are those known as split-valence basis sets, first developed by John Pople [11]. It is recognised that most chemistry is concerned with valence orbitals and their interactions, and split-valence basis sets attempt to address this by using more basis functions for the valence space. As an example, one

split-valence basis set, 3-21G, uses one basis function consisting of a linear combination of three Gaussian functions for the core orbitals, then splits the valence orbitals into two parts known as the inner and outer shells. The inner shell uses a contraction of two Gaussian functions, while the outer is a single Gaussian function. The outer shell function has a smaller α value compared to the inner shell, resulting in a longer range drop-off of the function, which allows the valence orbitals to be more diffuse and have a longer spatial range. The basis set 3-21G is an example of a *double-zeta* basis set, where the valence shell is split into two sets of functions. Another popular variation is the *triple-zeta* split-valence basis set, which splits the valence shell into three separate parts, in a similar way to a *double-zeta* basis set. One such example of a *triple-zeta* basis set is the 6-311G set.

These split-valence basis sets can be further added to by adding either polarisation or diffuse functions to the valence orbitals. Polarisation functions, denoted by either an asterisk (for example 6-311G*) or by (d) (for example 6-311G(d)), allow the electron distribution of the valence orbitals to become more polarised, by adding functions describing orbitals of higher angular momentum for the valence orbitals of atoms with atomic number 3-10 and above. This means the six spatial d-orbitals are included. Double polarisation is possible and is denoted by 6-311G** or 6-311G(d, p), where the p-shell spatial orbitals are included for the hydrogen and helium atoms. This can be an important addition as hydrogen atoms especially are ubiquitous to many molecules. Diffuse functions can also be applied to a molecule and are denoted by a +, which would be written as 6-311+G** when used in conjunction with a doubly polarised basis set. Diffuse basis sets add basis functions for the valence shell with increased principle quantum number, and like with the polarised basis sets, one + denotes 3s and 3p orbital functions for atoms with atomic numbers 3-10 and above, and two ++ denotes a 2s

function for Hydrogen and Helium. ***Table 2.1.*** deals with a more thorough breakdown of how the above split-valence basis sets described combine Gaussians and what orbitals they represent for the first- and second-row atoms.

Table 2.1. *Comparison of the size of popular triple-zeta basis sets.*

Basis Set	Atoms	Functions	Gaussians	Total Functions	Total Gaussians
6-311G	H-He	1s, 1s′, 1s″	3, 1, 1	3	5
	Li-Ne	1s 2s, $2p_x$, $2p_y$, $2p_z$ 2s′, $2p_x$′, $2p_y$′, $2p_z$′ 2s″, $2p_x$″, $2p_y$″, $2p_z$″	6 3, 3, 3, 3 1, 1, 1, 1 1, 1, 1, 1	13	26
6-311G*	H-He	*Same as 6-311G*	*Same as 6-311G*	3	5
	Li-Ne	1s 2s, $2p_x$, $2p_y$, $2p_z$ 2s′, $2p_x$′, $2p_y$′, $2p_z$′ 2s″, $2p_x$″, $2p_y$″, $2p_z$″ $3d_{xx}$, $3d_{yy}$, $3d_{zz}$, $3d_{xy}$, $3d_{xz}$, $3d_{yz}$	6 3, 3, 3, 3 1, 1, 1, 1 1, 1, 1, 1 1, 1, 1, 1, 1, 1	19	32
6-311G**	H-He	1s, 1s′, 1s″ $2p_x$, $2p_y$, $2p_z$	3, 1, 1 1, 1, 1	6	8
	Li-Ne	*Same as 6-311G**	*Same as 6-311G**	19	32
6-311++G**	H-He	1s, 1s′, 1s″ $2p_x$, $2p_y$, $2p_z$ 2s	3, 1, 1 1, 1, 1 1	7	9
	Li-Ne	*Same as 6-311G** *with addition of:* 3s, $3p_x$, $3p_y$, $3p_z$	19, 1, 1, 1, 1	23	36

2.3.1. Dunning Basis Sets & the Complete-basis Set Limit

One popular collection of basis sets in use today are the so-called correlation consistent Dunning basis sets [12], which contain functions that are optimised using correlated CISD wavefunctions. CISD (configuration interaction singles & doubles) is an accurate wavefunction based method for directly calculating a system's properties. Correlation consistent basis sets follow the nomenclature cc-pVXZ where *cc-pV* denotes *correlation consistent-polarised valence,* meaning the basis set is correlation consistent and contains valence shells (as in split-valence basis sets), *XZ* denotes whether the basis set is double-zeta (DZ), triple zeta (TZ) or higher order (QZ, 5Z, etc.). Due to the large number of integrals evaluated upon using these basis sets, cc-pVDZ and cc-pVTZ are by far the most commonly used correlation consistent basis sets. Functions for a cc-pVXZ basis set are added in shells. The number of orbitals for atoms for some of these basis sets are presented in ***Table 2.2.*** This shows that for carbon, a relatively small yet ubiquitous atom, for the cc-pVTZ basis set there would be 4s orbitals, 3p orbitals, 2d orbitals and 1f orbital that would need to be evaluated. As these basis sets lead to such a large number of integrals to be evaluated., they are often only used for situations where a large degree of accuracy is required.

Table 2.2. *Comparison of the orbitals present for first- and second-row atoms using popular correlation consistent basis sets.*

Atoms	cc-pVDZ	cc-pVTZ	cc-pVQZ
H-He	*2s1p*	*3s2p1d*	*4s3p2d1f*
Li-Ne	*3s2p1d*	*4s3p2d1f*	*5s4p3d2f1g*

These basis sets can be further expanded with diffuse functions, which are known as *augmented* correlation consistent basis sets, and are represented with the prefix "aug" (such as aug-cc-pVTZ). With these augmented basis sets one set of diffuse functions are added for every angular momentum present in the basis set; returning to the example of carbon, for the aug-cc-pVTZ basis set there would be diffuse s, p, d and f functions.

One significant advantage of using these correlation consistent basis sets is that they scale to the complete basis set limit (CBS). This is effectively the energy of the system using an infinite basis set, and can be quantified for HF calculations with the Dunning basis sets as [13]:

$$E_{HF,\infty} = \frac{x^5 E_{HF,x} - y^5 E_{HF,y}}{x^5 - y^5} \tag{2.48}$$

where $E_{HF,\infty}$ is the CBS energy, and x and y are the highest angular momentum of two sequential basis sets (2 for cc-pVDZ, 3 for cc-pVTZ, etc.). This extrapolation is applied in chapter 5, where MP2 calculations are extrapolated to the CBS based upon the aug-cc-pVDZ and aug-cc-pVTZ basis sets.

2.3.2. Basis Set Superposition Error & Counterpoise Correction

Basis set superposition errors (BSSE) can arise for systems of more than one molecule. As two or more separate molecular systems approach one another their basis functions can overlap in the space between molecules. This effectively means the basis set of one molecule 'borrows' the basis set of the other molecule, so the basis set for both molecules is relevant to calculating the energy of each individual molecule. This has implications when constructing a potential energy curve with respect to separation of two atoms or molecules, as is the case in chapter 5 where the excited states of two such pairs are modelled. If, for example, an argon atom and an ethene molecule are considered, then the argon atom would have access to the basis functions of the ethene molecule (and vice versa), and this effect would become more important as the two structures came closer together. When calculating binding energies which would be the total energy of the system less the individual energies for argon and ethene, BSSE can arise if the argon and ethene are modelled individually with only the orbitals of each individual species included for argon or ethene.

One way to compensate for BSSE is to include a very large number of basis functions, where it is assumed for either atom or molecule the orbitals from other components will not affect the energy much, as the basis set size is already sufficient, as the basis set is approaching the asymptotic limit of the energy. Another method to deal with BSSE is known as the counterpoise method [14]. This method involves comparing the energy of a molecule pair AB with the energy of A within the basis set of the whole system AB, and the same for molecule B. This method directly compensates for BSSE as the individual components of a system are explicitly modelled with the orbital space of the other components included. In this work, the counterpoise method is employed to compensate for BSSE where highly accurate potential energy curves for weakly bound

complexes are calculated. One such accurate method is the second-order Møller-Plesset perturbation theory.

2.4. Møller-Plesset Perturbation Theory

As discussed in section **2.2**, HF theory fails to account properly for electron correlation, which results in a HF energy that is higher than the true energy of a system. Many different ways to account for this correlation energy exist, and are known collectively as post-HF methods. The Møller-Plesset (MP) Perturbation Theory [15] is one of the most widely used post-HF methods in use, particularly the second order variant MP2 theory, which adds dynamic electron correlation effects to the HF equations to improve the result, where dynamic correlation energy arises from HF's failure to keep electrons far enough apart in a system.

MP perturbation theory applies a perturbation to the time-independent Schrödinger equation to account for dynamic correlation effect. It is possible to write this for a perturbed state as

$$\left(\hat{H}^{(0)} + \lambda\hat{V}\right)\Psi_n = E_n\Psi_n \tag{2.49}$$

where $\hat{V}$ is the perturbation operator of the unperturbed Hamiltonian $\hat{H}^{(0)}$, λ is a real parameter that defines the strength of the perturbation and n is a whole integer denoting different discrete states of the system being studied. In MP theory $\hat{H}^{(0)}$ is taken to be the standard HF Hamiltonian.

To understand MP2 theory it is first necessary to understand how successive perturbations affect the complexity of the calculations involved. It is possible to have different orders of perturbation. To model successive perturbations it is possible to expand Ψ_n and E_n as a Taylor series in powers of the parameter λ, which leads to the equation in terms of perturbations $i = 0, 1, 2$ ...:

$$\left(\hat{H}^{(0)} + \lambda\hat{V}\right)\left(\sum_{i=0} \lambda^i {\Psi_n}^{(i)}\right) = \left(\sum_{i=0} \lambda^i {E_n}^{(i)}\right)\left(\sum_{i=0} \lambda^i {\Psi_n}^{(i)}\right) \tag{2.50}$$

Writing out this equation only for terms up to and including $i = 2$ and eliminating terms with powers of λ above λ^2 gives all the terms necessary to understand MP2 perturbation.

$$\begin{aligned} \hat{H}^{(0)}{\Psi_n}^{(0)} + \lambda\left(\hat{H}^{(0)}{\Psi_n}^{(1)} + \hat{V}{\psi_n}^{(0)}\right) + \lambda^2\left(\hat{H}^{(0)}{\Psi_n}^{(2)} + \hat{V}{\Psi_n}^{(1)}\right) \\ = {E_n}^{(0)}{\Psi_n}^{(0)} + \lambda\left({E_n}^{(0)}{\Psi_n}^{(1)} + {E_n}^{(1)}{\Psi_n}^{(0)}\right) \\ + \lambda^2\left({E_n}^{(0)}{\Psi_n}^{(2)} + {E_n}^{(1)}{\Psi_n}^{(1)} + {E_n}^{(2)}{\Psi_n}^{(0)}\right) \end{aligned} \tag{2.51}$$

From this one can derive the zeroth-, first- and second-order perturbations as the terms that depend on λ^0, λ^1, and λ^2 respectively. For a zeroth-order system the result is simply the Schrödinger equation for an unperturbed system.

$$\hat{H}^{(0)}{\Psi_n}^{(0)} = {E_n}^{(0)}{\Psi_n}^{(0)} \tag{2.52}$$

For a first-order perturbation the terms are those from Eq. (2.51) which are multiplied by the perturbation parameter λ:

$$\hat{H}^{(0)}{\Psi_n}^{(1)} + \hat{V}{\Psi_n}^{(0)} = {E_n}^{(0)}{\Psi_n}^{(1)} + {E_n}^{(1)}{\Psi_n}^{(0)} \tag{2.53}$$

Finally, for a second-order perturbation the terms are those from Eq. (2.51) which are multiplied by the perturbation parameter squared λ^2:

$$\hat{H}^{(0)}{\Psi_n}^{(2)} + \hat{V}{\Psi_n}^{(1)} = {E_n}^{(0)}{\Psi_n}^{(2)} + {E_n}^{(1)}{\Psi_n}^{(1)} + {E_n}^{(2)}{\Psi_n}^{(0)} \tag{2.54}$$

To obtain the expectation values of these expressions they can be multiplied through by the complex conjugate of the zero-order wavefunction ${\Psi_n}^{(0)*}$ and then integrated throughout, yielding the following expressions for the first three energy terms.

$${E_n}^{(0)} = \left\langle {\Psi_n}^{(0)} \middle| \hat{H} \middle| {\Psi_n}^{(0)} \right\rangle \tag{2.55}$$

$$E_n{}^{(1)} = \langle \Psi_n{}^{(0)} | \hat{V} | \Psi_n{}^{(0)} \rangle \tag{2.56}$$

$$E_n{}^{(2)} = \langle \Psi_n{}^{(0)} | \hat{V} | \Psi_n{}^{(1)} \rangle \tag{2.57}$$

MP0, the zeroth-order perturbation, only describes $E_n{}^{(0)}$, the sum of the HF one-electron energies. This ignores interelectronic repulsion apart from following the Pauli exclusion principle. MP1 includes the $E_n{}^{(1)}$ term, which includes the two-electron Coulomb and exchange integrals. MP1 theory is therefore equal to the standard HF energy, so MP2 is the first perturbation to improve upon HF theory. The MP2 method adds dynamic electron correlation effects and is added to the HF energy as shown in Eq. (2.59).

$$E_{MP1} = E_n{}^{(0)} + E_n{}^{(1)} = \langle \Psi_n{}^{(0)} | \hat{H}^{(0)} + \hat{V} | \Psi_n{}^{(0)} \rangle = E_{HF}^{total} \tag{2.58}$$

$$E_{MP2} = E_{HF}^{total} + E_n{}^{(2)} \tag{2.59}$$

The HF energy already includes all internuclear repulsion terms, which leads to $E_n{}^{(2)}$ being a purely electronic term, which takes the form of the sum of pairs of electrons excited from occupied to unoccupied (virtual) orbitals. This technique is known as double excitation and is commonly seen throughout other post-HF methods. The MP2 energy term $E_n{}^{(2)}$ can be shown to be for the lowest quantum state $(n = 0)$:

$$E_0{}^{(2)} = \frac{1}{4} \sum_{ab}^{virt} \sum_{ij}^{occ} \frac{|\langle ab \| rs \rangle|^2}{\varepsilon_a + \varepsilon_b - \varepsilon_r - \varepsilon_s} \tag{2.60}$$

In Eq. (2.60) a and b denote virtual spin orbitals, r and s are occupied spin orbitals, and ε_a, ε_b, ε_r, and ε_s are the respective orbital energies. The numerator of this equation is an integral defined by the term in Eq. (2.61) where the two electron integral of the form $\langle ij \| kl \rangle$ is defined as follows in Eqs. (2.62) and (2.63)

$$\langle ab||rs\rangle = \langle\psi_0|\sum_{i<j} r_{ij}^{-1}\,|\psi_{ab}^{rs}\rangle \tag{2.61}$$

$$\langle ab||rs\rangle = \langle ij|kl\rangle - \langle ij|lk\rangle \tag{2.62}$$

$$\langle ij|kl\rangle = \int\int \frac{\psi_i^*(\boldsymbol{r}_1)\psi_j(\boldsymbol{r}_1)\psi_k^*(\boldsymbol{r}_2)\psi_l(\boldsymbol{r}_2)}{r_{12}}\,d\boldsymbol{r}_1 d\boldsymbol{r}_2 \tag{2.63}$$

MP2 evaluates this energy correction and accounts for electron correlation by exciting electrons from occupied to unoccupied orbitals. The advantage of using virtual orbitals is that they allow electrons more room within the molecule, which reduces the chance of electrons being calculated in close proximity to one another, thus lowering the problems of electron correlation. Looking at the term in Eq. (2.60) describing the energy gap between occupied and unoccupied orbitals, $(\varepsilon_a + \varepsilon_b - \varepsilon_r - \varepsilon_s)$ it is apparent that as it increases, the orbital interaction decreases, along with the MP2 contribution ${E_0}^{(2)}$. This means that as the energy gap between occupied and unoccupied orbitals increase, promotion of electrons to these orbitals becomes more difficult, and the MP2 energy does not stabilise the energy with respect to HF as much as a system with lower lying excited states.

Although MP2 leads to more accurate results than standard HF, there are more complex and computationally expensive wavefunction based methods that can also be applied, such as coupled-cluster theory and configuration interaction. For many calculations, however, MP2 theory is classed as an 'accurate' method, although higher order MP3, MP4 etc. is possible, these are rarely used due to their large computational cost.

2.5. Coupled-Cluster Theory

Coupled-cluster (CC) methods, like MP2 theory, attempts to correct the HF energy by accurately calculating a correction to the dynamic electron correlation energy [16]. There are many varieties of CC methods, involving different orders of excitations, as well as perturbative excitations. The specific method known as coupled-cluster singles and doubles, with perturbative triples CCSD(T) [17] is referred to as the 'gold standard' of computational chemistry, due to its high accuracy for a wide variety of systems.

The essential idea underpinning CC theory is that the ground state wavefunction of a molecular system $|\psi_0\rangle$, can be described by the exponential ansatz

$$|\psi_{CC}\rangle = e^{\hat{T}}|\Phi_0\rangle \tag{2.64}$$

where ψ_{CC} is the coupled-cluster wavefunction, $e^{\hat{T}}$ is the exponential of an operator $\hat{T}$ and Φ_0 is the Slater determinant of the system. As $e^{\hat{T}}$ is an exponential function it can be expanded into the sequence

$$e^{\hat{T}} = 1 + \hat{T} + \frac{\hat{T}^2}{2!} + \frac{\hat{T}^3}{3!} + \cdots \tag{2.65}$$

The operator $\hat{T}$ can be further split into a sequence of operators

$$\hat{T} = \hat{T}_1 + \hat{T}_2 + \hat{T}_3 + \cdots \tag{2.66}$$

where $\hat{T}_1$, $\hat{T}_2$ etc. are excitation operators and describe the promotion of electrons from occupied orbitals to virtual (unoccupied) orbitals as described in Eqs. (2.62) and (2.63), where $\hat{T}_1$ describes single excitations and $\hat{T}_2$ describes double excitations. The excitation operators for higher orders would follow a similar pattern for higher level excitations.

$$\hat{T}_1|\Phi_0\rangle = \sum_{i}^{occ.}\sum_{a}^{virt.} t_i^a \, \Phi_i^a \tag{2.67}$$

$$\hat{T}_2|\Phi_0\rangle = \sum_{ij}^{occ.}\sum_{ab}^{virt.} t_{ij}^{ab} \, \Phi_{ij}^{ab} \tag{2.68}$$

In the above equations, t refers to the one electron coupled-cluster amplitude, where i or ij denotes the occupied electrons and a or ab the unoccupied electrons, and Φ refer to the CC molecular orbitals. The most common CC method encountered involves only the first two expansions to $\hat{T}$ and involves singles and doubles (CCSD) [18] although higher order calculations involving triple excitations (CCSDT) and quadruples (CCSDTQ) can be used, at a significantly higher computational cost. These higher-order calculations are often prohibitively expensive for calculations on systems involving more than a few electrons. CC theory can be combined with perturbative excitations, such as CCSD with perturbative triples, known as CCSD(T). It is this method that is applied in chapter 5 to obtain 'accurate' potential energy curves.

The energy of a system using CCSD involves expansions of $\hat{T}$ up to and including $\hat{T}_2$ and can be explained in the following set of equations. The coupled-cluster exponential operator involves terms $\hat{T}_1$ and $\hat{T}_2$ which can be expanded as shown in Eq. (2.70). This has only been expanded to $\hat{T}^2$ but can be further expanded to give more terms.

$$|\psi_{CCSD}\rangle = e^{\hat{T}_1+\hat{T}_2}|\Phi_0\rangle \tag{2.69}$$

$$e^{\hat{T}_1+\hat{T}_2} = 1 + \hat{T}_1 + \hat{T}_2 + \frac{\hat{T}_1^{\,2}}{2} + \frac{\hat{T}_2^{\,2}}{2} + \hat{T}_1\hat{T}_2 \ldots \tag{2.70}$$

The coupled-cluster energy can be expressed by the forms seen in the following equations, which can be rearranged to give an expression equal to zero.

$$E_{CCSD} = \langle \Phi_0 | \hat{H} | \psi_{CCSD} \rangle \tag{2.71}$$

$$E_{CCSD} = \langle \Phi_0 | \hat{H} | e^{\hat{T}_1 + \hat{T}_2} \Phi_0 \rangle \tag{2.72}$$

$$\langle \Phi_0 | \hat{H} - E_{CCSD} | e^{\hat{T}_1 + \hat{T}_2} \Phi_0 \rangle = 0 \tag{2.73}$$

The exponential operator can be expanded in Eq. (2.73) to give

$$\left\langle \Phi_0 \middle| \hat{H} - E_{CCSD} \middle| \left(1 + \hat{T}_1 + \hat{T}_2 + \frac{\hat{T}_1^{\,2}}{2} + \frac{\hat{T}_2^{\,2}}{2} + \hat{T}_1 \hat{T}_2 \ldots \right) \Phi_0 \right\rangle = 0 \tag{2.74}$$

For many systems, double excitation do not appropriately account for all electron correlation effects, therefore triples excitations must be considered. As explicit triple excitation using coupled-cluster methods (CCSDT) are often prohibitively expensive to calculate, perturbative triples can be introduced. These triple excitations are found from the single determinant reference which arises is higher order MP perturbations. Although CC methods are size consistent, they are not variational by default, although variational CC methods have been introduced, they are computationally very expensive [19]. This means using non-variational CC theory it can be difficult to assess the accuracy of a method compared to other variational methods.

2.6. Density Functional Theory

Density functional theory (DFT) is currently the most popular method of quantum chemical calculation. Many post-HF methods, although accurate for a variety of systems, are prohibitively expensive for many calculations. DFT provides a significant improvement on the accuracy of HF calculations with a relatively low computational cost. It is worth noting DFT is not a wavefunction-based method like HF theory and related methods. The electron density of an N-electron system is given by the following equation, where $\psi_i(\boldsymbol{r})$ describes a set of molecular orbitals and $\rho(\boldsymbol{r})$ is the electron density (probability of finding an electron within the volume $d\boldsymbol{r}$).

$$\rho(\boldsymbol{r}) = \sum_{i}^{N} |\psi_i(\boldsymbol{r})|^2 \tag{2.75}$$

The integral of the electron density gives the number of electrons in the system N:

$$\int \rho(\boldsymbol{r})\, d\boldsymbol{r} = N \tag{2.76}$$

One advantage of electron density over wavefunction methods is that electron density is an observable property, and can be measured practically by methods such as X-ray diffraction. Another important aspect of the electron density is that at any position of an atom, the electron density $\rho(\boldsymbol{r})$ has a maximum with a finite value. The gradient of electron density around an atom is related to nuclear charge on the atom. One other property of electron density is that it is a function of position in three-dimensional space, giving it only three variables. This differs from wavefunction based methods which rely on three spatial coordinates and one spin coordinate per electron, giving $4N$ variables in an N electron system. This means the amount of variables on a density based system does not change with the size of the system, in contrast to wavefunction methods.

Hohenberg and Kohn in 1964 [20], proved that for molecules with a nondegenerate ground state, molecular energy, wavefunctions and all other properties can be determined by the ground state electron probability density, ρ_0,

$$\rho_0(\boldsymbol{r}) \rightarrow E_0 \tag{2.77}$$

This means E_0 is a functional of $\rho_0(\boldsymbol{r})$, which acts on the density (a function) to give a number (the energy of a system). The first Hohenberg-Kohn theorem states that any ground state property is a functional of the ground state density functional. This is shown below for energy, where square brackets denote a functional.

$$E[\rho_0] = E_0 \tag{2.78}$$

The second Hohenberg-Kohn theorem states that the energy is variational, which means any trial electron density functional $E_v[\rho_t]$ will give an energy greater than or equal to the true energy $E_0[\rho_0]$.

$$E_v[\rho_t] \geq E_0[\rho_0] \tag{2.79}$$

This was proved by first looking at the ground state electronic wavefunction for an N-electron molecule, which is an eigenfunction of the electronic Hamiltonian, $\hat{H}_e$ Eq. (2.25), which consists of a kinetic energy function, $\hat{T}$, an electron-nuclei attraction term, $\hat{V}_{ne}$, and an electron-electron repulsion term,$\hat{V}_{ee}$.

$$\hat{H}_e = \hat{T} + \hat{V}_{ne} + \hat{V}_{ee} \tag{2.80}$$

$$\hat{V}_{ne} = \sum_{i=1}^{n} \mathrm{v}(\boldsymbol{r}) \tag{2.81}$$

$$\mathrm{v}(\boldsymbol{r}) = -\sum_{\alpha} \frac{Z_\alpha}{r_{i\alpha}} \tag{2.82}$$

The potential energy of interaction between an electron and the nuclei (2.81) depends on electronic and nuclear coordinates, and due to the Born-Oppenheimer

approximation, nuclei positions are fixed, so are constant. Therefore $\mathrm{v}(\boldsymbol{r})$ becomes a function of only the positions of the electrons, which is known as the external potential.

Hohenberg and Kohn proved that the external potential and number of electrons in a system can be determined by knowing ρ_0, by imagining two different external positions which give rise to the same electron density. This assumption was known to be false, which means every electron density is unique, with its own unique external potential. Hence the ground state electron density can uniquely determine the electronic Hamiltonian, and therefore also the ground state wavefunction, energy, and other molecular properties.

As it has been shown energy can be written as a functional of the electron density, it then follows that components of the energy can also be described as functionals of ρ_0.

$$E_0 = E[\rho_0] = \bar{T}[\rho_0] + \bar{V}_{ne}[\rho_0] + \bar{V}_{ee}[\rho_0] \tag{2.83}$$

Although $\bar{V}_{ne}[\rho_0]$ can be exactly calculated, due to it relying on the external potential (2.81), it was found $\bar{T}[\rho_0]$ and $\bar{V}_{ee}[\rho_0]$ could not be calculated exactly, and can be grouped into an unknown functional, $\bar{F}[\rho_0]$, as shown in Eq. (2.85), which is independent of the external potential and needs some practical method to calculate it.

$$\bar{V}_{ne} = \int \rho_0(\boldsymbol{r})\mathrm{v}(\boldsymbol{r})d\boldsymbol{r} \tag{2.84}$$

$$\bar{T}[\rho_0] + \bar{V}_{ee}[\rho_0] = \bar{F}[\rho_0] \tag{2.85}$$

The expression for the energy Eq. (2.83) can be rewritten as

$$E_0 = \int \rho_0(\boldsymbol{r})\mathrm{v}(\boldsymbol{r})d\boldsymbol{r} + \bar{F}[\rho_0] \tag{2.86}$$

A way of calculating the unkown term $\bar{F}[\rho_0]$ was formalised in 1965 by Kohn and Sham [21], and is the method most DFT calculations, including those in this thesis, are solved by to this day.

Kohn-Sham (KS) DFT involves using a fictitious reference system of N-electrons, denoted with an s, which is analogous to the system which is being studied except with non-interacting electrons, with each electron experiencing the same external potential $\mathrm{v}_s(\boldsymbol{r})$. The aim of KS-DFT is to find an external potential such that the electron density of the reference system, ρ_s, is equivalent to the electron density of the real system, ρ_0. The Hamiltonian of this reference system eliminates electron-electron repulsion terms, as there is no electron interaction, so one can simplify Eq. (2.25) to the expression shown in Eq. (2.87), where $\hat{h}_i^{KS}$ is the one-electron KS Hamiltonian.

$$\hat{H}_s = -\frac{1}{2}\sum_i^N \nabla_i^2 + \sum_i^N \mathrm{v}_s(\mathbf{r}) = \sum_i^N \hat{h}_i^{KS} \tag{2.87}$$

The reference system can then be related to the real system by rewriting the electronic Hamiltonian as is seen in Eq. (2.88). In this form, λ is a parameter ranging between 0 and 1 which at 0 completely describes the reference system, and at 1 describes the true system. $\mathrm{v}_\lambda(\boldsymbol{r})$ is the external potential needed to make the ground state electron density of the reference system to that of the true molecular ground state.

$$\hat{H}_\lambda = \hat{T} + \sum_i^N \mathrm{v}_\lambda(\boldsymbol{r}) + \lambda\hat{V}_{ee} \tag{2.88}$$

As this ground state electronic wavefunction of the reference system contains only non-interacting particles, it is the antisymmetrised product of the lowest energy KS spin-orbitals of the reference system. Finding these orbitals will in turn find the electron density of the true system. The unknown part of the energy functional, $\bar{F}[\rho_0]$ from Eq. (2.85) can have its components written in terms of the difference between the reference system and real system, where subscript s denotes a reference term.

$$\Delta\bar{T}[\rho_0] \equiv \bar{T}[\rho_0] - \bar{T}_s[\rho_0] \tag{2.89}$$

$$\Delta\bar{V}_{ee}[\rho_0] \equiv \bar{V}_{ee}[\rho_0] - \bar{V}_{ee(s)}[\rho_0] \tag{2.90}$$

The difference in electron-electron repulsion $\Delta\bar{V}_{ee}[\rho_0]$ can also be defined as the deviation of the true energy from the Coulomb repulsion $\bar{J}[\rho_0]$

$$\Delta\bar{V}_{ee}[\rho_0] \equiv \bar{V}_{ee}[\rho_0] - \bar{J}[\rho_0] \tag{2.91}$$

where

$$\bar{J}[\rho_0] = \frac{1}{2}\int\int \frac{\rho_0(\boldsymbol{r}_1)\rho_0(\boldsymbol{r}_2)}{r_{12}} d\boldsymbol{r}_1 d\boldsymbol{r}_2 \tag{2.92}$$

All the reference and Coulomb terms in the above equations can be solved exactly. On rewriting equations (2.89) and (2.91) in terms of the real energy functions,

$$\bar{T}[\rho_0] \equiv \Delta\bar{T}[\rho_0] + \bar{T}_s[\rho_0] \tag{2.93}$$

$$\bar{V}_{ee}[\rho_0] \equiv \Delta\bar{V}_{ee}[\rho_0] + \bar{J}[\rho_0] \tag{2.94}$$

then substituting these expressions for the kinetic energy and electron-electron repulsion functionals into the equations for the overall energy Eq. (2.83) and Eq. (2.86), it is possible to construct an equation for the ground state energy of a molecule as a functional of the electron density of that system.

$$E_0 = E[\rho_0] = \bar{T}_s[\rho_0] + \bar{V}_{ne}[\rho_0] + \bar{J}[\rho_0] + \Delta\bar{T}[\rho_0] + \Delta\bar{V}_{ee}[\rho_0] \tag{2.95}$$

The above expression now leaves the terms $\Delta\bar{T}[\rho_0]$ and $\Delta\bar{V}_{ee}[\rho_0]$ which are unknown terms. These are grouped together into what is known as the exchange-correlation functional E_{xc}, which gathers together all unknown terms in the energy expression.

$$E_{xc}[\rho_0] = \Delta\bar{T}[\rho_0] + \Delta\bar{V}_{ee}[\rho_0] \tag{2.96}$$

This allows one to rewrite Eq. (2.95) to give a full expression for the energy of a system.

$$E_0 = \int \rho_0(\boldsymbol{r})\mathrm{v}(\boldsymbol{r})d\boldsymbol{r} + \bar{T}_s[\rho_0] + \frac{1}{2}\int\int \frac{\rho_0(\boldsymbol{r}_1)\rho_0(\boldsymbol{r}_2)}{r_{12}} d\boldsymbol{r}_1 d\boldsymbol{r}_2 + E_{xc}[\rho_0] \tag{2.97}$$

The KS equations are used to find the energy of the system, and are derived from the second Hohenberg-Kohn theorem, that states DFT is variational. It is shown that the electron density of the reference system ρ_s is equal to that of the real system ρ_0, and that electron density can be expressed in terms of KS orbitals

$$\rho_0 = \rho_s = \sum_i^{2n} \left|\psi_i^{KS}(1)\right|^2 \tag{2.98}$$

where ψ_i^{KS} are the KS spatial orbitals and n is the number of occupied KS orbitals. As the orbitals can be doubly occupied with different spin electrons, $2n$ is the number of electrons in the system for closed-shell systems. KS-DFT works by attempting to minimise the energy of the individual Kohn-Sham orbitals using a one electron Schrödinger-like equation to work out the energy

$$\hat{h}_i^{KS}(1)\psi_i^{KS}(1) = \varepsilon_i^{KS}(1)\psi_i^{KS}(1) \tag{2.99}$$

where $\hat{h}_i^{KS}$ is the one-electron hamiltonian, ψ_i^{KS} are the KS orbitals and ε_i^{KS} is the energy level of the electron using KS-DFT. The one-electron Hamiltonian is given by substituting the density expression Eq. (2.98) into Eq. (2.97), then varying E_0 with respect to the KS spatial orbitals:

$$\hat{h}_i^{KS} = -\frac{1}{2}\sum_i^N \nabla_i^2 - \sum_A \frac{Z_A}{r_{iA}} + \int \frac{\rho_0(\boldsymbol{r}_2)}{r_{12}} d\boldsymbol{r}_2 + v_{xc}(1) \tag{2.100}$$

The term $v_{xc}(N)$ is the exchange correlation potential (for an electron number N), which is which is evaluated from a derivative of the unknown exchange correlation functional $E_{xc}[\rho]$, and is defined as

$$v_{xc}(\boldsymbol{r}) = \frac{\delta E_{xc}[\rho(\boldsymbol{r})]}{\delta\rho(\boldsymbol{r})} \tag{2.101}$$

When comparing with HF theory, which is an approximation of the Schrödinger equation, the KS energy in Eq. (2.97) is exact as long as the exchange correlation functional $E_{xc}[\rho]$ is also exact. Unfortuately as the exchange correlation functional is a collection of the unknown terms it cannot be calculated exactly, so the DFT energy will always be slightly different to the true energy of a system. How much that energy deviates depends on both the size of the basis set and the choice of the exchange correlation functional, of which there are many different types and forms.

2.6.1. Exchange-correlation Functionals

There are several different approaches to calculating the exchange correlation functional. The simplest model, known as the local density approximation (LDA) was originally suggested by Kohn and Sham [21]. LDA functionals assume that if electron density ρ varies very slowly with position, then $E_{xc}[\rho]$ relates to an integral of electron density and exchange-correlation energy per electron e_{XC}^{UEG}, at a uniform density ρ.

$$E_{XC}^{LDA} = \int e_{XC}^{UEG}(\rho)\, d\boldsymbol{r} \tag{2.102}$$

This is based on the uniform electron gas model and is quite a simplistic view of electron behaviour, as it assumes that the electron density has zero gradient around a point. One variety of LDA applies different spatial orbitals ψ_{α}^{KS} and ψ_{β}^{KS} to electrons with different spins α and β within the uniform gas model. This method, known as the local density spin approximation (LSDA) is analogous to using unrestricted HF theory as opposed to spin restricted HF, and can be applied to systems with unpaired electrons.

As a real molecular system does not have a uniform electron distribution, LDA and LSDA functionals offer poor approximations for the exchange correlation functional. A way to improve the model is to use a generalised-gradient approximation (GGA) functional, where both electron density at a point $\boldsymbol{r}$ as well as the gradient of the electron density at $\boldsymbol{r}$ are used to form the exchange correlation functional. One example of a GGA functional is the Perdew–Burke–Ernzerhof (PBE) functional [22]. One other popular GGA functional is the BLYP (Becke-Lee-Yang-Parr). This functional involves the separating of the exchange and correlation parts of E_{xc},

$$E_{XC} = E_X + E_C \tag{2.103}$$

where in the context of the BLYP functional, the exchange functional is Becke's exchange functional [23], and the correlation functional is the Lee-Yang-Parr correlation functional [24].

One other type of exchange correlation functional with wide use in DFT calculations are hybrid functionals. These functionals include a degree of exact HF exchange energy, which can be taken from the equation for total HF energy Eq. (2.32) and expressed as a sum of the exchange integrals from Eq. (2.28)

$$E_X = -\frac{1}{2}\sum_{i=1}^{n}\sum_{j=1}^{n} K_{ij} \tag{2.104}$$

Substituting the HF orbitals in Eq. (2.28) for KS orbitals gives the exact HF exchange energy for a system of non-interacting electrons:

$$E_X^{HF} = -\sum_{i=1}^{n}\sum_{j=1}^{n}\left\langle \psi_i^{KS}(1)\psi_j^{KS}(2)\left|\frac{1}{r_{12}}\right|\psi_i^{KS}(2)\psi_j^{KS}(1)\right\rangle \tag{2.105}$$

The most popular hybrid exchange-correlation functional in use at the moment is the B3LYP functional [25, 26]. This functional has found a wide variety of applications in many fields and has proved to give good results for many systems with a relatively small computational cost. B3LYP includes a component of exact HF exchange, LDA exchange and GGA exchange along with correlation terms. All these terms have been fitted according to empirical parameters as follows:

$$E_{XC}^{B3LYP} = a_0 E_X^{HF} + (1 - a_0 - a_x)E_X^{LDA} + a_x E_X^{B88} + (1 - a_c)E_C^{VWN} + a_c E_C^{LYP} \tag{2.106}$$

where the parameters a_0=0.2, a_x=0.72, and a_c=0.81, leading to the expression

$$E_{XC}^{B3LYP} = 0.2E_X^{HF} + 0.08E_X^{LDA} + 0.72E_X^{B88} + 0.19E_C^{VWN} + 0.81E_C^{LYP} \tag{2.107}$$

Within Eq. (2.107), E_X^{HF} is the term for the HF exact exchange, E_X^{LDA} describes the LDA contribution to the exchange functional and E_X^{B88} is the Becke component of exchange. For the correlation terms, E_C^{VWN} is the correlation functional according to Vosko, Wilk and Nusair [27] and E_C^{LYP} is the Lee-Yang-Parr correlation functional as seen earlier for the BLYP exchange correlation functional.

Another hybrid functional used in this thesis is the B97-1 functional, which is an improvement on the B97 functional introduced by Becke in 1997 [28]. B97 takes the form seen in Eq. (2.108), where the term c_x has been reparameterised as 0.21 for B97-1, and has been shown to produce good results with respect to experimental values [29].

$$E_{XC}^{B97-1} = c_x E_X^{HF} + (1 - c_x) E_X^{GGA} + E_C^{GGA} \tag{2.108}$$

2.6.2. Long-range-corrected Functionals

Although B3LYP and B97-1 have been shown to be versatile functionals with a wide range of potential applications, they fail in three key areas:

1. Accurately calculate the polarisability of long chain molecules.
2. Electronic excitations using time-dependent DFT (TDDFT) to high energy Rydberg states.
3. Charge-transfer (CT) excitations, where transfer of electrons occurs in a system where the orbitals involved in transition are separated by a significant distance (several Å or more).

The third area is of particular importance to this work, as CT excitations are important to the fluorescent activity of the potassium cation sensor studied in chapter 4, so accurately calculating the energies of these states is essential. The failure of standard hybrid functionals to calculate these energies accurately is due to CT states requiring full (100%) HF exchange, whereas standard B3LYP and B97-1 only contain around 20% HF exchange. In TDDFT the excitation energy for a CT transition is essentially the energy difference between the orbital energies. Due to the approximate exchange in the functional this separation is often underestimated. These errors in calculations have been shown to appear significantly from separations in the CT transitions as low as 2 Å [30].

There are two ways to model this long-range HF exchange within an exchange correlation functional. The first method involves preserving the chosen functional at a short-range, while incorporating 100% HF exchange at long-range, with a mixture at a medium-range. Such functionals are known as ‘Coulomb-attenuated’ or ‘long-range-corrected’ functionals, two examples of such functionals which are used in this work

include the Coulomb-attenuated method B3LYP (CAM-B3LYP) functional, as well as the ω-B97 functional [31, 32]. These functionals involve a partitioning of the electron-electron Coulomb potential into short- and long-range terms:

$$\frac{1}{r_{12}} = \frac{1 - \mathrm{erf}(\omega r_{12})}{r_{12}} + \frac{\mathrm{erf}(\omega r_{12})}{r_{12}} \tag{2.109}$$

where erf is the error function, the right-hand term is a short-range term that decays to zero with increasing interelectronic radius r_{12}. The first term deals with long-range interaction and stays relatively constant beyond a point. ω is a parameter that controls the extent of the two terms at a particular separation. For CAM-B3LYP, the above term is expanded to include further parameters α and β:

$$\frac{1}{r_{12}} = \frac{1 - [(\alpha + \beta)\mathrm{erf}(\omega r_{12})]}{r_{12}} + \frac{(\alpha + \beta)\mathrm{erf}(\omega r_{12})}{r_{12}} \tag{2.110}$$

where $\alpha = 0.2$, $\beta = 1.0$ and $\omega = 0.33/r_{Bohr}$ for the CAM-B3LYP functional. This is shown to give good improvements for energies of Rydberg and CT states over standard B3LYP using TDDFT.

The second method for calculating long-range exchange accurately is by parameterising new functionals which directly deal with exact HF exchange at long-range. One such functional is the M06-HF functional [33], which contains a large number of adjustable parameters. These types of functional are not used in this work.

As well as failing to accurately model CT and Rydberg states accurately, regular DFT also fails to accurately model dispersion forces in systems. There are several approaches to incorporating dispersion into DFT, which will be summarised in the following section.

2.6.3. Dispersion Corrections to DFT

As previously mentioned, standard exchange-correlation functionals fail to accurately model dispersion forces in a molecular system. This is due to the fact that many exchange–correlation functionals are functionals of the local electron density or the gradient of the local electron density in LDA and GGA-type functionals respectively. This means only local effects influence the behaviour of the electrons in a system. Dispersion forces arise when an instantaneous dipole on one molecule or atom induces a dipole on another molecule in the system. This creates instantaneous dipoles between the two species, which results in a weak attraction force. This is an inherently non-local effect. As the interactions in standard DFT use local electron interaction these dipoles do not form and therefore dispersion forces do not occur. There are several different approaches to overcoming this problem within DFT. One way is to model dispersion explicitly with parameterised functionals that do not contain an explicit dispersion term using systems where dispersion interactions are prominent. Examples of this approach are the M05 [34] and M06 [35] functionals, which have proven successful for modelling some dispersion bound complexes. This thesis concentrates on the more common methods of correcting for dispersion, which involve an add-on term to the standard DFT energy

$$E_{DFT-D} = E_{KS-DFT} + E_{disp} \tag{2.111}$$

where E_{DFT-D} is the dispersion-corrected energy, E_{KS-DFT} is the standard Kohn-Sham DFT energy and E_{disp} is the dispersion correction. Among the most popular dispersion corrections to DFT (DFT-D methods) is Grimme's D2 and D3 empirical corrections [3, 4, 36]. These methods are both similar and include E_{disp} as a sum of pairwise interactions of atoms in a system. For the D2 correction (DFT-D2) E_{disp} takes the form

$$E_{disp}^{D2} = -s_6 \sum_{A}^{N} \sum_{B<A}^{N} \frac{C_6^{AB}}{R_{AB}^6} f_{dmp}(R_{AB}) \tag{2.112}$$

where A and B are atoms in an N-atom system, R_{AB} is the distance between atoms A and B, s_6 is a global scaling parameter, $f_{dmp}(R_{AB})$ is the damping function which prevents the dispersion energy becoming infinitely high at small R_{AB} separations. C_6^{AB} is a term which combines atomic parameters C_6^A and C_6^A and takes the form:

$$C_6^{AB} = \sqrt{C_6^A C_6^B} \tag{2.113}$$

The damping function is of the form

$$f_{dmp}(R_{AB}) = \frac{1}{1 + exp\left[-d\left(\frac{R_{AB}}{R_{AB}^0} - 1\right)\right]} \tag{2.114}$$

and includes two further parameters, d is the global scaling parameter for the damping function and R_{AB}^0 is the sum of the van der Waals radii of atoms A and B. The values for R_{AB}^0 and C_6^A have been determined by Grimme from experimental observations, and the global scaling parameters assessed for a range of functionals to empirically determine optimum results using those functionals. For PBE, s_6 is 0.75, whereas for B3LYP s_6 is 1.05. These two functionals are used in chapter 5 in conjunction with DFT-D2.

Grimme also parameterised the slightly improved DFT-D3 method, where higher orders of C^{AB} can be applied to the system as well as a term evaluating three-body interactions. For this study, three-body interactions were not considered. The expression for the dispersion interactions of two-body terms is

$$E_{disp}^{D3} = -\sum_{A}^{N} \sum_{B<A}^{N} \sum_{n=6,8,10\ldots} s_n \frac{C_6^{AB}}{R_{AB}^6} f_{dmp}(R_{AB}) \tag{2.115}$$

which follows a similar format and parameters to the DFT-D2 method.

As well as the empirical D2 and D3 methods, it is possible to introduce an add-on term to DFT which is calculated directly as opposed to relying on empirical terms. One such method is the exchange-dipole model (XDM) [37, 38]. This model calculates dispersion directly from the interaction between the instant dipole moment of the exchange hole in one atom or molecule in system, and the induced dipole moment in the other atom or molecule. The exchange hole refers to the space around an electron where there is almost zero probability of finding another electron. The XDM add-on term takes the form

$$E_{disp}^{XDM} = -\sum_{A>B} \frac{C_6^{AB}}{R_{AB}^6 + kC_6^{AB}/(E_A^C + E_B^C)} \tag{2.116}$$

where k is a universal scaling parameter, E_A^C and E_B^C are the absolute values of correlation energies of atoms A and B, and C_6^{AB} takes the form

$$C_6^{AB} = \frac{\langle d_X^2\rangle_A \langle d_X^2\rangle_B \alpha_A \alpha_B}{\langle d_X^2\rangle_A \alpha_B + \langle d_X^2\rangle_B \alpha_A} \tag{2.117}$$

where $\langle d_X^2\rangle_A$ is the exchange hole dipole moment of atom A, and α_A is the effective polarisability of atom A.

2.7. Excited State Methods

The methods described so far are appropriate for the electronic ground state, i.e. the electrons in a molecular system are in their lowest energy configuration. In many cases, however, it is necessary to model an electronically excited state of a system, for example when studying absorption and emission spectra of a molecule, where a molecule gains or loses a photon to change its electronic state. These processes are the main focus of chapters 3 and 4 of this work, where the fluorescence activity of fluorescent sensors are studied. It may also be of interest to perform calculations on a molecule in an excited state to investigate its behaviour and interactions with other molecules, and how that compares to the ground state; this is the focus of chapter 5. Other situations where electronically excited states are modelled include the calculating of X-ray spectra of molecules. The ability to accurately model excited state systems is essential to many areas of computational chemistry. Two DFT-based methods are discussed in this section: the time-dependent density functional theory approach and the maximum overlap method. Also discussed is the excited state coupled-cluster method using equations of motion.

2.7.1. Time-Dependent Density Functional Theory

Time-dependent DFT (TDDFT) is a variant of ground-state DFT that calculates electronic excitations and other time-dependent effects [39]. TDDFT, like ground-state DFT, only relies on the electron density dependent on three spatial variables, making it computationally more simple than wavefunction methods which rely on $4N$-variables in an N-electron system. The ground-state Hohenberg-Kohn theorems state that all ground-state properties of a molecule can be determined by the ground-state electron density, with a ground-state property being a functional of the electron density functional, and that the energy is variational.

Extending the Hohenberg-Kohn theorem to a time-dependent framework is described by the Runge-Gross theorem [40], which states that for a many-body time-dependent system evolving from an initial wavefunction, all properties can be calculated with the knowledge of the one-body density, and these properties are a functional of the density. This provides a time-dependent analogue to the standard Hohenberg-Kohn theorems. Using the KS theory for DFT described in section **2.6,** where an auxiliary system of non-interacting electrons subject to a local potential v_{KS}, this can be applied to a time-dependent system obeying the time-dependent Schrödinger equation for a single electron, with the following Hamiltonian $\hat{H}$:

$$\hat{H}_s(t) = \hat{T} + \hat{V}_s(t) \tag{2.118}$$

where the subscript s refers to a KS non-interacting system, $\hat{T}$ is the kinetic energy and $\hat{V}_s(t)$ the time-dependent potential energy. This can be expanded to use known terms for the Hamiltonian components and placed in context of a time-dependent Schrödinger equation.

$$i\frac{\partial}{\partial t}\psi_i(\boldsymbol{r},t) = \left[-\frac{\nabla^2}{2} + v_{KS}(\boldsymbol{r},t)\right]\psi_i(\boldsymbol{r},t) \tag{2.119}$$

where the density of the time-dependent KS orbitals are

$$\rho_s(\boldsymbol{r},t) = \sum_{i=1}^{N}|\psi_i(\boldsymbol{r},t)|^2 \tag{2.120}$$

As before with regular KS DFT, the density of the reference system is the same as the density of the true system

$$\rho_s(\boldsymbol{r},t) = \rho(\boldsymbol{r},t) \tag{2.121}$$

The part of these equations that is unknown is the time-dependent potential, $v_{KS}(\boldsymbol{r},t)$. This consists of the sum of the external potential of the system v_{ext}, the Coulombic interaction v_J and the exchange correlation potential v_{xc}, with all these potentials being dependent on both position and time.

$$v_s(\boldsymbol{r},t) = v_{ext}(\boldsymbol{r},t) + v_J(\boldsymbol{r},t) + v_{xc}(\boldsymbol{r},t) \tag{2.122}$$

The most popular formalism of TDDFT involves linear response to the external potential formalised by Casida [41, 42]. This calculates poles in the response to a time-varying applied external field. These poles correspond to the excitation energies. TDDFT is commonly used within the Tamm-Dancoff approximation [43], where the excitation energies of a system are determined in the following eigenvalue equation.

$$\mathbf{AX} = \omega\mathbf{X} \tag{2.123}$$

where **X** corresponds to the oscillator strengths, ω are the excitation energies and **A** is given by the following expression

$$A_{ia\sigma,jb\tau} = \delta_{ij}\delta_{ab}\delta_{\sigma\tau}(\varepsilon_{a\sigma} - \varepsilon_{i\tau}) + (ia\sigma|jb\tau) + (ia\sigma|f_{XC}|jb\tau) \tag{2.124}$$

where ε_i are orbital energies and

$$(ia\sigma|jb\tau) = \int\int \frac{\Psi^*_{i\sigma}(\boldsymbol{r}_1)\Psi_{j\tau}(\boldsymbol{r}_2)\Psi_{b\tau}(\boldsymbol{r}_2)}{r_{12}} d\boldsymbol{r}_1 d\boldsymbol{r}_2 \tag{2.125}$$

$$(ia\sigma|f_{XC}|jb\tau) = \int \Psi^*_{i\sigma}(\boldsymbol{r}_1)\Psi_{a\sigma}(\boldsymbol{r}_1)\frac{\partial^2 E_{XC}}{\partial\rho_\sigma(\boldsymbol{r}_1)\partial\rho_\tau(\boldsymbol{r}_2)}\Psi_{j\tau}(\boldsymbol{r}_2)\,\Psi^*_{b\tau}(\boldsymbol{r}_2)d\boldsymbol{r}_1 d\boldsymbol{r}_2 \tag{2.126}$$

where E_{XC} is the exchange correlation functional. This allows excitation energies to be calculated for a system.

2.7.1.2. Lamba (Λ) Analysis of TDDFT Calculations

Although TDDFT gives good results for low-lying valence states, for higher energy Rydberg states and CT states, these energies are poorly modelled, as has been previously described [30]. Long-range-corrected functionals have already been discussed as a way to avoid this shortcoming of TDDFT, however it is important for a quantum chemist to be aware of how good or poor a particular functional of any type would perform for these Rydberg and CT states. There has been a method developed to quantify how well a particular functional models CT states, first suggested by Peach, Benfield, Helgaker and Tozer [44]. They introduced a quantity, Λ (Lambda), which gives information on the spatial overlap between orbitals in a given excitation, and returns a value between zero and one, with a higher value corresponding to a lower deviation in energy from gas-phase experimental and high-accuracy wavefunction methods. They suggested that

$$\Lambda = \frac{\sum_{i,a} \boldsymbol{k}_{ia}^2 \, O_{ia}}{\sum_{i,a} \boldsymbol{k}_{ia}^2} \tag{2.127}$$

where i and a correspond to occupied and virtual orbitals respectively, and O_{ia} is given by the overlap integral of orbitals i and a,

$$O_{ia} = \langle |\psi_i| | |\psi_a| \rangle = \int |\psi_i^*(\boldsymbol{r})| \, |\psi_a(\boldsymbol{r})| d\boldsymbol{r} \tag{2.128}$$

and $\boldsymbol{k}_{ia}$ is the addition of the two solution vectors from the TDDFT eigenvalue equation

$$\boldsymbol{k}_{ia} = X_{ia} + Y_{ia} \tag{2.129}$$

This Λ analysis was applied in chapter 4, where charge transfer state and their energies helped describe the fluorescent activity of a potassium cation sensor.

2.7.2. Maximum Overlap Method

One approach to calculating excited states is to explicitly model the state of interest within an SCF calculation. In a regular SCF calculation relying on a standard iterative procedure, such as the direct integration of iterative subspace (DIIS) method, after each step in the SCF cycle a new set of orbitals are chosen based on lowering the energy of the previous set of orbitals, thus the energies of the orbitals are minimised over subsequent steps. After an energy-minimising SCF cycle to give the optimum ground-state orbitals of a system it is possible to promote an electron from an occupied to a virtual orbital, however this approach gives poor energies, as the orbitals are only optimal for the ground state and are not able to relax after electronic excitation. The maximum overlap method (MOM) [45] aims to provide an alternate method to converging SCF calculations based on orbital overlap as opposed to energies.

Within the SCF eigenvalue problem, the MOM states that the *new occupied orbitals should be those that overlap most with the span of the old occupied orbitals.* The overlap matrix $\boldsymbol{O}$ of the orbitals is defined as:

$$\boldsymbol{O} = (\boldsymbol{C}^{old})\boldsymbol{S}\boldsymbol{C}^{new} \tag{2.130}$$

where $\boldsymbol{C}^{old}$ is the old coefficient matrix in the SCF process, $\boldsymbol{C}^{new}$ is the new coefficient matrix and $\boldsymbol{S}$ is the basis function overlap matrix. The general term O_{ij} is the overlap between the i-th old orbital and the j-th new orbital in the system. The projection p_j of the j-th orbital onto the old occupied space is expressed as:

$$p_j = \sum_{j}^{n} O_{ij} = \sum_{v}^{N} \left[\sum_{\mu}^{N} \left(\sum_{i}^{n} C_{i\mu}^{old} \right) S_{\mu v} \right] C_{vj}^{new} \tag{2.131}$$

The MOM then proceeds to calculate a full set of p_j values for a system, which is computationally negligible in cost on top of a regular SCF procedure, and then occupies the n orbitals with the largest projections p_j. This allows the convergence of excited state solutions which can be treated in a quantum chemical software package as a ground state, allowing geometry optimisations and calculations of properties easily for the excited state, as well as energies of excited states.

The MOM does have its shortcomings however. Due to the way it converges the orbitals of a system, if the orbitals of the electronic ground state or an alternate excited state are similar to the excited state of interest, the MOM may collapse to the ground state. Thus, some states for some systems are near impossible to converge using the MOM. Also, it is essential to know the shape and relative energies of orbitals involved in a transition before calculating the excited state. This is in contrast to methods such as TDDFT which will directly calculate which orbitals are involved in an excitation, even without prior knowledge of the orbitals in a system.

When the MOM is able to converge an excited state of interest, it has been known to give accurate result [46-48], although excitation energies for open-shell singlet states involving excitation to valence orbitals are often underestimated. This is due to the open-shell singlet state being described by a single determinant to give a spin-mixed state. Excitation energies can be significantly improved by applying a post-SCF spin-purification correction suggested by Ziegler [49].

$$E = 2E_S - E_T \tag{2.132}$$

where E is the true (spin-purified) singlet energy, E_S the spin-mixed (single determinant) singlet energy and E_T the energy of the corresponding triplet state. This is rationalised by knowing that the separation between the triplet and spin-mixed singlet

states is roughly the exchange energy K between the two unpaired electrons, as well as the spin-mixed singlet and spin-pure singlet energy separation being K. This gives the expression

$$E = E_T + 2K \tag{2.133}$$

which can be shown to be $2E_S - E_T$ when E_S and E_T are rearranged in terms of E_T and K. In this work calculations which have been spin corrected are referred to as spin-mixed MOM (SM-MOM), whereas calculations using the spin-purification post-SCF method are known as spin-pure (SP-MOM).

2.7.3. Equations of Motion Coupled Cluster

Another method for calculating excited states is by using coupled-cluster theory with the equations-of-motion method (EOM-CC). This procedure calculates excited states by diagonalising a similarity transformed Hamiltonian matrix [50]. This is often used in conjunction with CCSD theory [17], as encountered in chapter 5 on this work. EOM-CC theory follows on from the ground-state Schrödinger equation for a system by introducing Schrödinger equations for two states, a ground-state 0 and an excited state k.

$$\hat{H}\Psi_0 = E_0\Psi_0 \tag{2.134}$$

$$\hat{H}\Psi_k = E_k\Psi_k \tag{2.135}$$

The excited state wavefunction can be described as the ground-state wavefunction acted on by some operator $\hat{\Omega}_k$.

$$\Psi_k = \hat{\Omega}_k\Psi_0 \tag{2.136}$$

Combining the above equations by subtracting Eq. (2.134) from Eq. (2.135) to give an expression for the energy gap between two states, $\omega_k = E_k - E_0$, then substituting into Eq. (2.136) gives

$$\left[H, \hat{\Omega}_k\right]\Psi_0 = \omega_k\hat{\Omega}_k\Psi_0 \tag{2.137}$$

Different choices of $\hat{\Omega}_k$ can be used to define different excited states.

Coupled-cluster can be introduced to the EOM equations above by using the familiar notation for the exponential operator $\hat{T}$.

$$\Psi_0 = e^{\hat{T}}\Phi_0 \tag{2.138}$$

For any choice of $\hat{\Omega}_k$, $\left[\hat{\Omega}_k, \hat{T}\right] = 0$, so the equations can be expressed as

$$\left[\bar{H}, \hat{\Omega}_k\right]\Phi_0 = \left(\bar{H}, \hat{\Omega}_k\right)_c \Phi_0 = \omega_k \hat{\Omega}_k \Phi_0 \tag{2.139}$$

where

$$\bar{H} = e^{-\hat{T}} H e^{\hat{T}} \tag{2.140}$$

All of the ground state CC information is contained in $\bar{H}$. EOM-CCSD is computationally expensive, so is often applied for accurate calculations of small molecular systems, as encountered in chapter 5 of this thesis.

2.8. Configuration Interaction and Complete Active Space Methods

Electron correlation methods such as perturbation theory and coupled-cluster approaches have already been discussed. Correlation energy can also be accounted for through the related methods configuration interaction and complete active space methods. Configuration interaction (CI) improves of the HF wavefunction by adding onto the HF wavefunction determinants that describe the promotion of electrons from occupied to virtual (unoccupied) orbitals. The total wavefunction can be described as

$$\Psi = c_1 D_1 + c_2 D_2 + c_3 D_3 + \cdots + c_i D_i \tag{2.141}$$

Where D_1 is the HF determinant, D_2 through to D_i are the determinants of the system with electrons promoted to virtual orbitals, and c_2 through to c_i are constants. This can lead to the expression

$$\Psi_{CI} = \Psi_{HF} + \sum_I a_I \Psi_I \tag{2.142}$$

Where Ψ_{CI} is the CI wavefunction, Ψ_{HF} is the HF wavefunction and $\sum_I a_I \Psi_I$ corresponds to the sum of all the excitation wavefunctions. If every single possible electronic state of a system is modelled using CI, the wavefunction would be a full CI wavefunction. Due to the need for a reasonably-sized basis set for CI calculations to give reliable results, paired with the large number of possible excitation wavefunctions in systems larger than a few electrons, full CI is prohibitively expensive for most systems, and is usually restricted to calculations on very small systems.

There are various ways of truncating the amount and type of excitations considered in these sort of calculations, such as only including single and doubles excitations (CISD). One other way of including excitations, which is more thorough than CISD and much

less expensive than full CI, is referred to as complete active space self-consistent field, or CASSCF calculations [51]. In CASSCF, molecular orbitals are split into three types of orbitals: core orbitals, active orbitals, and virtual orbitals. CASSCF seeks to calculate all combinations of electronic excitations for only the active orbitals. This is analogous to full CI, except the active orbital space is much smaller than the whole molecular system. In the CAS framework, core orbitals are always occupied and virtual orbitals always empty, whereas the active space consists of the highest occupied and lowest unoccupied orbitals in the system.

An extension to the regular CASSCF procedure is CASPT2 [52], which introduces dynamic correlation effects into the regular CASSCF calculation, by adding in a second order perturbation, in much the same way as MP2. This method was included in chapter 3 for accurate structural analysis of the BODIPY core.

2.9 Molecular Dynamics

All of the previously described methods are quantum mechanical methods, and aim to solve some approximation of the Schrodinger equation. Due to the computational expense of these methods, they are usually restricted to systems of around 100 atoms or smaller, depending on the level of theory used. For larger systems, such as a solvated system or a cell membrane, other approaches to modelling systems must be considered, such as classical molecular dynamics (MD). MD is a simulation method used to study the movement of atoms and molecules in a system over time. The most common formalism of MD determines the trajectories of atoms and molecules by numerically solving Newton's equations of motion, where forces and potential energies of molecules are determined by a set of forces known as a force field.

A general MD simulation will undergo the following procedure:

1. Give atoms in system initial position $\boldsymbol{r}^{(i=0)}$ and velocity $\boldsymbol{v}^{(i=0)}$ for the initial time step $i = 0$, set the acceleration $\boldsymbol{v}$ and time t to 0 and choose a short time step Δt.
2. Predict the next atom positions $\boldsymbol{r}^{p}$ and update velocities $\boldsymbol{v}^{p}$.
3. Get forces $\boldsymbol{F}$, either from classical interatomic potentials (Eq. 2.143) or quantum mechanical methods (Eq. 2.144). Obtain acceleration of the atoms $\boldsymbol{a}$ from Eq. (2.145)

$$\boldsymbol{F} = -\nabla V(\boldsymbol{r}^{p}) \tag{2.143}$$

$$\boldsymbol{F} = \boldsymbol{F}[\Psi(\boldsymbol{r}^{p})] \tag{2.144}$$

$$\boldsymbol{a} = \frac{\boldsymbol{F}}{m} \tag{2.145}$$

4. Correct the atom positons based on the new acceleration $\boldsymbol{a}$, and move atoms accordingly to obtain new positions $\boldsymbol{r}^{(i)}$ and velocities $\boldsymbol{v}^{(i)}$.
5. Apply boundary conditions to the system, as well as temperature and pressure controls.
6. Calculate physical properties of interest.
7. Move time step forward so $i = 1$ and $t = t + \Delta t$.
8. Repeat steps 2 through to 7 for the necessary number of time steps.

Popular force fields used include CHARMM [53] and AMBER [54]. The number of time steps and the size of the steps, as well as force field choice and boundary conditions, vary depending on the aims of the calculation. In this work classical molecular mechanics is combined with *ab initio* methods as detailed below. Solvent was considered when modelling the excited state dynamics of BODIPY: this was modelled using the TIP3P solvent method [55]. This is one of the most popular solvent methods applied to molecular simulations, and is a rigid solvent model that relies on non-bonding interactions, where the interaction with the water solvent and the rest of the system E_{ab} is represented by

$$E_{ab} = \sum_{i}^{a} \sum_{j}^{b} \frac{k_C q_i q_j}{r_{ij}} + \frac{A}{{r_{OO}}^{12}} + \frac{B}{{r_{OO}}^{6}} \tag{2.146}$$

where k_C is an electrostatic constant, q_i and q_j are partial charges of atoms in the system, with r_{ij} corresponding to separation between the two atoms. A and B are Lennard Jones parameters, with r_{OO} corresponding to the distance between oxygen atoms in the water model. TIP3P is known as a three-site solvent model, meaning only the three atoms in the water are considered; higher orders are possible, by adding dummy atoms and lone-pair sites to the water model.

2.9.1 *Ab initio* Molecular Dynamics

Ab initio molecular dynamics (AIMD), as its name implies, is a technique that employs part quantum-mechanical *ab initio* calculations within classical MD simulations. A similar technique to classical molecular mechanics, AIMD instead uses a quantum mechanical method to calculate energies and forces, as opposed to the classical mechanics of regular MD. In this project DFT is used to calculate the energy in AIMD simulations, and the specific AIMD method used is known as Born-Oppenheimer molecular dynamics (BOMD) [56]. Within this technique, classical molecular dynamics trajectories on the Born-Oppenheimer potential energy surface are generated by a particular theoretical model chemistry, such as DFT with a particular functional and basis set. This method calculates the forces on the nuclei for the MD simulation on-the-fly. A BOMD calculation consists of an energy calculation along with a gradient calculation at each molecular dynamics time step, and can be combined with excited state methods, such as the MOM described earlier in section **2.7.2.** to give the dynamics of an excited state system. BOMD has been implemented on the BODIPY fluorophore in chapter 3 to calculate ground and excited state geometries over a BOMD simulation, so structures can be extracted and excitation energies computed for a range of structures.

Ab initio molecular dynamics can be performed on a single molecular system of choice or be combined with classical molecular mechanics to simulate its behaviour in a solvent or membrane. These types of calculations are known as quantum mechanics/ molecular mechanics (QM/MM) calculations [57], and allow accurate *ab initio* methods to be applied to the molecule of choice, while still modelling its surroundings albeit in an approximate way.

2.10 Geometry Optimisation

One important aspect of the work involved in this thesis concerns the optimisation of a system's geometry so that the energy of a particular state or system is at a stationary point of its PES. Geometry optimisation involves modifying a starting geometry, with knowledge of its energy and first and second derivatives, to produce a revised geometry closer to the desired stationary point. These calculations take the form of a number of subsequent SCF cycles in which the amount of these cycles needed is affected by both the geometry optimisation algorithm used, the starting geometry of the molecular system, and the complexity of the PES.

Geometry optimisation algorithms commonly follow the form

$$\boldsymbol{h} = -\boldsymbol{H}^{-1} g \tag{2.146}$$

Where $\boldsymbol{h}$ is the displacement from the starting geometry on a particular cycle, g is the first derivative (gradient) of the energy, and $\boldsymbol{H}$ is the second derivative (Hessian) of the energy. Geometry optimisation algorithms aim to calculate $\boldsymbol{h}$ in the most efficient way depending on the initial atomic coordinates within the system and the gradient. In the following work, geometry optimisation has been implemented within the Q-CHEM software package using the default settings, which allows a variety of optimisation algorithms to be used, which is decided on by the software.

2.11 Polarisable Continuum Solvation Model

The modelling of solvent within quantum chemical calculations is often essential, as the effects of solvent on molecular properties such as polarizability and the energy of charge transfer states cannot be ignored for many systems. Along with the previously described explicit solvent model of TIP3P and similar, it is also possible to apply implicit solvent models within quantum chemical calculations. This can offer a great reduction in computational expense when compared to explicit models. The polarisable continuum solvation model (PCM) has been used at various points throughout this work.

PCM methods are also known as "apparent surface charge" solvation models, as they model solvent in such as a way to form a surface of charge points around a molecular system. By default, the Q-CHEM software will calculate a solute cavity from a union of atom-centred spheres with radii around 1.2 times that of the atomic van der Waals radii. This cavity surface is then converted to a number of Lededev grid points (the same as those implemented during DFT calculations to model electron density) to create a surface of charges. These charges are relative to the solvent the user wishes to model, and is specified with the parameter ε, the dielectric constant.

3. QM/MM Excited State Molecular Dynamics and Fluorescence Spectroscopy of BODIPY

3.1. Introduction

One frequently used class of fluorescent molecules involves dyes derived from 4,4-difluoro-4-bora-3a,4adiaza-s-indacene, also known as *bo*ron *dipy*rrin or *bo*ron *dipy*rromethene dyes, commonly abbreviated to BODIPY [58]. First synthesised in 1968 [58], BODIPY has seen a surge of popularity in the past 20 years [1, 60, 61]. This recent success is due to the ever-increasing applications of fluorescent molecules along with BODIPYs favourable and highly versatile photochemical properties, which can be varied by chemical substitutions around the BODIPY fluorophore, allowing a wide variety of functionalisation [60, 62-72].

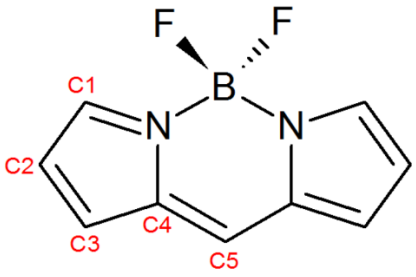

Figure 3.1. *Structure of the BODIPY fluorophore with relevant stereochemistry and labelled carbon atoms.*

The BODIPY fluorophore consists of an aromatic ring system containing a dipyrromethene core bridged by a boron-difluoro group, as shown in ***Figure 3.1.*** It is this aromatic planar structure that gives the fluorophore its fluorescent properties through a strong $\pi \rightarrow \pi^*$ transition from the highest-occupied molecular orbital (HOMO) to the lowest-unoccupied molecular orbital (LUMO). This is of particular importance

as BODIPY absorbs and emits photon from this transition in the visible region, giving rise to absorption and emission spectra usually in the 500 nm to 600 nm range with small well defined bandwidths for many derivatives. The combination of large molar absorption coefficients, fluorescence quantum yields (*Φ)* and high photostability make BODIPY an ideal fluorophore from a theoretical perspective [1].

Above all, the popularity of BODIPY is due to the variety of practical applications of the different derivatives, allowing tunability of photochemical and physical properties. This is possible due to BODIPYs chemical structure, as substitution of a variety of moieties is possible on the C1, C2, C3 and C5 positions [1]. This allows a variety of substituents that can modify the photophysical and spectroscopic properties of the resultant molecule. It has been found that these properties are often most sensitive to substituents at the *meso*-position of the BODIPY core, being the position opposite the boron atom in the 6-membered ring (C5). This has been found through quantum chemical calculations showing a significant increase in electron density at the *meso*-position during the $\pi \rightarrow \pi^*$ transition [73], due to a node in the HOMO at the *meso*-position, which is not present in the LUMO. In ***Figure 3.2.***, it is seen the LUMO of the BODIPY core molecule has electron density centred on the *meso*- carbon, which when compared to the HOMO shows the largest change in electron density compared to any other position between the two molecular orbitals. This large change in electron density can be further affected by the substituent attached to the *meso*- position.

Varying substituents on the *meso*-position can give rise to a variety of different photophysical properties in a BODIPY dye. The addition of electron-withdrawing groups such as CF_3 to the *meso*-position significantly lowers the energy of the HOMO to LUMO transition, giving a rise in wavelength, or redshift, to the resulting absorption and emission spectra [74-76] when compared to traditional BODIPY dyes [1, 60] and

the BODIPY core [77]. Similarly, addition of a *meso*-CN group to a BODIPY dye also sees a redshift [78], which is particular to addition at the *meso*-position. This is due to the electron withdrawing nature of the cyano group stabilising the LUMO, though not the HOMO due to the *meso*-position node in the BODIPY HOMO, leading to a decrease in the energy gap [1].

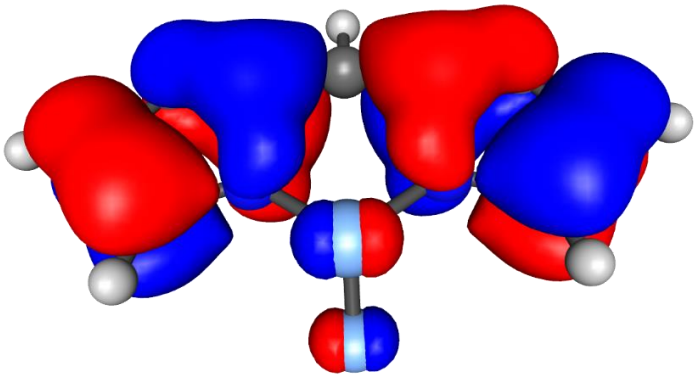

(a)

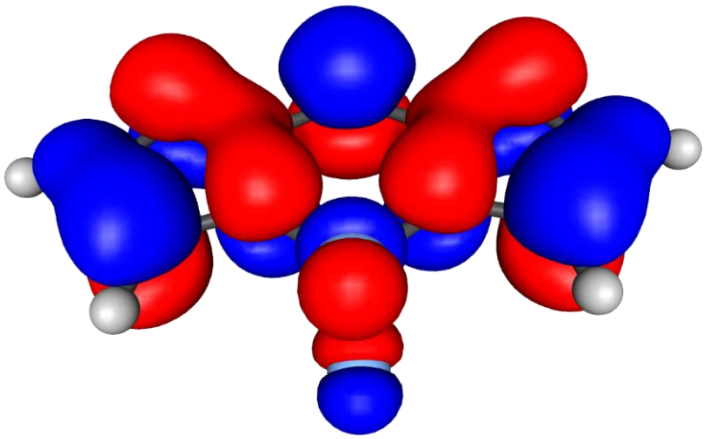

(b)

Figure 3.2. *The HOMO (a) and LUMO (b) molecular orbitals of the BODIPY core responsible for the π→π* transition.*

Substituting electron-donating groups such as NR_2 or OR to the *meso*-position has the opposite effect to electron-donors, showing blueshifted absorption and emission spectra when compared to unsubstituted and classic BODIPY dyes [79-88]. Alkylation of the *meso*-position gives minimal change to the fluorescence properties of a BODIPY dye [73, 89-91]. These well-defined effects of *meso*-substituents on a BODIPY dye allow a large degree of tunability and properties which can be theoretically modelled.

3.1.1. Applications of BODIPY

The applications of fluorescent molecules based on the BODIPY fluorophore are both numerous and varied. One of the earliest applications of BODIPY has been as the lasing medium in a dye laser [92], and research into these dyes, known as pyrromethene (PM) dyes, continues to be a thriving area of research. Many PM dyes are commercially available, and many studies on their properties and activity have been carried out. One study on the dyes PM567, PM580 and PM597 showed the dyes to be highly efficient, with a wide tuning range when compared with more traditional rhodamine (RN) dye, despite their low fluorescence yield and high rate of non-radiative decay [93]. These PM dyes have also been modified in various ways, such as the addition of polymerisable methacryloyloxypropyl groups to the PM567 dye with an aim to enhance the laser action of the dye [94]. Although PM dyes outperform RN dyes, they experience rapid photodegradation in common ethanol and methanol solvents, which limit their uses in high power liquid dye lasers. Work has gone into extending the use of PM567 and PM597 in these lasers, finding nonpolar n-heptane as a good substitute for ethanol in high power lasers [95].

There is also ongoing development of new PM laser dyes, such as the combination of extending π-conjugation and tuned intramolecular charge transfer, to synthesise a novel PM dye that exhibits highly efficient and stable laser emission tunable in the green and near-infrared (NIR) region (570–725 nm) in both polar and nonpolar solvents [96]. PM dyes have also been chlorinated, which yields enhanced laser action compared to non-halogenated PM dyes, in both liquid and solid phase [97]. The efficiency of PM dyes, combined with their versatility along with various efforts to overcome some of their problems, makes PM dyes a continuously popular lasing medium.

There is an extensive ongoing effort to synthesise BODIPY derivatives for new applications, for example, in fluorescent switching and chemical sensing, which has uses in optical memory storage and electronics [98], where a fluorescent on/off sensor can mimic traditional processor behaviour in electronic devices. BODIPY derivatives can be used to form highly efficient, reversible fluorescent switches [99], where the fluorescence of a BODIPY-containing molecule undergoes a known change in response to a change to its environment, either through photon-induced electron transfer [100] or UV light induced isomerisation [101], with some dyes being used to imitate photobiological processes found in cells [102].

BODIPY derivatives also have applications in organic light emitting diodes (OLED's) [103], where BODIPY derivatives have been shown to have promising characteristics as a solid state dopant in the deep blue region [104], as well as energy transfer cassettes where BODIPY-based compounds are used for the storage of solar energy [105, 106]. The light-harvesting properties of BODIPY have also been applied to the development of dye-sensitised solar cells [107, 108], where BODIPY moieties have been modified to accept electrons in a charge transfer mechanism to produce an electric current. BOPDIPY dyes have been shown to form the basis of photodynamic therapy, a process where the triplet state of a fluorophore (in this case BODIPY) can interact with triplet state oxygen in a cell to cause oxidative damage to specific cells [109]. One novel application of a BODIPY dye was to attach two electron-donating macrocyclic binding units with different metal ion preferences, which enable the dye to operate as an ionically driven molecular Implication gate, capable of reading Boolean operations [110].

BODIPY dyes have been designed as on/off fluorescent sensors to detect the presence of metal cations in biological systems, by utilising a metal chelator group attached to

the BODIPY fluorophore. This is a versatile approach which can be applied to a variety of metal ions, such as Ca^{2+} [111, 112], Cu^{2+} [113, 114], Zn^{2+} [115], Hg^{2+} [116, 117] and Pb^{2+}[118], as well as other molecules such as nitric oxide [84], and these are often used in biological systems to detect ion through changes in fluorescence. Results on the potassium cation sensor KS1 [2] will be presented later in this thesis, with the focus on understanding the mechanisms involved in the fluorescence activity of the sensor with and without K^+ bound to the molecule.

Fluorescent molecular probes work by adding a fluorophore to groups which interact with a biological system. By monitoring the fluorescence of the system, it can reveal the conditions of the biological system the molecule is in, with properties such as pH and solvent environment being readily deducible from well-known systems with sensitivity to these conditions [115, 119, 120].

BODIPY derivatives have been used in biological systems, as fluorescent probes to study membrane lipid domains [121], and proteins to probe their activity [122-125]. Due to its hydrophobic nature, BODIPY has been used in studies where a cholesterol group has been added to the *meso*-position of the BODIPY core [121, 126-128]. The biological activity of the cholesterol group is maintained, while the fluorescent nature of BODIPY is also little affected. BODIPY has been used to label biologically active molecules such as opioids, where fluorescence of the BODIPY-opioid molecule has been used to monitor how the drug has distributed itself in monkey brains among other biological environments [129, 130]. Other biologically active molecules can have their activity and distribution monitored by selective BODIPY-based sensors [131, 132]. The BODIPY group has also been added to porphyrin rings [133], an important group in metalloproteins such as haemoglobin, which could help probe the activity of such proteins, or further the field of BODIPY as a metal sensor. Other novel uses of BODIPY

derivatives in biological applications involves their use in synthesising light-harvesting arrays, to mimic processes like photosynthesis [134-136].

One main factor in using fluorescent probes is how their fluorescence responds to the molecular environment. The solvatochroism of absorption and emission bands of a number of BODIPY based molecules has been reported. Studies have shown that the observed spectral shifts are primarily dependent on solvent polarisability [137] or solvent polarity, with hydrogen bonding being of less importance [138]. In particular, BODIPY derivatives have solvatochromic shifts dependent upon the polarisability of the solvent immediately surrounding the dye [139, 140].

The applications discussed for chemical sensing using BODIPY derivatives can be readily extended into the biological field. This has been used to investigate the activity of newly discovered drugs in the body [133], and to probe the abundance of antibodies in cells, such as the recently discovered glucagon yellow compound, which is a selective sensor to the antibody glucagon [141]. BODIPY derivatives can also be used to sense nitric oxide in biological systems, using a derivative known as DAMBO [142], as well as investigate nitration of aromatic rings in biological systems using a type of BODIPY derivative known as a NiSPY [143].

Overall the uses of BODIPY based fluorophores are numerous and the applications of these molecules are ever increasing. For such a widely expanding field, computational studies into properties and photochemistry of BODIPY and its derivatives can be a useful tool in predicting and designing new derivatives, and new uses for them.

3.1.2. Computational studies of BODIPY

One issue when studying molecules such as BODIPY is modelling them in complex environments such as a solvent or lipid membrane, which is further complicated by the need to simulate fluorophores in the excited state when modelling emission. BODIPY and related molecules have previously been studied using a combination of DFT and TDDFT to model the absorption and emission spectroscopy [93, 131, 143-149], as well as addressing the choice of exchange-correlation functional [150].

TDDFT calculations carried out using the B3LYP exchange-correlation functional on the laser dye PM567, comprising of BODIPY with ethyl groups bonded at the C2 positions and methyl groups at the C1, C3 and C5 positions showed a smaller dipole moment in the S_1 state. The computed transition energies were 0.4-0.5 eV larger than experiment [145]. In these studies the solvent is modelled using an implicit solvent model, the PCM, however it is also possible to model solvent using a combination of classical MD simulations and TDDFT, where structures from an MD simulation are used in subsequent TDDFT calculations. Examples of this approach have been reported for the molecules hydroxytryptophan in solution [151], within proteins [152] and for molecular probes within a membrane bilayer environment [153, 154].

Another approach to studying the ground and excited state of BODIPY is by using semiempirical methods, such as the sempiempirical intermediate neglect of differential overlap/ singles-configuration interaction method (INDO/SCI). This has been used to obtain geometry optimisations of the ground and excited state, and the calculation of radiative lifetimes of the various BODIPY derivatives [155-157]. These studies have also identified how various factors can affect spectral shifts, with qualitative and quantitative agreement with the presented experimental evidence.

The limitation of the approaches previously described is that for MD the derivation of force field parameters for the excited state simulations are often based on ad hoc charges derived from quantum mechanical gas phase excited state calculations. A more theoretically consistent method is to use quantum chemical methods such as DFT directly in the MD simulations. Although this results in a large increase in computational expense, modern computational resources allow for molecules the size of BODIPY to be modelled in this way. It is even possible to incorporate an extended molecular environment such as solvent using a hybrid quantum mechanics/molecular mechanics (QM/MM) approach.

The QM/MM approach has been previously applied to study the excited state dynamics and emission spectrum of the first singlet excited state of acetone in water within restricted open-shell Kohn-Sham and TDDFT formalisms [158]. This showed that a purely classical description of the water was consistent with results treating the first solvent shell of the system in a quantum mechanical way. A similar methodology has been applied to investigate the excited state dynamics and proton-electron transfer in guanine [159] and the excited state dynamics of pyrrole-water clusters has also been studied [160].

Not all theoretical studies are directly aimed at modelling fluorescence of the molecule. There have been studies on BODIPY derivatives concerning fluorescence quenching processes of heavy metal ion sensing BODIPY [161]. DFT and TDDFT have been used to investigate an Hg^{2+} cation sensor, showing the quenching of fluorescence was due to the photo-induced electron transfer (PET) process. One other study used DFT with B3LYP to estimate HOMO and LUMO energies of modified PM laser dyes, though results were underestimated by up to 100 nm in comparison with experiment [162]. Computational studies of BODIPY derivatives have also been extended to the

adsorption of BODIPY molecules on surfaces, such as the aza-BODIPY molecule near a gold surface using DFT [163]. This was compared with a complementary scanning-tunnelling microscope procedure to compare the theoretical results with experiment.

Overall BODIPY derivatives have had limited investigation from a computational viewpoint with respect to their numerous applications, and there is much more that could be done with this fluorophore from a theoretical perspective. In this chapter we describe a QM/MM study of the excited state dynamics, absorption and emission spectra of BODIPY in gas phase and in water, as well as structural analysis of various BODIPY and *meso*-BODIPY dyes. In both the molecular dynamics and subsequent calculations of the spectroscopy, the electronic structure of the BODIPY molecule is described using DFT, while the solvent is treated classically.

3.2. Computational Details

Structures were optimised for the ground state (S_0) and first singlet excited state (S_1) of the BODIPY core and the dyes PM567, PM580 and PM597 using unrestricted DFT with the B3LYP exchange correlation functional and the 6-311G** basis set. The BODIPY core molecule was also optimised at the DFT/B3LYP/6-31G level of theory to compare how different optimisations affect the transition energies. To study the first excited singlet state within Kohn-Sham DFT, the maximum overlap method (MOM) [45] was employed to converge the SCF calculation to an excited state electronic configuration. This allows optimisation of the S_1 state, as well as the determining of transition energies using a ΔSCF procedure. As well as computing the singlet excited energies using MOM, the Ziegler post-SCF spin-purification correction ($2E_S$-E_T) was also applied to excitations. Calculations for the excited state that have not been spin-corrected are referred to as spin-mixed MOM (SM-MOM). Calculations that have undergone the spin-purification correction are known as spin-pure MOM (SP-MOM).

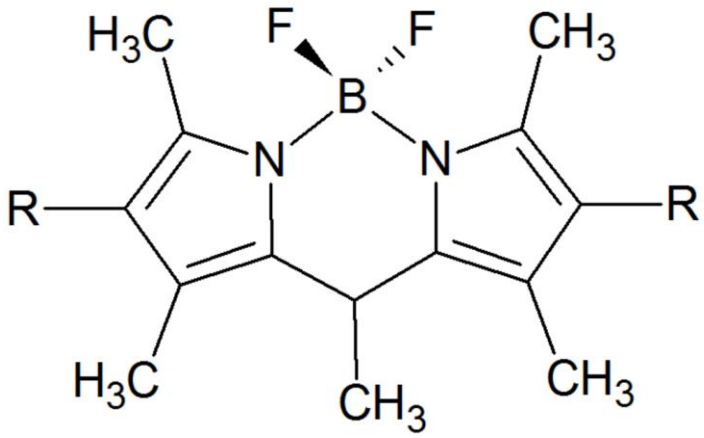

Figure 3.3. *General structure of PM dyes used in this study. (PM567: R=CH_2CH_3, PM580: R=$(CH_2)_3CH_3$, PM597: R=$C(CH_3)_3$).*

To produce reference data to compare to the DFT calculations, geometry optimisations for the S_0 and S_1 of the BODIPY core molecule were performed by David Robinson using the complete active space self-consistent field (CASSCF) with multi-configurational perturbation theory (CASPT2) [51, 52] using the 6-31G* basis set with no symmetry constraints. The active space of the CASSCF wave function consisted of the π-bond system (12 electrons in 12 orbitals) giving 226,512 symmetry adapted configuration state functions. From these CASPT2 structures the absorption and emission vertical excitation energies were calculated using the larger ANO-L basis set [164], contracted to 4s3p2d for non-hydrogen atoms in the system. CASSCF/CASPT2 calculations were carried out using the MOLCAS software [165].

Important structural parameters of the BODIPY core and PM laser dyes from the DFT/B3LYP/6-311G** optimisations were measured, along with the BODPIY core molecule.

AIMD simulations were performed on the BODIPY molecule in gas phase for the ground and first excited singlet state at the B3LYP/6-31G level of theory. This small basis set was used so a direct comparison could be made with QM/MM simulations also undertaken. Simulations ran for 120fs with a 0.24fs time step. Initial velocities for the system were from a Maxwell-Boltzmann distribution, with the first 60fs of the simulation consisting of equilibration steps, with velocities scaled to 298K for the first 100 time steps. The structures from the last 250 time steps were used for the subsequent calculations of absorption and emission spectra.

To model the BODIPY molecule in a condensed phase, a QM/MM approach was applied by David Robinson where BODIPY was treated using DFT/B3LYP/6-31G and the solvent treated classically using the commonly used TIP3P potential [55]. These

simulations were carried out using Q-Chem/CHARMM interface [57], at atmospheric pressure and temperature (300K). Periodic boundary conditions were used on the system in the form of a truncated octahedron with a box-length of 29.091 Å. The BODIPY core was treated quantum mechanically using B3LYP/6-31G. The excited state was simulated following an initial ground state followed by MOM procedure to generate excited state orbitals for BODIPY using SP-B3LYP/6-31G.

Both QM/MM systems were heated and equilibrated for 10ps. The simulations were allowed to run indefinitely to obtain as many structures as possible, hence the difference in the amount of structures sampled for the ground and excited states. Structures were taken at 2ps intervals after the initial heating period, and used for subsequent calculations. A total of 129 structures for the ground state and 49 structures for the excited state were produced. Spectra from these structures and those from the gas phase simulations were generated by representing the transition energy and oscillator strength for each structure by a Gaussian function with a full width at half-maximum of 0.2 eV and area equal to the oscillator strength, centred on the transition energy. The averages of important structural parameters of the S_0 and S_1 states of the BODIPY core were calculated for both the gas and solvent phases.

Three *meso*-BODIPY structures (**1-3**, see ***Figure 3.4.***) were optimised at the ground state (S_0) and first singlet excited state (S_1) using unrestricted DFT/B3LYP/6-311G*. In order to study the first singlet excited within Kohn-Sham DFT, a ΔSCF approach using SP-MOM was employed. Solvation was taken into account using the PCM, with a dielectric constant set to 9.08. Structural parameters of these structures were observed.

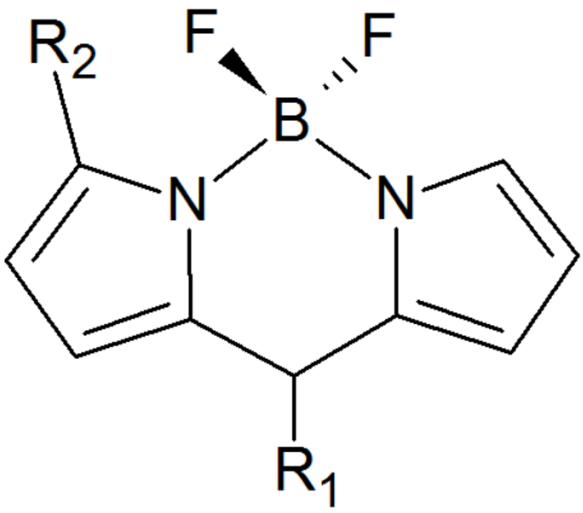

Figure 3.4. *General structure of meso-BODIPY dyes* ***1-3****. (meso-BODIPY* ***1****:* R_1*=*CH_3*,* R_2*=H, meso-BODIPY* ***2****:* R_1*=* $C(CH_3)_3$*,* R_2*=H, meso-BODIPY* ***3****:* R_1*=H,* R_2*=* $C(CH_3)_3$*).*

AIMD simulations were performed by David Robinson in both the gas phase and solvated phase, using the PCM. All AIMD simulations were run for a total of 104 steps, with a time step of 10 a.u. Ground-state and excited-state potential energy surfaces were explored using the MOM method outlined above for the BODIPY core, with the aim to obtain absorption and emission energies for the three *meso*-BODIPY dyes.

3.3. Results & Discussion

3.3.1. BODIPY core and PM dyes

The structural parameters of BODIPY from ***Table 3.1.*** show that as expected, the ground state of BODIPY has C_{2V} symmetry, which is reflected in both the CASPT2 and B3LYP structures. The biggest deviation in bond length between CASPT2 and B3LYP is 0.014 Å for the N-C_1 bond, and the bond angles agree within 1º. These computed results agree well with the experimental values for the ground state, with the largest deviations in bond length being the B-N bond; the only major difference being that the X-ray structure is non-planar at the boron atom whereas the computed structures are found to be planar. It is likely this is due to the packing forces present in the crystal structure, which are not replicated in the gas–phase molecules being optimised.

For the S_1 state, all of the calculations find the rings to be non-planar in the optimised structures, in contrast to the ground state structures. A non-planar structure has also been reported in TDDFT calculations of the closely related PM597 laser dye, although the same study reports the excited state structures of the PM567 and PM580 as planar [93]. Similar calculations carried out for this study shown in ***Table 3.2.***, with SP-MOM as opposed to TDDFT, show that the PM567 and PM580 dyes are close to planar, with a deviation from planarity to 4.8º as opposed to 3.5º in the ground state for PM597. There was not found to be a significant decrease in the planarity for the MOM calculation of PM597.

The extent of planarity in the structures is indicated by the B-N-C_4-C_5 dihedral angle, which is found to be 14.4º at the CASPT2 level with smaller values in the DFT calculations for the BODIPY core.

Table 3.1. *Structural parameters for the S_0 and S_1 states of BODIPY computed at different levels of theory and taken from experiment; (a) from reference [166], (b) from reference [167].*

	S_0			*S_1*			
Parameter	CASPT2/ 6-31G*	B3LYP/ 6-311G**	Exp.	CASPT2 / 6-31G*	SM-B3LYP/ 6-311G**	SP-B3LYP/ 6-311G**	SM-B3LYP/ 6-31G
Bonds (Å)							
B-F	1.388	1.387	1.378[a]	1.390	1.388	1.388	1.430
B-N	1.561	1.572	1.545[a]	1.555	1.562	1.561	1.547
N-C_1	1.352	1.338	1.339[a]	1.343	1.344	1.332	1.357
C_1-C_2	1.406	1.411	1.400[a]	1.418	1.420	1.421	1.427
C_2-C_3	1.390	1.386	1.370[a]	1.406	1.385	1.397	1.395
C_3-C_4	1.425	1.418	1.410[a]	1.408	1.428	1.410	1.432
C_4-C_5	1.385	1.389	1.383[a]	1.418	1.411	1.416	1.413
C_4-N	1.389	1.393	1.391[a]	1.420	1.398	1.420	1.418
Angles (º)							
F-B-F	111.8	111.3	108.6[b]	112.2	111.0	111.2	109.0
N-B-N	104.9	105.5	106.6[b]	102.5	104.8	104.5	105.9
C_4-C_5-C_6	121.7	121.9	123.3[b]	118.4	119.4	119.7	119.5
N-C_4-C_5	121.3	120.6	118.9[b]	120.1	121.0	120.4	120.8
B-N-C_4-C_5	0.0	0.0	4.3	14.2	10.2	8.2	6.1

Table 3.2. *Structural parameters for the S_0 and S_1 states of PM567, PM580 and PM597 computed at B3LYP/6-311G** and SP-MOM for the S_1 state.*

Parameter	PM567		PM580		PM597	
	S_0	S_1	S_0	S_1	S_0	S_1
Bonds (Å)						
B-F	1.402	1.407	1.402	1.407	1.406	1.406
B-N	1.552	1.545	1.551	1.546	1.554	1.554
N-C1	1.344	1.355	1.344	1.355	1.344	1.344
C1-C2	1.416	1.424	1.416	1.424	1.430	1.430
C2-C3	1.396	1.396	1.397	1.396	1.406	1.406
C3-C4	1.434	1.441	1.433	1.440	1.435	1.435
C4-C5	1.406	1.426	1.406	1.423	1.408	1.408
C4-N	1.396	1.396	1.396	1.396	1.389	1.389
Angles (^{o})						
F-B-F	109.8	109.1	109.8	109.2	109.9	109.9
N-B-N	106.5	106.2	106.6	106.1	107.2	107.2
C4-C5-C6	120.7	118.1	120.8	118.0	120.7	120.7
N-C4-C5	120.4	121.0	120.3	121.1	120.4	120.4
B-N-C4-C5	1.4	1.539	0.1	0.3	4.8	4.8

Overall, for the excited state there is a small deviation between the structures predicted by CASPT2, SM-B3LYP and SP-B3LYP, with the SP-B3LYP structure slightly closer to the CASPT2 in terms of bond lengths and angles, though SM-B3LYP has the closest B-N-C_4-C_5 dihedral angle to the CASPT2 structure. It appears that SP-MOM

calculations may underestimate this deviation from planarity in the aromatic ring, which may explain the results previously discussed for the PM597 dye.

For the MD simulations it is necessary to reduce computational expense as much as possible, due to the fact every step in an AIMD simulation will take as much computational resources as one complete DFT SCF geometry optimisation cycle. For this reason, also shown in ***Table 3.1.*** is the structure for SM-B3LYP with the 6-31G basis set. While the reduction in the basis set leads to some larger deviations in the structure compared to CASPT2, particularly the B-F bond length and F-B-F bond angle, the structure of the ring system, where the electronic excitation is localised, is predicted quite accurately. Therefore 6-31G is thought to be an appropriate basis set for the MD simulations.

Excitation energies for singlet states using SM-B3LYP have been predicted to be too low, and this is evident in ***Table 3.3.*** as the SM-B3LYP values for the S_1 state of BODIPY are significantly lower than corresponding values from the CASPT2 calculations, as well as experimental values, although bulk and solvent effects have not been taken into account with these quantum chemical calculations, which may bring the results closer to the experimental values. The three PM dyes also show significantly lower SM-B3LYP values for the S_1 state when compare to the experimental data. Once the spin-purification is applied, the error is partially corrected, for both BODIPY and the three PM dyes, with the SP-B3LYP values being closer to the CASPT2 and experimental values, though are still around 0.3 eV lower than CASPT2 for BODIPY. The SP-B3LYP absorption values for BODIPY are very close to experiment, being 0.05 eV and 0.1 eV too low for the SP-B3LYP and $^{\#}$SP-B3LYP methods respectively, where $^{\#}$SP-B3LYP corresponds to a spin-pure MOM energy from a structure optimised at

Table 3.3. *Computed transition energies for BODIPY at a variety of different levels of theory.*

Molecule	Method	E_{abs}/eV	0-0/eV	E_{em}/eV
BODIPY	CASPT2/6-31G*	2.62	2.58	2.37
	SM-B3LYP/6-311G**	2.06	2.01	1.97
	SP-B3LYP/6-311G**	**2.41**	**2.33**	**2.23**
	[#]SP-B3LYP/6-311G**	**2.36**	**2.35**	**2.26**
	[†]TD-B3LYP/6-311G**	3.15	-	1.43
	Experimental	**2.46**	**-**	**2.41**
PM567	SM-B3LYP/6-311G**	1.94	-	1.96
	SP-B3LYP/6-311G**	**2.25**	**-**	**2.18**
	[#]SP-B3LYP/6-311G**	**2.22**	**-**	**2.12**
	[†]TD-B3LYP/6-311G**	2.89	-	-
	Experimental	**2.40**	**-**	**2.32**
PM580	SM-B3LYP/6-311G**	1.93	-	1.95
	SP-B3LYP/6-311G**	**2.24**	**-**	**2.17**
	[#]SP-B3LYP/6-311G**	**2.23**	**-**	**2.12**
	[†]TD-B3LYP/6-311G**	2.88	-	-
	Experimental	**2.39**	**-**	**2.31**
PM597	SM-B3LYP/6-311G**	1.90	-	1.93
	SP-B3LYP/6-311G**	**2.22**	**-**	**2.16**
	[#]SP-B3LYP/6-311G**	**2.19**	**-**	**2.01**
	[†]TD-B3LYP/6-311G**	2.84	-	-
	Experimental	**2.37**	**-**	**2.20**

SM-B3LYP/6-31G, and are slightly further away from experiment for the PM dyes, with transitions being consistently 0.1-0.2 eV lower than experiment. The emission values for SP-B3LYP shows a similar deviation from experiment for all four molecules.

There is little change in the calculated SP-B3LYP/6-311G** excitation energies when the structure was optimised at the SM-B3LYP/6-31G level ($^{\#}$SP-B3LYP/6-311G**), with the maximum change evident in the absorption energy of 0.05 eV for BODIPY, as well as a change of 0.15 eV for the PM597 emission energy. This is because the transition being studied involves orbitals localised on the rings, and the structure of the rings have been shown in ***Table 3.1.*** to be reproduced accurately using the smaller 6-31G basis set. This suggests using this smaller basis set for the AIMD and QM/MM calculations will only introduce a small error, while reducing the computational time by a significant amount. Vertical absorption and emission energies with TDDFT (†TD-B3LYP/6-311G**) are further from the CASPT2 values, with the absorption and emission energies too high and too low, respectively. TDDFT excitation energies have also been found to be too high in calculations on PM567 [142].

The calculated absorption energies in ***Table 3.3.*** for the PM dyes are within 0.2 eV of experiment, and do show a slightly lower absorption energy for PM597 which is evident in experiment. Some difference with the experimental values would be expected because calculated gas-phase values are compared with experimental measurements in the solvent phase. A similar level of agreement with experiment is found for the emission energies. A Stokes shift of about 0.1 eV is found for BODIPY, which agrees well with the experimental shift of 0.05 eV [166]. A Stokes shift of 0.1 eV is also calculated for PM567 and PM580 with a Stokes shift of 0.2 eV for PM597, which agrees with the larger Stokes shift for PM597 in experiment. Overall, the results suggest that the SP-B3LYP/6-311G**//B3LYP/6-31G approach provides a relatively inexpensive

but accurate description of the lowest absorption and emission transitions in BODIPY and related molecules that can be applied in QM/MM simulations.

Table 3.4. *Average values of the structural parameters of the S_0 and S_1 states from the molecular dynamics simulations.*

	Gas Phase		Water Solvent	
Parameter	S_0	S_1	S_0	S_1
Bonds (Å)				
B-F	1.426	1.439	1.481	1.479
B-N	1.576	1.562	1.516	1.511
N-C1	1.360	1.370	1.373	1.376
C1-C2	1.419	1.428	1.405	1.419
C2-C3	1.396	1.397	1.410	1.401
C3-C4	1.427	1.434	1.417	1.430
C4-C5	1.397	1.407	1.397	1.411
C4-N	1.413	1.418	1.423	1.432
Angles (°)				
F-B-F	110.8	110.5	102.4	101.7
N-B-N	105.3	105.0	109.0	109.2
C4-C5-C6	122.1	120.3	120.5	119.3
N-C4-C5	120.4	120.8	120.4	120.7
B-N-C4-C5	6.2	9.5	7.6	7.0

The gas-phase simulations using the SP-B3LYP/6-311G**//B3LYP/6-31G approach gives structures in ***Table 3.4.*** which agree well with the structural parameters from ***Table 3.1.*** Some differences are evident between the gas and solvent-phase simulations, which are mostly focussed on the B-F groups, where there is a large increase in B-F bond lengths and decrease in B-N bond lengths in the condensed phase, which also causes corresponding changes in bond angles, with smaller F-B-F and larger N-B-N angles in the condensed phase.

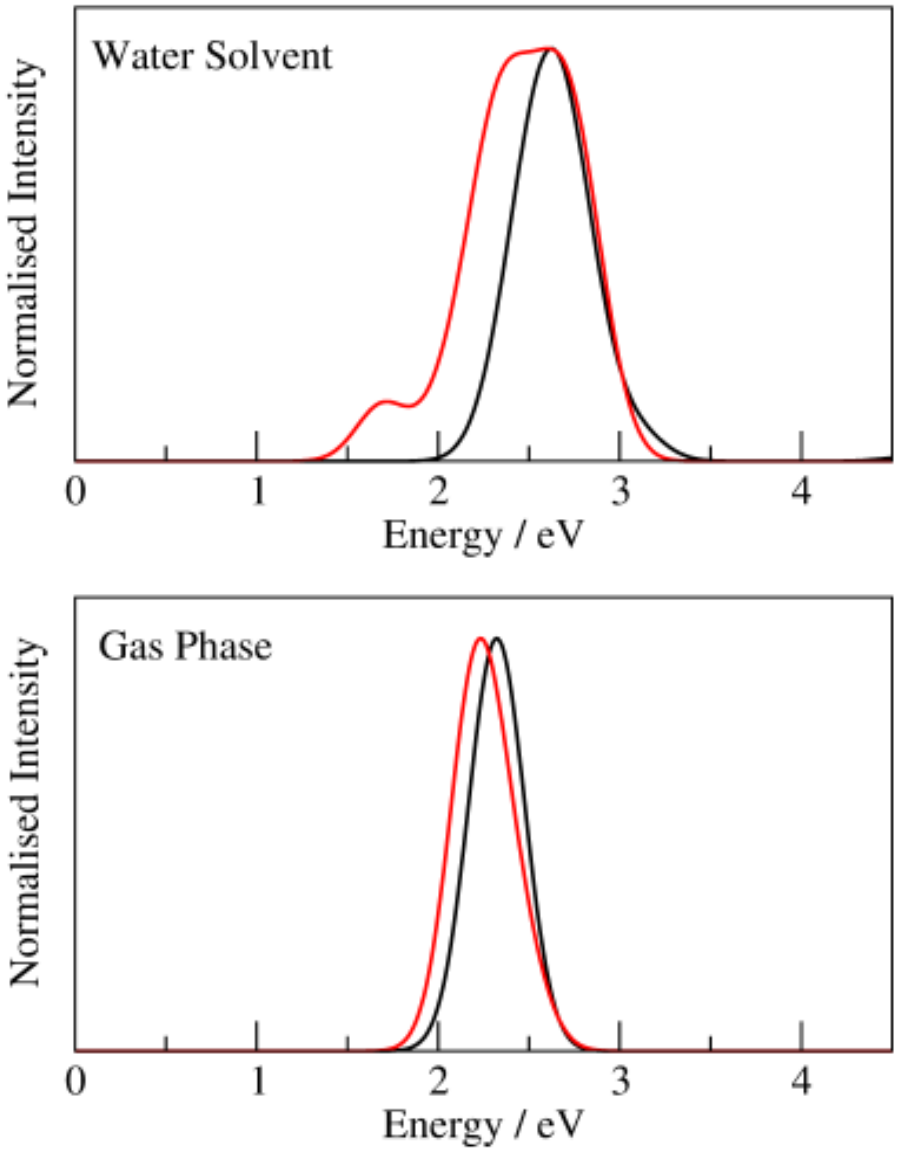

Figure 3.5. *Simulated absorption (black line) and emission (red lines) bands for the lowest energy transition of BODIPY in gas-phase and water.*

The absorption band for the gas phase simulations in ***Figure 3.5.*** (black line) has its maximum at 2.32 eV and the emission maximum (red line) at 2.23 eV giving a Stokes shift of 0.09eV. These compare well with experimentally obtained absorption and emission maxima in ethanol solvent; 2.49 eV and 2.32 eV, respectively [166]. The emission band is wider than the absorption band, which can be shown by the standard deviation of 0.06 eV for absorption and 0.10 eV for emission energy. This also compares well with experimental data for BODIPY [77]. Overall there are only small structural differences between the S_0 and S_1 states. ***Table 3.4.*** shows a small decrease in B-N bond length and a small increase in other bond lengths of the ring and the non-planarity of the ring (B-N-C_4-C_5 dihedral angle). The average dipole moment of the ground state is calculated to be 4.6 D, while the dipole moment of the excited state is found to be lower at 3.8 D. A lower value for the dipole moment in the S_1 state is consistent with calculations on PM567 [142]. The emission spectrum for the solvated BODIPY exhibits a shoulder maximum at 1.4 eV, at much lower intensity than the main emission band. This is most likely due to the QM/MM simulation giving rise to some structures a second stable state of excited BODIPY, which would be possible with the higher energy emission structure under influence of solvent.

The radial distribution functions for the S_0 and S_1 state from ***Figure 3.6.*** are similar to each other with the first solvent shell at about 3.6 Å, with a second solvent shell at about double the distance of the first shell at 6.4 Å. This second shell is less ordered than the first, as the peak observed at the second solvent shell is not as distinct as for the first solvent shell. The solvent simulations predict an absorption band with a maximum at 2.62 eV and an emission band centred at 2.53 eV. Both bands show a Stokes shift of around 0.3 eV, which is much larger than the values from the gas phase. This is

consistent with the dipole moment of the excited state being smaller than the ground state, which would lead to a blueshift in the transition energies in a polar solvent.

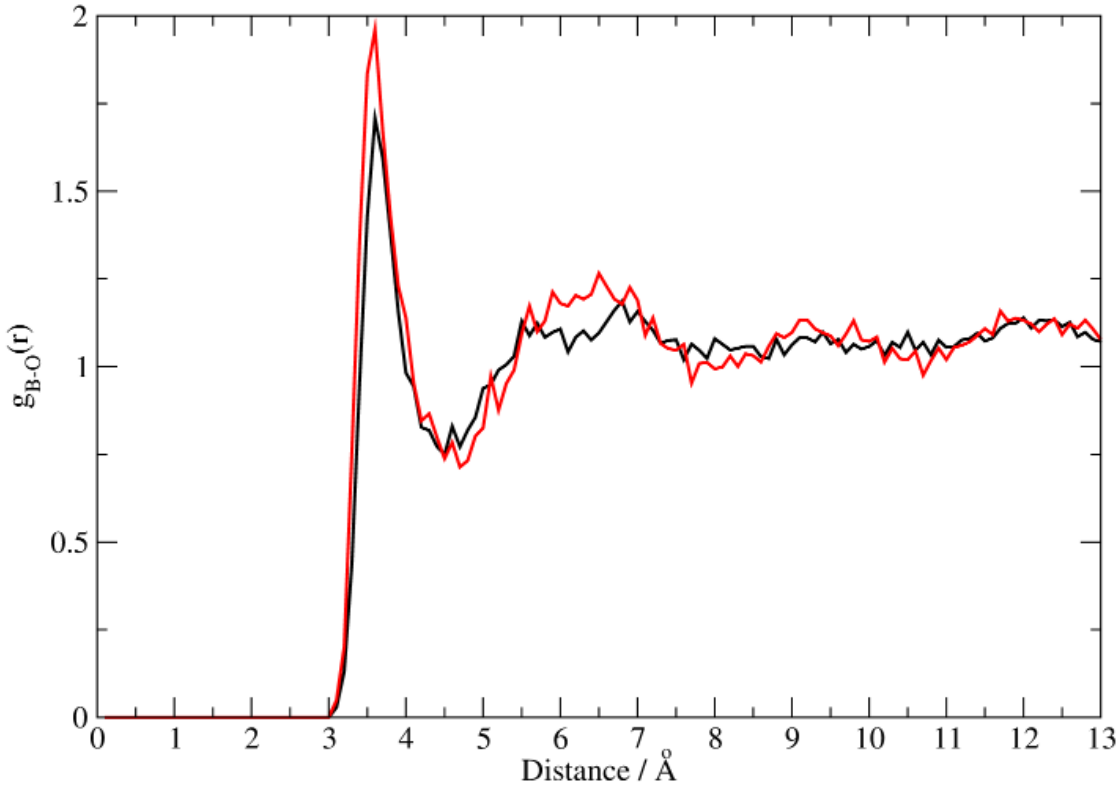

Figure 3.6. *Radial distribution functions of the BODIPY boron to water oxygen distance for the ground state (black line) and excited state (red line).*

Furthermore, the computed gas-phase absorption and emission energies for the PM laser dyes (***Table 3.3.***) were lower than the experimental values measured in methanol. Based on the results for water, a blueshift in the transition energies is also expected for these closely related molecules in methanol, which would bring the computed values in close agreement with experiment. Absorption and emission spectra for BODIPY based dyes have been reported for a range of solvents [136]. These spectra also show a small shift towards higher absorption and emission energies in more polar solvents. The emission bands are also found to be wider than the absorption bands, with experimental spectra showing a full width at half maximum for the absorption and emission bands of approximately 1.5 for a BODIPY based dye in methanol [136] and 1.7 for PM546 in

methanol [165]. For the simulated bands in water solvent the ratio of emission: absorption is 1.5, which is consistent with the experimental values. However, the actual widths of the bands are larger than observed in experiment. This is likely to be associated with treating the water molecules that are very close to BODIPY as point charges in the DFT calculations to determine the transition energies, and not treating them explicitly with DFT. This could be addressed by treating these water molecules fully within the DFT calculations.

3.3.2. *Meso*-BODIPY

In this work, the structures and emission energies of *meso*-BODIPY **1**–**3** were calculated at 0K both in the gas phase and in dichloromethane using DFT with a PCM representing the solvent using the B3LYP/6-311G* level of theory. For compounds **1**, **2** and **3**, the calculated λ_{em}(max) were 532 nm, 620 nm and 539 nm, respectively, from the S_0 and S_1 minimum energy geometries. These values are redshifted with respect to the experimental ones by over 0.12 eV for **1** and **3** and 0.25 for **2**. Given in ***Table 3.5.*** are some of the computed geometrical parameters for both the S_0 and S_1 states. In the S_0 state, all three BODIPY derivatives show a very small dihedral angle between the two pyrrole rings, with **3** displaying a highly planar conformation of the BODIPY core.

Table 3.5. *Structural parameters for the S_0 and S_1 states of BODIPYs **1, 2** and **3** in gas and solvent phases, using B3LYP/6-311G* DFT, with SP-MOM for the S_1 states.*

	meso-BODIPY **1**		*meso*-BODIPY **2**		*meso*-BODIPY **3**	
Parameter	S_0	S_1	S_0	S_1	S_0	S_1
Gas Phase						
B-N (Å)	1.561	1.558	1.549	1.556	1.577, 1.561	1.559, 1.577
C5-C9 (Å)	1.505	1.500	1.551	1.534	-	-
B-N-C4-C5 (°)	4	4	4	27	0	0
Solvent Phase						
B-N (Å)	1.551	1.545	1.537	1.543	1.567, 1.590	1.559, 1.577
C5-C9 (Å)	1.502	1.500	1.550	1.535	-	-
B-N-C4-C5 (°)	4	4	4	25	0	0

These data are in excellent agreement with experimental X-ray crystal data, *Meso*-BODIPY **2** shows a distorted, nonplanar geometry in the S_1 state, characterised by a very large dihedral angle of 27° in the gas phase and 25° in dichloromethane, compared to much smaller angles for **1** and **3** (4° and 0°, respectively). This is thought to give rise to a destabilised ground-state electronic structure of **2** at the S_1 geometry (0.20 eV relative to the ground state minimum), whereas **1** and **3** show much smaller destabilisation of the ground-state electronic structure at their respective S_1 geometries (0.05 eV and 0.03 eV for compounds **1** and **3**, respectively), which leads to the redshifted emission maximum of **2** relative to **1** and **3**. This can account for the large Stokes shift and broad emission band of **2**.

3.4. Conclusions

The structure of the BODIPY core fluorophore, along with three pyrromethene laser dyes and three *meso*-substituted BODIPY derivatives were compared with each other and experimental results. The optimised S_1 structure was found to be non-planar using CASPT2 and DFT methods, which has interesting implications to the activity of the S_1 state. Dynamics and absorption and emission spectra have been simulated for the S_0 and S_1 states of BODIPY in both the gas phase and water. The excited states have been calculated using Kohn-Sham DFT, using the MOM procedure to converge SCF calculations to give excited states. To give accurate transition energies, a post-SCF spin-purification correction has been successfully applied to give more accurate transition energies. It has been found that absorption and emission energies can be accurately computed using structures optimised using DFT with a relatively small basis set and then evaluating the absorption and emission energies using a larger basis set. Molecular dynamics simulations have been performed on both the ground and excited states, and for the condensed phase water is incorporated within a QM/MM framework. The resulting spectra are consistent with available experimental data, with a predicted Stokes shift of about 0.1 eV, and a blueshift of about 0.3 eV in water compared to gas-phase. The simulations also show the width of the emission band in solution to be broader than the absorption band by the same amount as that reported in experimental spectra of a closely related molecule. Overall a relatively cheap method employing a small basis set has been employed to simulate the absorption and emission spectra of BODIPY, with good agreement with experimental data.

There is still a large amount of work which could be carried out in this area. Further investigation into the non-planarity of the S_1 state, could show whether there are exceptions to the deviation of planarity in the S_1 state, or how it arises and affects the

properties of the molecules. Looking closer at the simulation work could involve modeling the first solvent shell of water around BODIPY with explicit DFT as opposed to point charges, with the aim to obtain absorption and emission spectra that may be more accurate than modeling the entire water solvent as point charges. Also it is possible to do dynamics simulations and subsequent excitations with small laser dyes, such as PM567, although this results in a large increase in computational time due to the time-scaling factors of DFT. Since the initial run of these calculations the ability for high performance computers to produce longer simulations with larger BODIPY dyes is a real possibility which could yield worthwhile results.

The work with *meso*-substituted BODIPY shows that the deviation from planarity seen with the BODIPY fluorophore and PM dyes can be extended to other BODIPY derivatives, and the amount of or lack of planarity can be changed by varying the substituents. It was found a more bulky alkyl substituent on the *meso* position leads to a larger deviation from planarity in the excited state, and the exited state structure can be used to rationalise observed spectroscopic properties.

Overall this study has made two main advances in the research of BODIPY dyes and similar fluorophores: the first being that a combined AIMD/DFT approach with QM/MM solvent gives an accurate model of how these fluorophores behave; the second being that an unexpected deviation from planarity in the calculations is also observed in experimental data, which could have implications into how the molecules work and behave in the S_1 excited state.

4. Density Functional Theory Based Analysis of Photoinduced Electron Transfer in a Triazacryptand Based K^+ Sensor

4.1. Introduction

Ions play an important role in many biological processes. The potassium cation (K^+) is the most abundant intracellular ion in the human body and is involved in processes which include muscle contractions, nerve transmission, and kidney function [168-170]. Potassium cations are essential for these processes to properly function. Furthermore, K^+ deficiency can be a sign of poor health and an indicator of many conditions and diseases, such as a weakened heartbeat or a sign of deficiencies in the body resulting from eating disorders [171-173]. Although the potassium cation plays a major role in the health of humans and animals, the mechanisms of K^+ in the body are still poorly understood. It is important to be able to reliably determine the concentration of ions such as K^+ in cells in order to determine their mechanisms in extracellular and intracellular processes, and many current methods exist. One analytical technique, the K^+ electrode [174], produces reliable data but cannot be applied non-invasively into biological systems, and operates on too large a scale to be applied to single-cell areas of an organism. Fluorescence based sensors provide one approach to overcoming the problems of the K^+ electrode method, as it is non-invasive and can be applied to small (single cell) systems. Research into designing and synthesising these fluorescent probes is a highly active area.

Modern day ion sensors typically comprise two key parts, a chelator which binds to the cation of choice and a fluorescent moiety, where the chelator selectively "traps" the ion of interest resulting in a significant enhancement or quenching of the fluorescence of the fluorophore component of the probe [175, 176]. Among the most commonly used and most well-known fluorescent sensors for intracellular K^+ is the potassium-binding benzofuran isophthalate (PBFI), which uses a diaz-18-crown-6 to bind the ion and an isophthalate substituted benzofuran as the fluorophore. It has been shown to be highly fluorescent in the presence of K^+ ions [177]. One main drawback to using PBFI and the closely related sodium sensor SBFI is their poor selectivity between sodium ions (Na^+) and potassium [178]. These selectivity issues can be improved by using a ligand based on the triazacryptand platform, first developed by He et al. which features excellent selective responses for K^+ over competing Na^+ at physiological concentrations [179]. Selectivity of K^+ over Na^+ is important for a potassium sensor as they have similar properties due to their electronic structure and charge, so bind in a similar fashion.

Several recent examples of fluorescent chemosensors for ions have been reported [176, 119, 180]; many of these are based upon the BODIPY chromophore [111, 119, 181], which has also been a topic of interest in this thesis. A similar fluorescent chromophore is the aminonaphthalimide fluorophore (see ***Figure 4.1.***), which has been used in the synthesis of a triazacryptand-based fluorescent sensor with a 4-aminonaphthalimide fluorophore reported by Zhou et al. [2], as shown in ***Figure 4.2.*** This probe is weakly fluorescent with no metal chelated, but in the presence of K^+ it becomes strongly fluorescent, and is highly selective with very low levels of emission recorded for different metal cations.

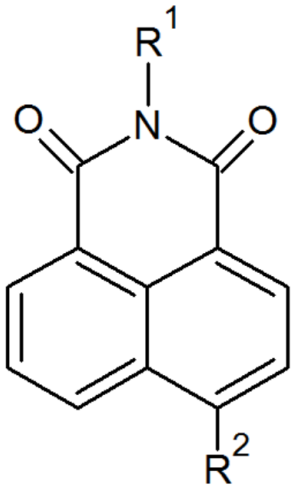

Figure 4.1. *General structure of a 4-amino-1-naphthalimide fluorophore.*

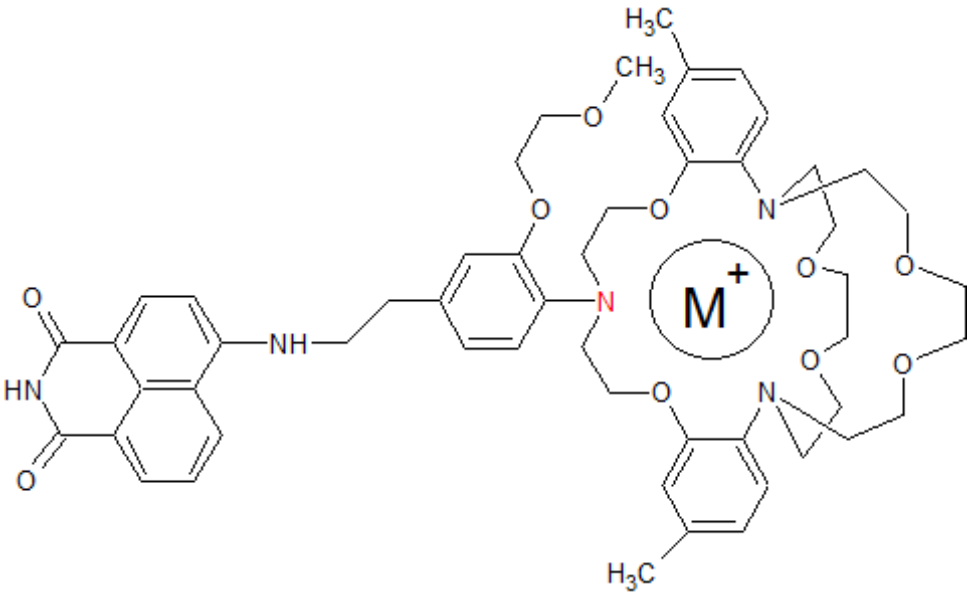

Figure 4.2. *Structure of triazacryptand sensor KS1.*

There are many photophysical processes that can lead to the quenching or enhancement of fluorescence. For the KS1 sensor, the change in fluorescence has been attributed to a reductive photoinduced electron transfer (PET) mechanism [2]. This process can be described in Eq. (4.1) [176], where $^1A^*$ represents the electronically excited 4-aminonaphthalimide fluorophore and D represents the electron donating triazacryptand system and is illustrated schematically in ***Figure 4.3.***

$$^1A^* + D \rightarrow {}^1A^{\bullet-} + D^{\bullet+} \quad (4.1)$$

$$^1D^* + A \rightarrow {}^1D^{\bullet+} + A^{\bullet-} \quad (4.2)$$

It is suggested in the absence of K^+, this PET process occurs in the KS1 sensor, resulting in fluorescence quenching and the system returning to its ground state via a nonluminescent process. However, in the presence of K^+, the chelator is no longer able to donate electrons to the chromophore and the PET process does not occur, which results in a strong fluorescence. Oxidative PET is a related process and corresponds to where the excited electron of the fluorophore can be transferred to a low lying unoccupied orbital of the chelator (Eq. 4.2).

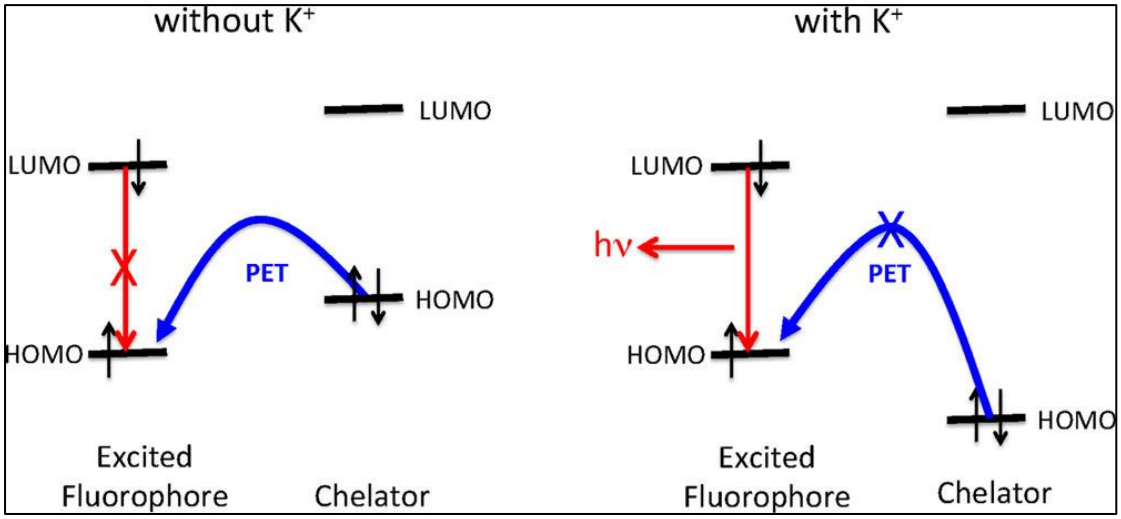

Figure 4.3. *Schematic representation of the photoinduced electron transfer process proposed for the KS1 sensor.*

The design and development of chemical sensors is challenging partly due to the complexity of the underlying photophysical processes in such large photosensitive molecules. Quantum chemical calculations have a potentially valuable role to play in this area since they can provide a detailed picture of the electronic structure of the fluorescent probe molecules, giving insight into the relevant photophysical processes

that in turn can aid the design of new sensors. The large size of the molecules involved precludes the use of accurate wave function based excited state methods such as multireference configuration interaction (MR-CI) [182] and multiconfigurational perturbation theory [183], and density functional theory based approaches represent the most accurate alternative. A number of groups have studied PET in fluorescent probes using KS-DFT and TDDFT [161, 176, 184-186]. The most common approach is to construct a molecular orbital diagram for the frontier molecular orbitals based upon the Kohn−Sham orbitals and their associated energies to determine whether PET and the associated fluorescence quenching or enhancement should occur [161, 184, 185]. This can often provide a picture that is consistent with the experimental observations and can be used to rationalise the observed fluorescent properties of a chemical sensor.

In an analysis of this type, the difference in orbital energies is implicitly being used as a measure of the relative energies of the excited states associated with the various stages of the PET process. One main problem with this approach is that orbital energy differences often provide a poor measure of the energies of the respective excited states, and to determine these reliably it is necessary to use a genuine excited state electronic structure method, such as TDDFT. Recent work has used TDDFT calculations to analyse the fluorescence quenching by Hg(II) ion chelation and fluorescence enhancement by Zn(II) ion chelation in a PET sensor [186]. However, the application of TDDFT to study these systems is not without its pitfalls, since many of the states involved will be charge transfer in nature, which represents a case where TDDFT with standard GGA or hybrid exchange-correlation functionals is known to fail [44]. This study has investigated the role of PET in the fluorescent activity of the KS1 sensor 1 using DFT, TDDFT, and excited state KS-DFT (using MOM). Two main approaches are used. Firstly, absolute molecular orbital energies are considered to rationalise the

presence or absence of PET in KS1. Secondly, excited state calculations are considered to assess the relative energies of different excited states of the structures, and how this can affect PET occurring in the structures. It is shown that different approaches can lead to different conclusions, with in some cases the correct behaviour predicted for the wrong reason. We find that to account for PET in KS1 correctly, it is necessary to use an appropriate excited state electronic structure method and include the influence of solvent.

4.2. Computational Details

The structure of KS1 in the ground state was optimised with and without the K^+ ion as well as with the Na^+ cation using DFT with the B97-1 exchange correlation functional [29] and the 6-31G* basis set [187, 188]. ***Figure 4.2.*** shows the molecular structure of the sensor used in the calculations. In experiment, the sensor has an extended chain attached to the nitrogen atom of the fluorophore that is not well-defined. This part of the structure plays no role in the function of the sensor, therefore in this study the chain has been replaced by a single hydrogen atom. In order to find the orbitals involved in transition to the first excited singlet state, time-dependent density functional theory was applied to the optimised structures using a range of different functionals with the 6-31G* basis set to find the lowest allowed singlet excitation energy for each functional, and the orbitals involved in that excitation, as well as viewing the symmetry of orbitals to confirm the π and π^* nature of the transition orbitals. Excited state energies were determined using TDDFT with the B3LYP and B97-1 functionals [28, 189] as well as the long-range corrected CAM-B3LYP and ω-B97 functionals [31, 32], known for their improved accuracy compared to standard hybrid functionals when calculating charge-transfer states [44]. Excited singlet state energies were also determined in a ΔSCF (or Δ Kohn−Sham) approach using KS-DFT where an initial set of orbitals are generated for each structure using the orbitals for the ground state. An electron is moved from one orbital to another, using the orbitals identified from the TDDFT excitation. The MOM [45] is then used to prevent variational collapse to the ground state for subsequent SCF calculations and to obtain ΔSCF energies. MOM has previously been used successfully to model the excited states of a range of systems [47, 48, 190], including BODIPY. One issue with this approach is that open-shell singlet states are not described well by a single determinant leading to a significant underestimation of the energy of some singlet

excited states [191]. However, the spin-purification procedure [49] can be applied as previously described. The ΔSCF procedure outlined was applied to the metallated and non-bound KS1 structures for the functionals described where possible, in both gas phase and solvent. The structure of the excited states were also optimised using the MOM approach. Emission energies for the sensor were obtained from these optimised excited states using the energy of the lowest $\pi \rightarrow \pi^*$ transition of the fluorophore. Solvent was modelled using a PCM with parameters corresponding to water, with a dielectric constant of ε=78.39. All calculations were performed using the Q-Chem software package [192].

4.3. Results & Discussion

4.3.1. Computed Transition Energies

It is important to assess from quantum chemical calculations the orbitals involved in absorption, emission and photoinduced electron transfer processes in the KS1 sensor. ***Figures 4.4.*** and ***4.5.*** show the lowest unoccupied and highest occupied orbitals as given by the B97-1/6-31G* calculation for the KS1 sensor with and without the K^+ ion.

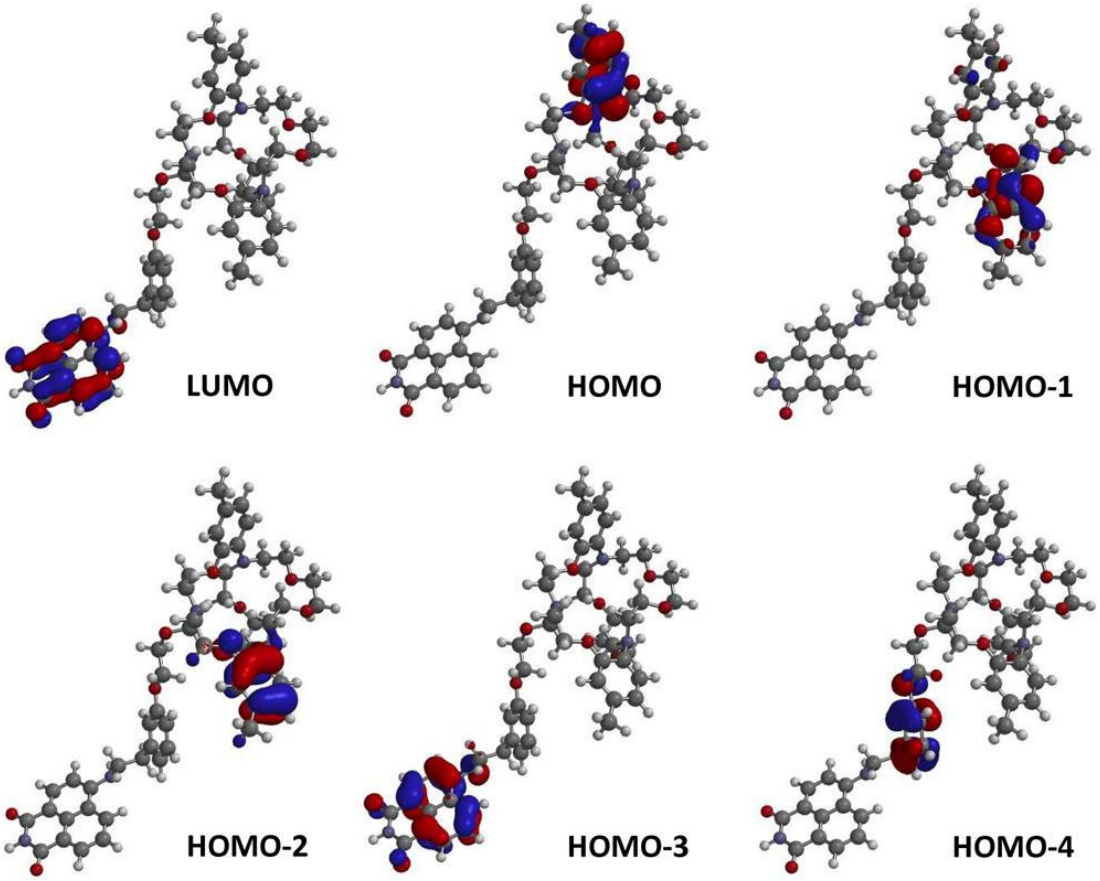

Figure 4.4. *Molecular orbitals of the K^+ sensor without K^+.*

Without K^+, the lowest unoccupied molecular orbital (LUMO) of KS1 is a π* orbital located on the 1,4-aminonapthalimide fluorophore part of the molecule. The three highest occupied molecular orbitals (HOMO, HOMO-1 and HOMO-2 orbitals) are localised on the triazacryptand chelator, while the highest occupied orbital associated

with the fluorophore is the HOMO-3 orbital, which can be described as a π orbital. The intense band observed in the absorption spectrum by Zhou et al. is localised on the fluorophore and arises from the HOMO-3→LUMO transition, which has π→π* symmetry. With the inclusion of K^+, the intense transition localised on the fluorophore corresponds to excitation from the HOMO→LUMO+1. The electron density in the LUMO is localised on the potassium cation, and the other high lying occupied orbitals are localised on the fluorophore or the linking group between the fluorophore and chelating moiety.

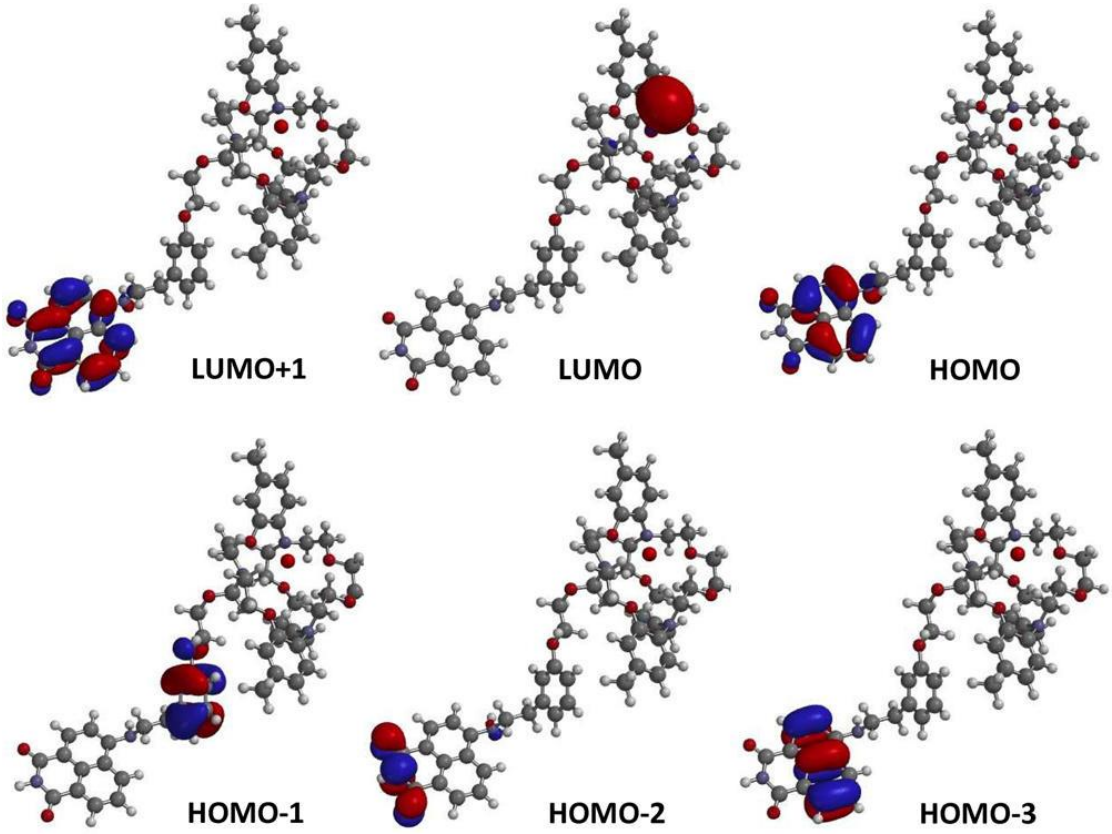

Figure 4.5. *Molecular orbitals of the K^+ sensor with K^+.*

Table 4.1. shows the computed transition energies of the intense fluorophore transition using various DFT based approximations. The calculated gas-phase transition energies are higher than the experimental value of 2.76 eV for the non metallated and K^+ structures [2]. Taking the difference in the relevant orbital energies (Δε) gives a value

of 3.76 eV for the non-chelated sensor, 1 eV higher than experiment. This is improved by TDDFT, which gives values of 3.36 eV for the B97-1 functional and a similar value of 3.34 eV for B3LYP. The long-range corrected functionals CAM-B3LYP and ω-B97 predict transition energies that are about 0.4 eV and 0.7 eV higher in energy respectively than those for the standard hybrid functional and close to the Δε value. It was clear from the results in ***Table 4.1.*** that the ω-B97 functional consistently predicted transition energies that were too large for all 3 structures being studied, and therefore was not used for the ΔSCF calculations. The B3LYP functional was also not used beyond this point in the study, as it showed for all structures to have transition energies 0.02 eV lower than the B97-1 functional. Due to the rise in use of B97-1 over recent years and its reliability of results including those previously undertaken by the author, this was favoured over B3LYP [29].

For the ΔSCF calculations, the initial orbitals were generated from the ground state orbitals where a β spin electron is moved from the HOMO-3 orbital to the LUMO for the non-chelated sensor. Results are given for the spin-mixed determinant, denoted ΔSCF^{SM}, and if post-SCF spin purification has been applied, denoted ΔSCF^{SP}. Both of these approaches give a lower transition energy that are closer to experiment. The spin-mixed approach gives 2.82 eV; however this is artificially too low, and spin purification gives a value of 3.20 eV, which is close to the TDDFT result. The value for spin-mixed ΔSCF using CAM-B3LYP in the gas phase shows a similar result to the spin-pure value for B97-1, however the spin-pure value is already known to give artificially low results, and with this excitation energy nearly 0.5 eV higher than experiment, it can be assumed spin-pure and solvated calculations using CAM-B3LYP functional would not give accurate results with respect to experiment for the sensor.

Table 4.1. *Computed transition energies for the intense transition localised on the fluorophore with and without the K^+ ion for a range of computational methods.*

Method	$\Delta E_{noK^+}^{F\rightarrow F}$ (eV)	$\Delta E_{K^+}^{F\rightarrow F}$ (eV)	$\Delta E_{Na^+}^{F\rightarrow F}$ (eV)
Δε	3.76	3.83	-
TD-B3LYP	3.34	3.45	3.40
TD-B97-1	3.36	3.47	3.42
TD-CAM-B3LYP	3.76	3.86	3.81
TD- ω-B97	4.03	4.16	4.08
ΔSCF^{SM}-B3LYP	2.82	2.91	2.86
ΔSCF^{SM}-B97-1	2.82	2.94	2.90
ΔSCF^{SM}- CAM-B3LYP	3.22	3.34	3.28
ΔSCF^{SP}-B97-1	3.20	3.36	-
ΔSCF^{SM}(sol)-B97-1	2.71	2.79	-
ΔSCF^{SP}(sol)-B97-1	3.02	3.12	-
expt	2.76	2.76	2.76

Table 4.2. shows the variation of the computed absorption energy with improving the quality of the basis set for the sensor with no K^+ bound, to assess how important the size of basis set is to the accuracy of results. These results indicate that changing from a double to triple-ζ type basis set leads to changes in the computed excitation energies of up to 0.05eV. The addition of diffuse basis functions gives a greater variation with changes in the computed excitation energies of up to 0.1eV. Consequently, the transition energies predicted with 6-31G* should be converged with respect to the basis set quality

to the order of about 0.1 eV. There is sufficient variety among results from different functionals and methods of excitation to assume that expanding the basis set from 6-31G* for all calculations will not have a significant effect on the energies calculated, and will not affect the conclusions the numbers will lead towards.

Table 4.2. *Variation in the Computed Transition Energies for the Intense Transition localised on the Fluorophore without K^+ Ion Bound ($\Delta E_{noK^+}^{F\rightarrow F}$ in eV).*

Method	6-31G*	6-311G*	6-31+G*
Δε	3.76	3.76	3.70
TD-B97-1	3.36	3.33	3.42
TD-CAM-B3LYP	3.76	3.71	3.84
ΔSCF^{SM}-B97-1	2.82	2.86	2.80
ΔSCF^{SP}-B97-1	3.20	3.23	3.17

The experimental value is measured in solution, and the presence of solvent can influence the position of the absorption band for KS1. The dipole moment for the ground state (μ_{gs}) is 7.58D as given by DFT with the B97-1 functional, and this increases to 9.01D in the excited state arising from the fluorophore π→π* excitation. Consequently, a shift to a lower energy would be expected in a polar solvent, and using an implicit solvent model for water shows a shift to lower energy of about 0.1 eV for both the spin-pure and spin-mixed ΔSCF values for B97-1. The best calculation observed with respect to the experimental values, ΔSCF^{SP}(sol)-B97-1, predicts a value of 3.02 eV, which lies within 0.3 eV of the experimental value. Once the sensor is bound to K^+, there is only a modest effect on the fluorescent part of the molecule and only a

small change in the excitation energy of the fluorophore. The different methods consistently predict a small increase of about 0.1 eV when K^+ is present, and a smaller difference of around 0.05 eV with Na^+ bound to the sensor. This is consistent with experimental data, which shows no significant change in the absorption spectra with and without the presence of K^+. Optimisation of the excited state structure allows the emission energy to be calculated. The calculations give values of 2.48 and 2.24 eV for the ΔSCF^{SM}-B97-1 and ΔSCF^{SM}(sol)-B97-1 methods, respectively, which compare well with the experimental emission value of 2.41 eV.

4.3.2. Analysis of PET Based upon the Molecular Orbital Diagram

Figure 4.6. shows a schematic orbital energy diagram based upon the Kohn−Sham orbital energies for the B97-1/6-31G* calculation for the ground electronic state of the KS1 sensor, with and without solvent present, where the orbitals have been partitioned according to whether they are localised on the fluorophore or on the chelator, and the orbital occupancies depicted correspond to after the excitation of the fluorophore. When no K^+ is present there are three occupied chelator orbitals at energies between the singly occupied orbital in the fluorophore $\pi \rightarrow \pi^*$ state that can facilitate electron transfer to the fluorophore, which is consistent with a reductive PET process occurring. In contrast, when K^+ is bound to the chelating part of the sensor, there are no occupied chelator orbitals present between the HOMO and LUMO of the fluorophore, suggesting that a reductive PET process will not occur. This is consistent with the enhancement of the fluorescence of the sensor when the potassium cation is chelated. However, there is an unoccupied chelator orbital that lies just below the LUMO of the fluorophore, which opens up the possibility of an oxidative PET process occurring, which could also cause fluorescent quenching. Consequently, an analysis based upon the molecular orbitals would predict a reductive PET process in the absence of K^+ and an oxidative PET process in the presence of K^+. This would result in the sensor not fluorescing whether or not K^+ was present, which is not consistent with experimental results. Consideration of the molecular orbitals from the CAM-B3LYP calculations lead to a similar conclusion, with oxidative PET occurring without K^+ and reductive PET with K^+ chelated. Also shown in ***Figure 4.6.*** are the molecular orbitals from the calculations with implicit solvent. For the sensor without K^+, the molecular orbital diagram is qualitatively similar to the gas-phase, although some fluorophore and chelator relative energies differ slightly. For the case where K^+ is present, occupied orbitals associated

with the chelating part of the molecule are present between the HOMO and LUMO of the fluorophore and reductive PET remains a possibility. As the solvated model is a more accurate representation of the conditions of the experimental results, this further implies that looking at orbital energies alone, while accounting for the lack of fluorescence in the non-chelated sensor, this does not explain the strong fluorescence in the chelated sensor.

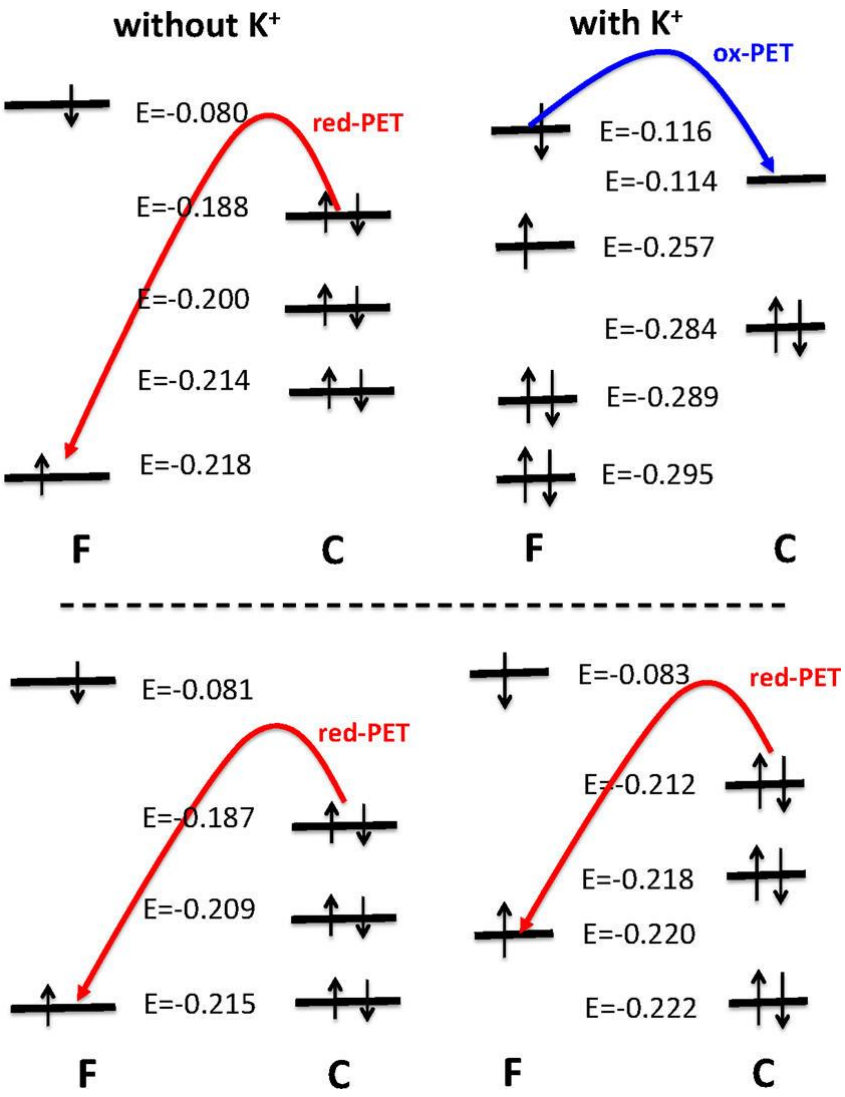

Figure 4.6. *Molecular orbital diagram based upon the ground state B97-1/6-31G* calculation for the gas phase (upper panel) and in solution (lower panel). F represents orbitals localised on the fluorophore and C represents orbitals localised on the chelating part of the molecule; orbital energies are given in a.u.*

4.3.3. Analysis of PET Based upon Excited State Calculations

Upon the basis of the above analysis, we conclude that a simple consideration of the molecular orbitals and their energies is not sufficient to reliably predict whether a PET process will occur and it is necessary to consider the relative energies of the initial and final electronic states. For a PET process to occur, the energy of the resulting electronic state formed from the PET process should be lower than the energy of the excited state formed by excitation of the fluorophore. For the K^+ sensor considered here, the final state corresponds to a CT state where the electron from the HOMO of the fluorophore has been excited to a virtual orbital associated with the chelating part of the molecule.

Table 4.3. *Computed transition energies for the lowest energy fluorophore → chelator charge transfer transition with and without the K^+ ion for a range of computational methods.*

Method	$\Delta E_{noK^+}^{F\rightarrow C}$ (eV)	$\Delta E_{K^+}^{F\rightarrow C}$ (eV)
TD-B97-1	2.78	3.65
TD-CAM-B3LYP	4.36	4.34
ΔSCF^{SM}-B97-1	5.05	3.74
ΔSCF^{SM}(sol)-B97-1	2.57	3.29

Table 4.3. shows the computed transition energies for the lowest CT transition at a variety of levels of theory. For the TDDFT results with the hybrid B97-1 functional, without K^+, the transition energy for the lowest CT transition is 0.58 eV lower than that for the local fluorophore transition, while with K^+ the lowest CT transition is higher in energy than the fluorophore transition by 0.2eV. These results show a large difference

in charge transfer state energies depending on whether K^+ is bound to the sensor, and on their own are consistent with the experimental observations that K^+ will lead to enhanced fluorescence, due to the lower energy CT state for the non-chelated sensor. However, it is well known that TDDFT with hybrid functionals can severely underestimate the energy of CT states. A Λ analysis of the degree of spatial overlap between the occupied and virtual orbitals involved in an excitation gives a value of 0.00 for the CT transition compared with 0.68 for the local fluorophore transition, suggesting that the computed CT energy is unreliably low.

The long-range corrected functional CAM-B3LYP should provide a more accurate transition energy for the CT state and gives a value of 4.36 eV, with no significant change in CT energy once K^+ is bound to KS1. Consequently, with the CAM-B3LYP functional, there is no CT state lower in energy than the state formed from the local excitation ($\Delta E = 3.76$ eV) on the fluorophore which suggests that no PET process will occur. It should be noted that this energy difference is considerably larger than 0.1 eV, which is the approximate error associated with the basis set. Within a ΔSCF methodology, as opposed to TDDFT, CT states can be described with a hybrid functional and it is not necessary to use a long-range corrected functional. Using a spin-mixed ΔSCF framework in the gas phase a transition energy of 5.05 eV was obtained, which is much higher than the local fluorophore transition and consistent with results for TDDFT with CAM-B3LYP. For the CT state, it is found spin purification has a very small effect on the transition energy since the triplet state has a similar energy to the singlet state, so only the spin mixed transition energies are presented here. It is noted that converging the SCF process for the CT state using the MOM procedure was problematic for KS1 in the gas phase where variational collapse to the ground state could not be prevented using initial guesses based upon the ground state orbitals of the

gas phase molecule. These problems were not experienced for the PCM solvent calculations, and the gas phase value was obtained by using the converged orbitals for the CT state with the PCM as a starting point for the gas phase calculation. The dipole moment for the CT state is computed to be μ_{CT} = 82.3 D, which is much higher than the 9.01 D for the excited fluorophore state. This large difference suggests that the CT state will have a greater interaction with a polar solvent, which raises the possibility that the relative ordering of the local fluorophore excitation and the lowest CT excitation may be changed by the solvent, by lowering the energy of the CT state in a polar solvent. The results for the ΔSCF calculation with the implicit solvent model predicts that this is the case and the energy of the CT state lies (ΔE = 2.57 eV) below the local fluorophore excitation (ΔE = 3.02 eV). With K^+ present, the lowest CT transition is higher in energy than the excited fluorophore state for all of the calculations including ΔSCF with implicit polar solvent.

These calculations demonstrate that to reliably predict whether a PET process will occur in a metal ion sensor such as KS1 it is necessary to use an appropriate excited state method that can accurately describe charge transfer states and also account for solvent effects at least to the level of an implicit solvent model. This has been shown to be achieved with DFT based ΔSCF approaches but could also be achieved with TDDFT with long-range corrected functionals. However, it is necessary to account for the solvent contribution to the exchange correlation response, and it is not sufficient to simply use solvent polarised orbitals in the TDDFT equations. There are other effects that remain neglected in these calculations. The sensor has a significant amount of conformational flexibility, which cannot be captured by considering just a single structure. For smaller systems such as BODIPY, it is possible to compute absorption and emission spectra through averaging over molecular structures generated in an *ab*

initio molecular dynamics simulation [39]. However, such molecular dynamics calculations for a system as large as the K^+ sensor are prohibitively expensive, and here the focus has been on establishing a computationally efficient approach to reliably predicting the PET processes in a fluorescent sensor. Similarly, more complex solvent models could be used, including using explicit solvent molecules [150] or more elaborate continuum solvent models. The complexity of solvent model is not a large concern however, as solvent shifts arising in the sensor are electrostatic in origin and arise from the very different dipole moments between the local fluorophore and charge transfer excitations. These should be adequately described by the PCM solvent model used here.

4.3.4. Calculation of the Rate of Electron Transfer

The analysis of the KS1 sensor so far provides a qualitative prediction of what type of PET process is possible and can provide some insight into the PET process; this can be quantified through calculation of the rate of electron transfer using Marcus theory, and comparing the electron transfer rate from the fluorophore π→π* state and the charge transfer state [194, 195]. This approach has been used to predict the rate of electron transfer in a range of systems [196-198]. According to Marcus theory, the rate of electron transfer can be expressed as

$$k_{ET} = \frac{2\pi}{\hbar}|V_{F-CT}|^2 \frac{1}{\sqrt{4\pi\lambda k_B T}} exp\left[\frac{-(\lambda + \Delta G)^2}{4\lambda k_B T}\right] \quad (4.3)$$

where λ is the reorganisation energy, ΔG is the total change in energy between the two states, and V_{F-CT} is the electron transfer coupling. The ΔSCF(sol) calculations give values of λ = 0.75 eV and ΔG = 0.20 eV.

The electron transfer coupling V_{F-CT} is computed in a gas phase TDDFT calculation at the ground state structure with the CAM-B3LYP calculation but rescaled according to the energy difference between the states in the condensed phase to give a value of 5.9×10^{-3}eV. Combined together, these give a value of $k_{ET} = 5.98\times10^{6}s^{-1}$ for the rate of electron transfer. This suggests that the PET process occurs on the microsecond time scale, which is likely to be slower than most fluorescent processes, implying the electron transfer to a lower energy charge transfer state would not necessarily take precedence over any radiative processes.

4.4 Conclusions

In this study, the electronic structure and associated fluorescence properties of a K^+ ion sensor KS1 have been modeled with both DFT and TDDFT. Absorption and emission energies of the intense electronic excitation localised on the fluorophore are accurately described using a ΔSCF approach, which gives excitation energies closer to experiment than TDDFT. The extent to which Na^+ binds to this sensor and affects its fluorescent activity has been limited in this study to calculations of vertical absorption energies for the Na^+ bound sensor, and has shown that absorption energies are largely consistent within the basis set used regardless of the metal complexed with the sensor. The PET processes that underpin the functioning of the sensor cannot be rationalised based upon analysis of the molecular orbital diagram arising from DFT calculations for the isolated molecule or with implicit solvent. To correctly account for the functioning of the sensor, it is needed to consider relative energies of the electronic states formed from the local excitation on the fluorophore and the lowest fluorophore → chelator CT state. The inclusion of solvent in these calculations is critical since the strong interaction of the CT state with the solvent lowers its energy below the local fluorophore excited state making a reductive PET possible in the absence of K^+, while no such process is possible when the sensor is bound to K^+. This is consistent with experiment where it is suggested that a PET process quenches fluorescence in the absence of K^+. The rate of electron transfer using this method can be quantified using Marcus theory, and the rate of electron transfer is computed to be $k_{ET} = 5.98 \times 10^6 s^{-1}$, which implies the speed of a PET process is slower than a regular fluorescence process taking place on the nanosecond timescale.

5. Modelling Excited States of Weakly Bound Complexes with Density Functional Theory

5.1. Introduction

Kohn–Sham density functional theory (DFT) [21] has emerged as the most widely used quantum chemical method, and is used routinely to study a diverse range of problems, encompassing areas from materials science to biological systems, from small molecules to carbon nanotubes. A serious deficiency of using DFT when applied with common exchange–correlation functionals is its failure to describe long range van der Waals (dispersion) interactions accurately, more details of which can be found in chapter 2 of this thesis [199-201]. Dispersion interactions play a critically important role in areas such as supramolecular chemistry and protein structure, so should not be neglected. These forces also have a small impact on the energy and binding of all large and multi-molecular systems. In the case of electronically excited states, such interactions would also be important in the description of the structure of an excited chromophore within a biological system [152]. The poor description of dispersion interactions within DFT can be attributed to the assumption that the exchange–correlation functional is a functional of the local electron density for LDA functionals or the gradient of the local electron density for GGA functionals and many hybrid functionals. Wave function based methods, such as second-order MP2 and CCSD(T), can provide an accurate treatment of dispersion, due to their more accurate description of electron-electron interaction [202-204]. However, there remains a clear need for an accurate treatment of van der Waals interactions in computationally less demanding methods that can be applied to

study large systems, such as DFT. Consequently, incorporating dispersion within DFT is a very active area of research, and many different approaches have been developed.

One popular approach to incorporating dispersion within DFT is to parameterise functionals that do not contain an explicit dispersion term using systems where dispersion interactions are prominent. Examples of this approach are the M05 [34] and M06 [35] functionals, which have proven successful for modelling some dispersion bound complexes. Other approaches have included the development of effective core potentials to incorporate the effects of dispersion [205]. Alternatively, it is possible to treat dispersion explicitly as part of the exchange–correlation functional [206-208]. An emerging class of methods are those that attempt to treat dispersion rigorously via non-local functionals [209-213]. Although these methods increase the computational cost, they do hold promise of an accurate treatment of dispersion that is less empirical in nature. The most common approach for incorporating dispersion forces within DFT calculations, and the one that is focused on here, is based upon the addition of an empirically based damped $-C_6R^{-6}$ separation term in so-called DFT-D methods [3, 36, 214-216].

These methods have been described in detail earlier in this thesis; for a detailed description the reader is referred to section **2.6.3.**. Within the framework of parameterised DFT-D methods there is considerable scope to vary how the various parameters are optimised, in addition to defining the precise nature of the damping function and how the pairwise dispersion coefficients are determined from the respective atomic values [207]. These different approaches are typically assessed by comparison with data from accurate wave function based calculations on model systems, and benchmark data sets have been established [203]. The two empirical DFT-D methods studied are Grimme's D2 and D3 corrections [2, 3], as well as the directly

calculated XDM method [37, 38, 218, 219], which provides a mechanism to determine the dispersion coefficients directly from the electron density.

These methods have proven to be an important addition to the ever expanding number of DFT-based methods and are now used extensively. However, the application of these methods has nearly exclusively considered the interaction between molecules in the electronic ground state. The interaction within complexes where one component is in an electronically excited state is important in the context of spectroscopy in rare gas matrices and the condensed phase. Since the commonly used dispersion corrections are empirical, the underlying parameterisation using ground state data may not be suitable for an excited state that could have significantly different electronic structure. Previous work by Besley & Ershova has considered the interaction between argon and nitric oxide in its ground $X^2\Pi$ and excited $A^2\Sigma^+$ states with DFT with a range of corrections for dispersion [190]. For the ground state, the DFT based calculations were in good agreement with coupled cluster theory data, however none of the functionals gave satisfactory agreement for the excited state. More recently, Fukuda and Ehara studied electronic excitations in a free-base porphyrin–Ar_2 complex with symmetry-adapted cluster-configuration interaction (SAC-CI) and TDDFT [220]. In these calculations, TDDFT did not reproduce the observed shift to higher energy for the 1^1B_{3u} state but did correctly predict shifts to lower energy for the B-band states. In this work, the performance of DFT-D methods in describing weakly bound complexes where one component is in an electronically excited state is assessed relative to EOM-CCSD and MP2 calculations using two model complexes, ethene–argon and formaldehyde–methane, with different excited states. The ethene-argon complex in particular is considered as a model of $\pi \rightarrow \pi^*$ transitions in unsaturated hydrocarbons, so should give

results that can be reliably applied to other unsaturated hydrocarbons. The molecular complexes and different excited states studied are illustrated in ***Figure 5.1***.

(a)

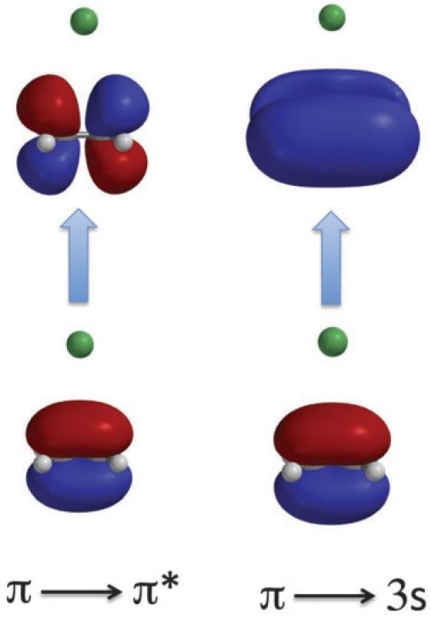

(b)

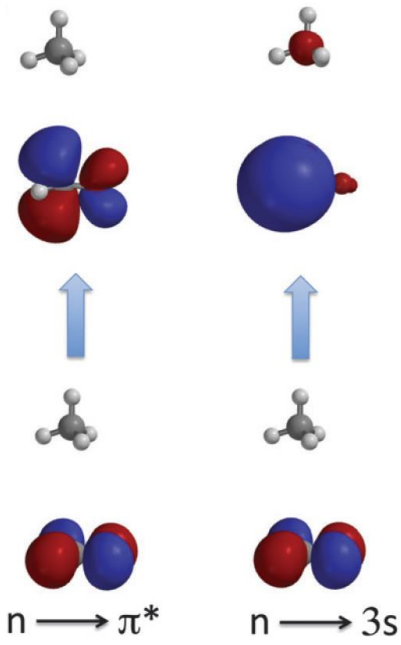

Figure 5.1. *The molecular orbitals involved in the electronic transitions. (a) ethene–argon and (b) formaldehyde–methane.*

5.2. Computational Details

For the argon-ethene system, the argon atom is placed above the centre of mass of the ethene molecule. The interaction energy is computed as *r* is varied, where *r* corresponds to the perpendicular distance between the centre of mass of ethene and the argon atom. No angular variations are considered. Along with the electronic ground state, the two excited states of ethene arising from the lowest $\pi \rightarrow \pi^*$ and $\pi \rightarrow 3s$ transitions are studied. For the formaldehyde-methane complex, the interaction energies for the ground state and excited states following $n \rightarrow \pi^*$ and $n \rightarrow 3s$ transitions of the formaldehyde are considered. In this complex, the methane molecule is placed directly above the carbon atom of the formaldehyde, perpendicular to the plane containing formaldehyde, with the perpendicular hydrogen atom of methane pointing away from the H_2CO. For this complex, *r* represents the distance between the two carbon atoms of the separate molecules.

Potential energy curves have been computed for the ground and excited states of the molecular systems using EOM-CCSD, MP2, DFT and DFT-D methods. All MP2 and DFT calculations were corrected for basis set superposition error using the counterpoise correction, where the molecular orbitals of the whole system was considered when looking at the energies of the individual molecules [14]. EOM-CCSD calculations were performed in conjunction with the aug-cc-pVDZ basis set. Additional CCSD and EOM-CCSD calculations to determine the binding energy with the larger aug-cc-pVTZ basis set were performed to assess the convergence of the calculated interaction energies with respect to the size of the basis set. These calculations were performed at the minimum separation according to the aug-cc-pVDZ basis set calculations, and full potential energy curves were not computed using this larger basis set. For the MP2 and DFT

calculations, excited states were determined by applying the MOM procedure [45]. This procedure has been applied to study the excited states in a variety of systems, and has already been used in extensively in the other chapters of this work [46, 47, 191, 221]. For the excited state calculations presented here, the complex is initially considered at a large separation of 8 Å with the molecular geometries optimised at the MP2/cc-pVTZ level. The ground state orbitals with the occupancies altered to reflect the relevant excited state are used as the initial guess for the MOM calculation to generate the excited state on convergence of the energy. Subsequently, the intermolecular separation was reduced in a stepwise manner of 0.01 Å per step to a final separation of 2 Å, and for each calculation the converged orbitals from the previous step were used as the initial guess. By following this procedure, the MOM approach was able to prevent any variational collapse to the ground state. For the MP2 calculations, the correlation energy was extrapolated to the complete basis set (CBS) limit using a two-point extrapolation relationship [222] based upon the aug-cc-pVDZ and aug-cc-pVTZ basis sets. Alternative methods such as the algebraic diagrammatic construction (ADC) scheme could be considered to study the excited states within a wavefunction based formalism. However, this approach would be expected to give results that are similar to EOM-CCSD and MOM-MP2 methods, which are considered appropriate benchmark calculations for comparing with the DFT-D results.

DFT calculations have been performed with the B3LYP [25, 26] and PBE [22, 223] exchange-correlation functionals in conjunction with the D2, D3 and XDM dispersion corrections and with the aug-cc-pVTZ basis set. Standard values of the scaling factors for B3LYP and PBE were used in the D2 and D3 dispersion corrections [3, 4], and the 3-body interaction term in the D3 correction was not applied. The van der Waals radii of the atoms were applied in the DFT-D methods initially with default values, then with

modified values for the D2 dispersion correction. For the XDM correction, Becke's damping function including only the C6 term was used. In order to obtain smooth potential energy curves a 250 point Euler-Maclaurin radial integration grid with 590 point Lebedev angular grid was used. All calculations were performed with the Q-Chem software package [192].

5.3. Results & Discussion

5.3.1. EOM-CCSD and MP2

Figures 5.2 and ***5.3*** show the computed EOM-CCSD, MP2/CBS, B3LYP and B3LYP-D3 potential energy curves for the ethene–argon and formaldehyde–methane complexes, with the binding energies and geometries of the minima given in ***Table 5.1.*** Initially, the EOM-CCSD and MP2 curves will be discussed. The ground state of ethene–argon is predicted to be bound by -595 μE_h with a separation of r_e=4.1 Å at the CCSD/aug-cc-pVDZ level, with the binding energy at 4.1 Å increasing to -763 μE_h with the larger aug-cc-pVTZ basis set. At the MP2 level a binding energy of -681 μE_h at a separation of r_e=3.8 Å is obtained, which is in reasonable agreement with the CCSD values. The focus of this study is the interaction when the molecule is in an excited state, and if a comparable degree of accuracy is obtained for excited states as is observed for the ground state. If ethene is excited to the $\pi \rightarrow \pi^*$ excited state, there is a large increase in the strength of the interaction, with the binding energy for the CCSD/aug-cc-pVDZ method increasing to -2454 μE_h and r_e decreasing to 3.1 Å. This binding energy changes to -2289 μE_h for the larger basis set. A significant increase in the binding energy compared to the ground state is also predicted by the MP2 calculations, with a computed binding energy of -2890 μE_h and a separation of 3.3 Å. These values seem consistent with the idea that the centre of the carbon double bond in ethene sees a decrease in electron density from the π to the π^* orbital, thus allowing a closer optimum binding separation and stronger interaction in the $\pi \rightarrow \pi^*$ state.

Table 5.1. *Computed binding energies (in μE_h) of the complexes with the minimum energy separation (in Å) in parenthesis.*

Complex	State	(EOM)-CCSD/ aug-cc-pVDZ	MP2/CBS	B3LYP/ aug-cc-pVTZ	B3LYP-D3/ aug-cc-pVTZ
C_2H_4-Ar	g.s.	-595.2 (r_e=4.1)	-680.8 (r_e=4.1)	No binding	-459.3 (r_e=3.9)
	π→π*	-2453.6 (r_e=3.1)	-2889.7 (r_e=3.1)	No binding	-1780.1 (r_e=3.3)
	π→3s	-284.1 (r_e=3.1)	107.2 (r_e=3.1)	No binding	-2308.4 (r_e=3.0)
		-123.8 (r_e=6.2)	-154.4 (r_e=6.2)		
H_2CO-CH_4	g.s.	-1150.8 (r_e=3.6)	-1230.7 (r_e=4.1)	<-10.1 (r_e>8.0)	-1000.3 (r_e=3.6)
	π→π*	-854.0 (r_e=3.9)	-444.4 (r_e=3.1)	<-4.6 (r_e>8.0)	-513.3 (r_e=3.9)
	π→3s	138.7 (r_e=3.6)	-836.8 (r_e=3.1)	-20.6 (r_e=7.9)	-2003.7 (r_e=3.2)
		-258.0 (r_e=6.0)	-232.9 (r_e=6.2)		

The potential energy curve for the π→3s state is more complex with two minima. EOM-CCSD predicts these minima to lie at 3.1 Å and 6.2 Å with binding energies of -284 μE_h and -124 μE_h, respectively. The MP2 calculations give a potential energy curve with a similar shape, although the depth of the minimum at short range is underestimated compared to the coupled cluster calculations. The observed shape of this potential energy curve suggests that there may be an avoided crossing. For ethene this is unlikely to be the case since the next excited state is a Rydberg π→3p state that lies about 0.5 eV higher in energy. This high energy gap suggests crossing is not a feasible option for the ethene molecule in this state. Furthermore, there would also be a change in electronic state as the separation is increased. Within the MOM formalism the nature of the excited state is explicitly maintained during the calculations, which excludes the possibility of

a change of state. However, for a Rydberg state that by its nature is more diffuse than valence states, a minimum at larger r values is not surprising.

The ground state of the formaldehyde–methane complex is relatively strongly bound compared with argon-ethene, with a binding energy of -1151 μE_h and r_e=3.6 Å calculated at the CCSD/aug-cc-pVDZ level. For both of the excited states the binding energy at the minimum decreases, particularly for the Rydberg n→3s state. Similar to the π→3s state of ethene–argon, the potential energy curve for the n→3s state shows two minima, a deeper one at r_e=6.0 Å and a more shallow minimum at r_e=3.6 Å. The potential energy curves computed with MP2 show similar features. The binding energy for the ground state is predicted to be 80 μE_h greater compared to CCSD, while for the n→π* state the predicted r_e is in good agreement with EOM-CCSD, but the binding energy is significantly smaller at -444.4 μE_h, only being slightly over half the binding energy of that for EOM-CCSD.

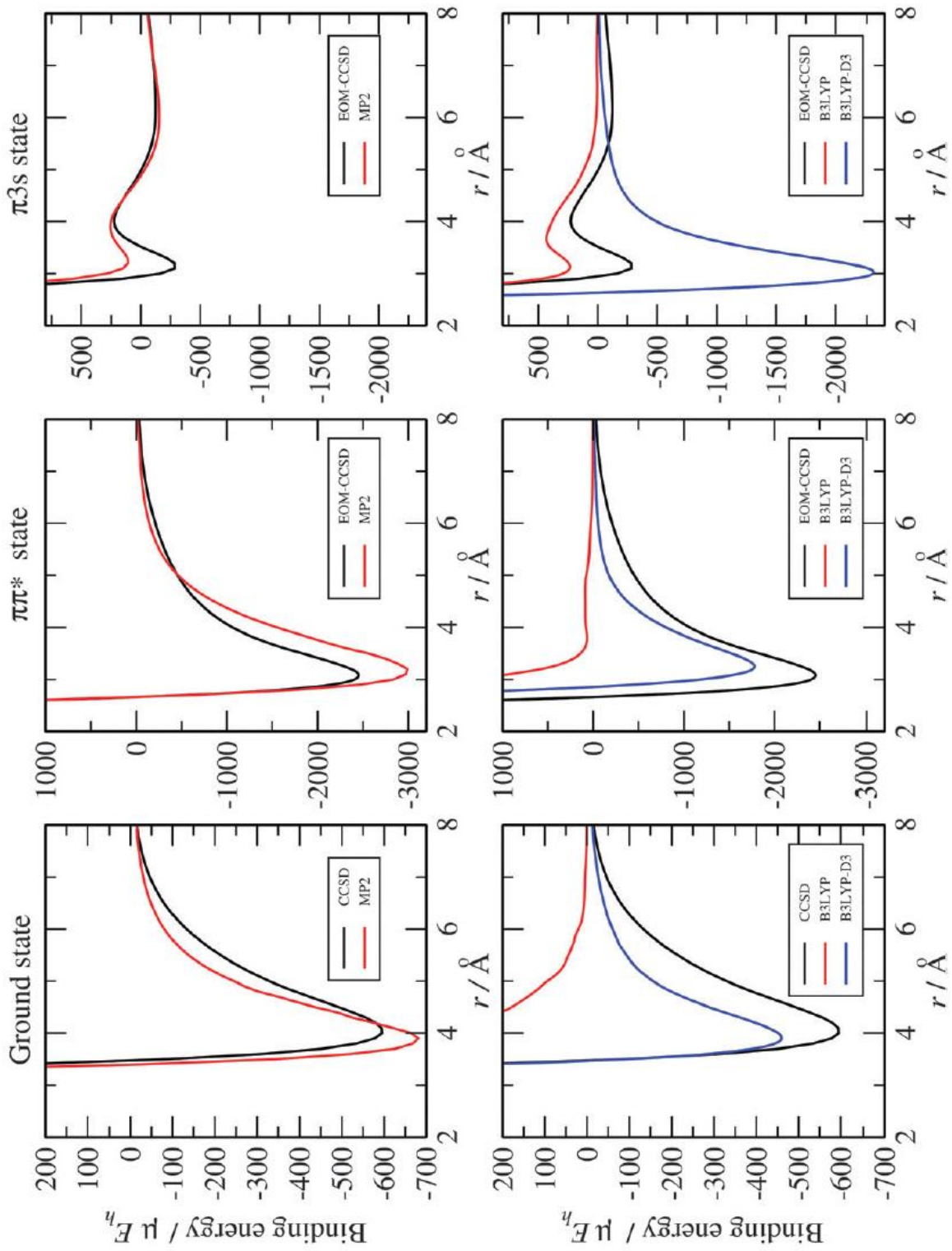

Figure 5.2. *Computed potential energy curves for the ground and excited states of the ethene–argon complex.*

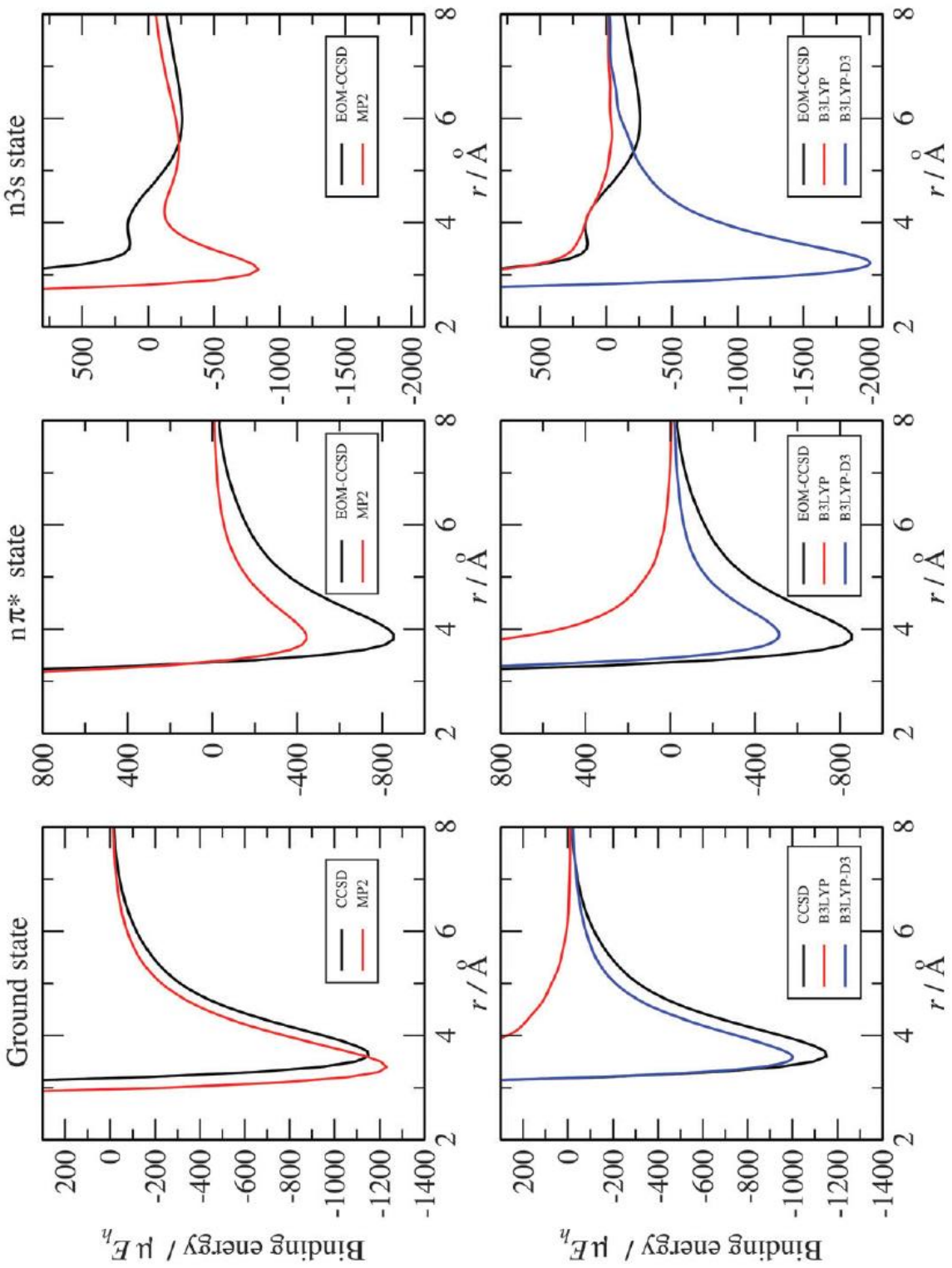

Figure 5.3. *Computed potential energy curves for the ground and excited states of the formaldehyde–methane complex.*

For the n→3s state two minima are found with MP2, but like ethene–argon the depth of the minimum at short range is larger than the one at larger separation. This short range minimum is much bigger than that for the EOM-CCSD calculations, and this shows the largest difference of binding energies for a minimum over all the EOM-CCSD and MP2 calculations. Despite these discrepancies and other small differences between the precise values of the binding energies, the EOM-CCSD and MP2 calculations do provide a reasonably consistent picture of the potential energy curves of the different electronic states. For the ethene–argon complex the binding energy in the ground state is about 600–700 μE_h with a large, approximately four fold increase, in the binding energy for the π→π* state. For the π→3s state a minimum at short-range (~3.1 Å) and long-range (~6.2 Å) are observed. The ground state of formaldehyde–methane is more strongly bound with a binding energy of ~1200 μE_h and there is a decrease in the strength of the interaction for the n→π* state. Again, for the Rydberg state two minima are observed. The minimum at larger *r* has a binding energy of ~250 μE_h, while there is disagreement over the binding energy for the minimum at shorter r. From these benchmarking calculations of the binding energies, it was now possible to compare to these results with the variety of DFT and DFT-D methods outlined previously.

5.3.2. DFT and DFT-D

Figures 5.2. and ***5.3.*** also show the computed potential energy curves for the DFT and DFT-D calculations with the B3LYP functional, with and without the D3 dispersion correction using the aug-cc-pVTZ basis set. The D3 correction was applied here as the D3 method is the most commonly used dispersion correction, and has shown to give good results for ground state calculations. For the ethene–argon system, no binding is predicted for any of the states when dispersion is not included. It is interesting to note that for the π→3s state, the distinct shape with a minimum at 3.1 Å and maximum at ~4 Å that is present in the MP2 and EOM-CCSD calculations is evident. However the more long range minimum is not found for the regular B3LYP calculations. This suggests that for this state, the minimum observed at larger separation r arises from dispersion forces, as well as the minima for the ground and π→π* state. For this complex the binding arises from the dispersion correction, and with the inclusion of dispersion the resulting potential energy curves for the ground state and π→ π* state are in qualitative agreement with the wave function based calculations. The predicted values of r_e are in close agreement with the wave function based calculations, with the largest difference in separation minima being with the π→ π* state, where the B3LYP-D3 result is 0.2 Å above the EOM-CCSD r_e value. The depths of the minima for the ground and π→ π* state are underestimated by about 20–30%. In contrast, for the π→ 3s Rydberg state the inclusion of dispersion leads to significant deviation from both EOM-CCSD and MP2 calculations. The resulting curve has a deep minimum at 3.0 Å and shows a significantly larger deviation from the EOM-CCSD and MP2 results than the B3LYP with no dispersion curve. A similar picture emerges for the formaldehyde–methane system.

Looking at the formaldehyde-methane calculations, binding is not observed in the regular B3LYP-DFT calculations for any of the three states. Once the dispersion correction is included binding is observed, and there is reasonable agreement with the wave function based results for the ground state and n→π* states. However, as seen with the ethene-argon system, for the Rydberg state the binding energy is much too large. These results show that while the dispersion correction works quite well for the valence excited states, its performance for the Rydberg excited states is much poorer. This suggests that the electronic structure of the Rydberg excited state is sufficiently different from that of the ground state to make the parameterisation of the dispersion correction no longer appropriate.

Table 5.2. *Computed binding energies (in μE_h) and minimum energy separations (in Å) for ethene–argon with different functionals.*

Method	Ground state	π→π* state	π→3s state
B3LYP-D3	-459.3 (r_e=3.91)	-1780.1 (r_e=3.25)	-2308.4 (r_e=3.03)
B3LYP-D2	-289.4 (r_e=3.89)	-1605.6 (r_e=3.25)	-2081.8 (r_e=3.06)
B3LYP-XDM	-113.2 (r_e=4.22)	-845.7 (r_e=3.35)	-1351.2 (r_e=2.94)
PBE	-112.8 (r_e=4.77)	-299.5 (r_e=4.41)	-658.3 (r_e=3.36)
PBE-D3	-587.1 (r_e=4.12)	-1421.2 (r_e=3.53)	-3091.1 (r_e=3.16)
PBE-XDM	-390.6 (r_e=4.39)	-787.1 (r_e=3.85)	-1849.7 (r_e=3.20)
(EOM)-CCSD	-762.9 (r_e=4.1)	-2288.6 (r_e=3.1)	-628.3 (r_e=3.1)

B3LYP-D3 represents only one of the many possible combinations of exchange–correlation functional and dispersion correction. ***Figure 5.4.*** shows computed potential energy curves for alternative dispersion corrections and exchange–correlation

functionals, with the computed properties of the minima given in ***Table 5.2.*** The potential energy curves computed using B3LYP-D2 are very similar to B3LYP-D3, with little variation in the location of the minima but for all three states the strength of binding is predicted to be weaker with the D2 correction with the ground state binding energy for D2 around half of that when using the D3 correction. The valence and Rydberg excited states both see binding decrease around 10% with the D2 correction compared to D3. With the XDM dispersion correction the binding is further weakened and significantly underestimated relative to EOM-CCSD. For the PBE exchange–correlation functional distinct minima are observed for all three states when no dispersion correction is applied. This is in contrast to B3LYP where no binding is predicted in the absence of a DFT-D correction. In fact it is found for the ground state the depth of the minima for PBE is comparable to B3LYP-XDM albeit at a larger value of r (4.77Å compared to 4.22 Å). For the $\pi \rightarrow 3s$ state, the curve for B3LYP resembles those from EOM-CCSD and MP2, while the PBE curve is significantly different. This suggests that B3LYP represents a better choice of underlying exchange–correlation functional. PBE in conjunction with D3 and XDM corrections largely overestimate the value for the equilibrium separation and underestimate the binding compared to EOM-CCSD for the ground and $\pi \rightarrow \pi^*$ states. Crucially, while many of the DFT-D calculations provide a reasonable description for the ground and $\pi \rightarrow \pi^*$ states of the ethene–argon complex, none are correct for the $\pi \rightarrow 3s$ state. This is consistent with earlier work done by Ershova & Besley on the excited $A^2\Sigma^+$ Rydberg state of the NO–Ar complex, where poor agreement with high level wave function based calculations was observed [32].

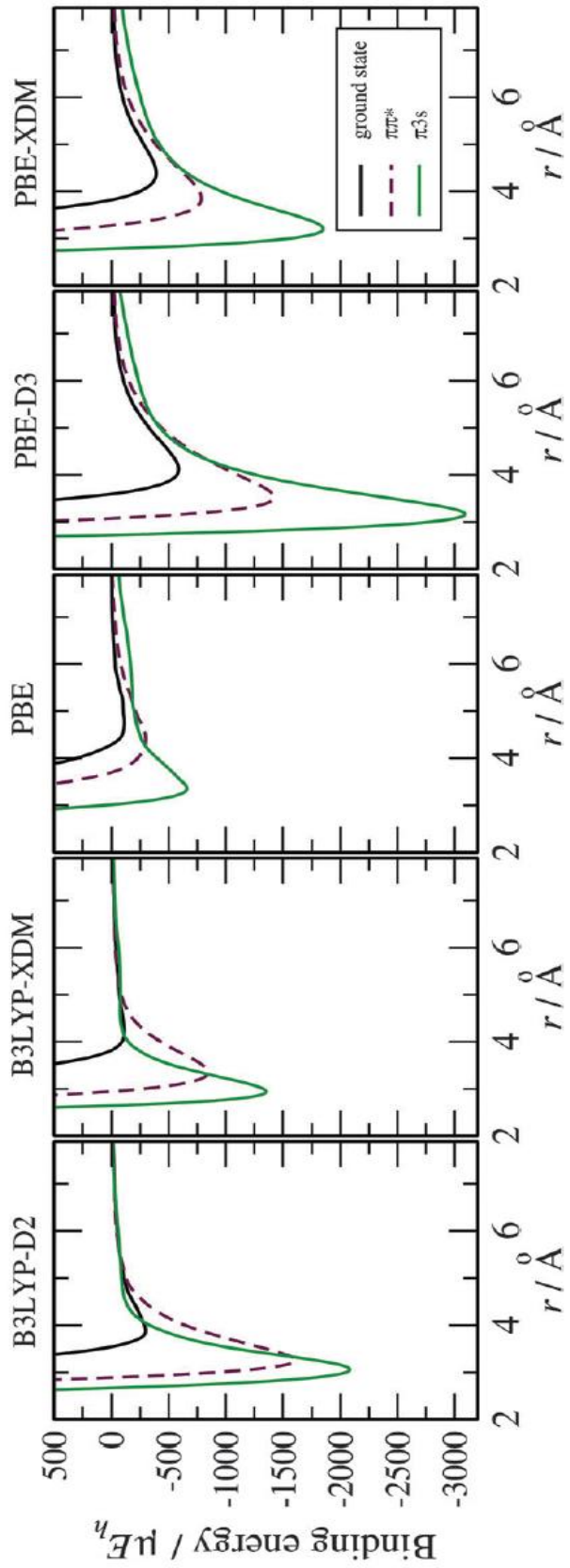

Figure 5.4. *Computed DFT/aug-cc-pVTZ potential energy curves for the ground and excited states of the ethene–argon complex.*

5.3.3. Variation of the dispersion correction

The discrepancy for the π→3s state of ethene–argon is illustrated clearly in ***Figure 5.5.***, which shows the difference between the EOM-CCSD curve and the B3LYP curve without the addition of dispersion. This indicates how a dispersion correction for this state would appear in order to bring the B3LYP curve into agreement with EOM-CCSD. This 'correct' dispersion contribution has a minimum of approximately 525 μE_h at a separation of 3.2 Å. Also plotted is the actual dispersion contribution as given by the D2 dispersion correction with default parameters.

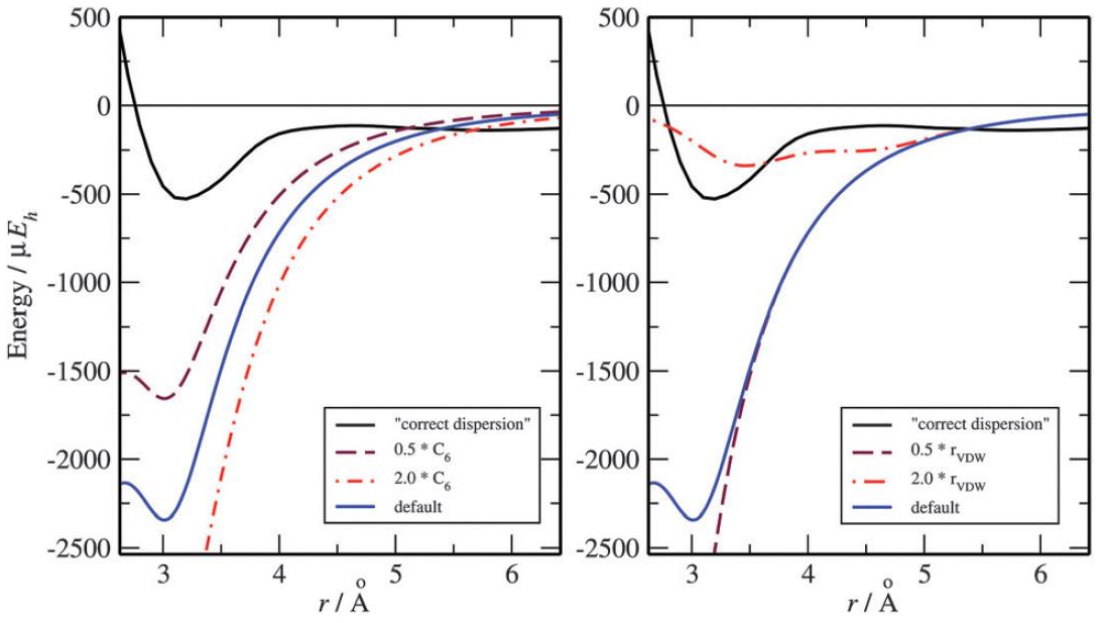

Figure 5.5. *Comparison of the correct dispersion contribution and D2 dispersion.*

At long range the D2 dispersion correction is too small, but more significantly the minimum at 3.2 Å is much too deep. This indicates that the parameterisation of the dispersion correction for the ground state is not appropriate for the excited Rydberg state. In order to explore how the dispersion contribution varies as the key parameters in the D2 correction are changed, the dispersion contributions arising from reducing and increasing the C_6 coefficients and Van der Waals radii are shown. Reducing the C_6

coefficients for carbon and hydrogen to half the original value. Looking at Eq. (5.2) shows that a reduction in C_6 values will reduce the magnitude of the binding observed. This is shown in a reduction of the depth of the minimum, but a significant deviation from the correct dispersion curve remains and the C_6 would have to be significantly reduced to agree with the correct dispersion values. Increasing C_6 coefficients for carbon and hydrogen to double the original value shows a large increase in the magnitude of the binding energy.

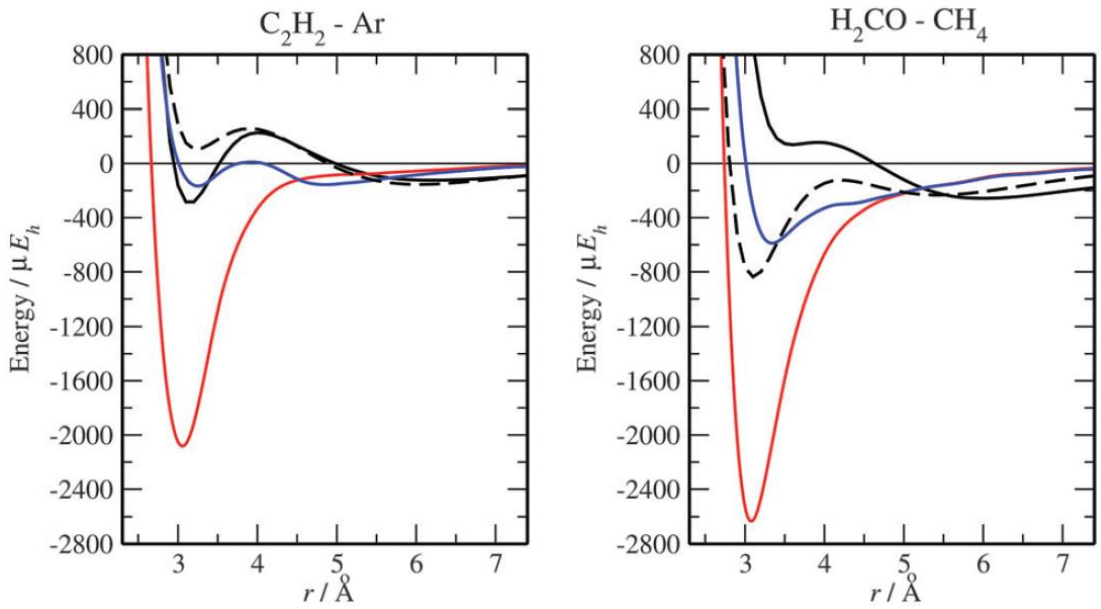

***Figure* 5.6.** *Computed potential energy curves for the π⟶3s state of ethene–argon and n⟶3s state of formaldehyde–methane (Black line: EOM-CCSD/aug-cc-pVDZ, broken black line: MP2/CBS, red line: B3LYP-D2 with default parameters, blue line: B3LYP-D2 with increased van der Waals radii).*

Increasing the van der Waals radii of carbon and hydrogen has a greater effect and the resulting dispersion contribution is considerably closer to the correct one. As the sum of van der Waals radii R_{AB}^0 is part of the damping function of the dispersion correction, changing this value can affect the separation at minimum energy r_e. It is seen an increase

in van der Waals radii increases the binding separation while reducing the binding energy, and vice versa for decreasing the van der Waals radii. The fact that increased van der Waals radii for the Rydberg state leads to more correct values has some physical basis since Rydberg states are known to have a greater spatial extent than valence states, however, such a large increase of a factor of two is hard to justify based upon analysis of the electron densities.

Figure 5.6. shows the resulting potential energy curves for the π→3s state of ethene–argon and n→3s state of formaldehyde–methane with modified van der Waals radii. For the formaldehyde–methane complex the van der Waals radii of the atoms in formaldehyde are increased by a factor of two, while the van der Waals radii for the methane atoms are not changed from their default value. For both of these states, the resulting potential energy curve with the modified D2 parameters (blue lines) are much closer to the EOM-CCSD and MP2 curves compared to the potential energy curve with default parameters (red line). For the ethene–argon complex the new B3LYP-D2 curve is in excellent agreement with the wave function based methods. A larger deviation is observed for formaldehyde–methane, but the resulting curve is comparable with that from MP2. This demonstrates that the nature of the EOM-CCSD curves can be captured by the D2 correction, and clearly with a more comprehensive re-parameterisation more accurate curves would result.

5.4. Conclusions

The description of the ground and excited states of the two weakly bound complexes, ethene–argon and formaldehyde–methane, with DFT-D based methods has been assessed relative to EOM-CCSD and MP2 calculations. In the ethene–argon complex, excitation of ethene to give the $\pi \rightarrow \pi^*$ state leads to an increase in the strength of binding, while the complex is more weakly bound on excitation to the $\pi \rightarrow 3s$ state, with a double minimum present. For the formaldehyde–methane complex, both excitation to $n \rightarrow \pi^*$ and $n \rightarrow 3s$ states lead to weaker binding compared to the ground state. DFT-D calculations with the dispersion component modelled according to the empirical scheme of Grimme reproduce the potential energy curves for the ground and valence excited states with a good level of accuracy. For the $\pi \rightarrow 3s$ and $n \rightarrow 3s$ Rydberg states, B3LYP-D3 calculations predict the binding to be much too strong, with the regular B3LYP results with better agreement with benchmark calculations, although binding much too weak. For the $\pi \rightarrow 3s$ state of ethene–argon this is also observed with a variety of DFT-D approaches. This is despite the uncorrected B3LYP potential energy curve providing a reasonable description of the EOM-CCSD and MP2 curves. It is found that the parameters of the DFT-D methods must be altered to better model these Rydberg states.

Modification of the C_6 and van der Waals radii within the D2 correction shows that a significantly improved agreement with the wave function based methods is achieved if the atomic van der Waals radii are greatly increased. This demonstrates that these states can be described within the framework of a mathematically simple dispersion term but that the appropriate parameters will be different from the ground state, and these parameters may not represent the real physical measurements of the excited state that the parameters should be modelled on. This clearly has consequences for describing the

excited states of such systems with TDDFT based upon Kohn–Sham DFT-D calculations, which assume that the dispersion in the excited state is the same as in the ground (reference) state. Clearly, for the B3LYP and PBE functionals considered here, excitations to Rydberg states would require a state specific dispersion correction. This would be difficult to realise within current TDDFT approaches.

6. Conclusions & Future Work

This thesis has covered three research projects focused on the main aim of studying fluorescence spectroscopy and excited states using DFT and TDDFT. It has encompassed a wide variety of quantum chemical methods, including *ab initio* wavefunction based methods such as MP2 and CCSD(T) as well as DFT, with a common theme of using MOM to calculate excited states in a ΔSCF framework in all three projects.

Firstly, absorption and emission spectra arising from the lowest energy transition in BODIPY were simulated in the gas phase and water using a QM/MM approach along with MOM to calculate excited states. Application of a post-self-consistent field spin-purification relationship gave transition energies in agreement with CASPT2 and available experimental data. Spectral bands were calculated from simulations where DFT was used for BODIPY, and in the condensed phase simulations the water molecules were treated classically. The resulting spectra showed a blue shift of 0.3 eV in water compared to the gas phase. A Stokes shift of about 0.1 eV is predicted, and the width of the emission band in solution is significantly broader than the absorption band. The absorption and emission results are consistent with experimental data for BODIPY and closely related dyes, and demonstrate how both absorption and emission spectra in solution can be simulated using a quantum mechanical treatment of the electronic structure of the solute.

Looking to the future, this work has laid out a reliable way to calculate absorption and emission bands of a fluorescent molecule, using DFT/B97-1 in an AIMD simulation combined with SP-MOM for excited states and a TIP3P water potential. This theoretical framework could potentially be applied to other fluorescent molecules: the three PM

dyes which underwent structural analysis in chapter 3 would be potential molecules for this treatment. The work could expand to include other fluorophores such as RH dyes or 4-aminonaphthalene-containing molecules as studied in chapter 4. The level of theory could be studied further, as various QM/MM solvent methods along with exchange-correlation functionals have not been investigated in this work. The first solvent shell of water around BODIPY could also be feasibly modelled with direct DFT as opposed to point charges, which could give a more accurate description of BODIPYs behavior in a water solvent.

The structural analysis of the BODIPY derivatives from chapter 3 showed interesting results, as the S_1 states of derivatives was found to deviate from a planar shape. Further investigation into the non-planarity of the S_1 state, could show any exceptions to this deviation or how it affects the properties of the molecules. The work with *meso*-substituted BODIPY shows that the amount of or lack of planarity can be changed by varying the substituents. It would be possible to provide a structural analysis of a wider range of BODIPY derivatives to further understand how the planarity is affected by substituents, and how that will affect absorption and fluorescence of the molecule.

For the second project in this thesis, the electronic structure and associated fluorescence properties of the K^+ ion sensor KS1 have been modeled with both DFT and TDDFT. Absorption and emission energies of the intense electronic excitation localised on the fluorophore are accurately described using a ΔSCF approach, which gives excitation energies closer to experiment than TDDFT. The PET processes that underpin the functioning of the sensor were rationalised by considering relative energies of the electronic states formed from the local excitation on the fluorophore and the lowest fluorophore → chelator CT state. It was found that the inclusion of solvent in these calculations is critical due to the strong interaction of the CT state with the solvent

lowers the CT state energy below the local fluorophore excited state making a reductive PET possible in the absence of K^+, while no such process is possible when the sensor is bound to K^+. This helps confirm the reductive PET process first suggested by Zhou et. al [2] is reflective of the photophysics of the molecule.

This work could be continued easily to apply the same theory to other similar fluorescent sensors, as so far only one molecule has been studied. This would further confirm the viability of this method in determining the fluorescent behavior of molecules, as well as being applied to newly developed sensors to assess their fluorescence with a variety of chelated metal ions.

The final project provided a description of the potential energies of ground and excited states of two weakly bound complexes, ethene–argon and formaldehyde–methane, with DFT-D based methods relative to EOM-CCSD and MP2 calculations. For the ethene–argon complex, excitation of ethene to give the valence $\pi \rightarrow \pi^*$ state leads to an increase in the strength of binding, while the complex is more weakly bound on excitation to the Rydberg $\pi \rightarrow 3s$ state. For the formaldehyde–methane complex, both excitation to $n \rightarrow \pi^*$ and $n \rightarrow 3s$ states lead to weaker binding compared to the ground state. For the $\pi \rightarrow 3s$ and $n \rightarrow 3s$ Rydberg states, B3LYP-D3 calculations predict the binding to be much too strong, with the regular B3LYP results with better agreement with benchmark calculations, although with weaker binding. It is found that the parameters of the DFT-D methods must be altered to better model these Rydberg states. Modification of the C_6 and van der Waals radii within the D2 correction show a significantly improved agreement with the wave function based methods can be achieved if the atomic van der Waals radii are greatly increased, however these have to be increased much more than any physical rationalisation can explain. This demonstrates that these Rydberg states can be described within the framework of a mathematically simple dispersion term but

that the appropriate parameters will be different from the ground state. This leads to the conclusion that for the B3LYP and PBE functionals considered here, excitations to Rydberg states would require a state specific dispersion correction. This would be difficult to realise within current TDDFT approaches. Future work in this area could find some way of rationalising parameters for the excited Rydberg states for a range of molecules, undergoing some sort of analysis of all parameters to find the best agreement with more accurate wavefunction-based methods. One could also study the valence and Rydberg states of other weakly bound molecules, as well as apply different DFT-D methods such as functionals which deal directly with dispersion effects.

The work carried out in this thesis has shown a variety of techniques and methodology related to quantum chemical calculations of fluorescence and excited states, with a focus on using DFT to obtain results in agreement with experiment. These results can mostly be rationalised in terms of the methods used and provide new ways to apply these methods, except for the reparameterisation of the DFT-D2, which shows how much more work in that area is needed to achieve accurate dispersion corrections for Rydberg states.

References

1. Ulrich, G.; Ziessel, R.; Harriman, A. The Chemistry of Fluorescent Bodipy Dyes: Versatility Unsurpassed. *Angew. Chem. Int. Ed.* **2008,** *47,* 1184−1201.
2. Zhou, X.; Su, F.; Gao, W.; Tian, W.; Youngbull, C.; Johnson, R.H.; Meldrum, D.R. Triazacryptand-Based Fluorescent Sensors for Extracellular and Intracellular K^+ Sensing. *Biomaterials*, **2011**, *32,* 8574-8583.
3. Grimme, S. Semiempirical GGA-type density functional constructed with a long-range dispersion correction *J. Comput. Chem.* **2006,** *27,* 1787–1799.
4. Grimme, S.; Antony, J.; Ehrlich, S.; Krieg, H. A consistent and accurate *ab initio* parametrization of density functional dispersion correction (DFT-D) for the 94 elements H-Pu *J. Chem. Phys.* **2010,** *132,* 154104.
5. Born, M.; Oppenheimer, R. Quantum Theory of Molecules. *Ann. Phys.,* **1927,** *84,* 457-484.
6. Hartree, D. R. The Wave Mechanics of an Atom with a Non-Coulomb Ventral Field. Part I. Theory and Methods. *Math. Proc. Cambridge Philos. Soc.,* **1928,** *24,* 89-110.
7. Fock, V. Approximation Method for the Solution of the Quantum Mehanical Multibody Problems. *Z. Physik,* **1930,** *61,* 126-148.
8. Slater, J. C. A Simplification of the Hartree-Fock method. *Phys. Rev.,* **1951,** *81,* 385-390.
9. Roothan, C. C. J. New Developments in Molecular Orbital Theory. *Rev. Mod. Phys.,* **1951,** *23,* 69-89.
10. Hall, G. G. The Molecular Orbital Theory of Chemical Valency. VIII. A Method of Calculating Ionization Potentials. *Proc. R. Soc. A,* **1951,** *205,* 541-552.

11. Binkley, J. S.; Pople, J. A.; Hehre, W. J. Self-consistent Molecular-orbital Methods .21. Small Split-valence Basis Sets for First-row Elements. *J. Am. Chem. Soc.* **1980,** *102,* 939-947.
12. Dunning, T. H. Gaussian Basis Sets for use in Correlated Molecular Calculations. I. The Atoms Boron through Neon and Hydrogen. *J. Chem. Phys.* **1989,** *90,* 1007-1023.
13. Parthiban, S.; Martin, J. M. L. Assessment of W1 and W2 theories for the computation of electron affinities, ionization potentials, heats of formation, and proton affinities *J. Chem. Phys.* **2001**, *114,* 6014-6029.
14. Boys, S. F.; Bernardi, F. Calculation of Small Molecular Interactions by Differences of Separate Total Energies- Some Procedures with Reduced Errors. *Mol. Phys.* **1970,** *19,* 553-566.
15. Møller, C.; Plesset, M. S. Note on Approximation Treatment for Many Electron Systems. *Phys. Rev.* **1934,** *46,* 618-622.
16. Cizek, C. On the correlation problem in atomic and molecular systems, Calculation of wavefunction components in Ursell-type expansion using quantum-field theoretical methods. *J. Chem. Phys.* **1966,** *45,* 4256-4266.
17. Raghavachari, K.; Trucks, G. W.; Pople, J. A.; Head-Gordon, M. A fifth-order perturbation comparison of electron correlation theories *Chem. Phys. Lett.* **1989,** *157*, 479-483.
18. Purvis, G. D.; Bartlett, R. J. A full coupled-cluster singles and doubles model: The inclusion of disconnected triples *J. Chem. Phys.* **1982** *76,* 1910-1918.
19. Cooper, B.; Knowles, P. J. Benchmark studies of variational, unitary and extended coupled cluster methods. *J. Chem. Phys.* **2010,** *133*, 234102.

20. Hohenberg, P.; Kohn, W. Inhomogeneous Electron Gas. *Phys. Rev. B* **1964,** *136,* 864-871.
21. Kohn, W.; Sham, L. J. Self-Consistent Equations Including Exchange and Correlation Effects *Phys. Rev. A* **1965,** *140,* 1133-1138.
22. Perdew, J. P.; Burke, K.; Ernzerhof, M. Generalized Gradient Approximation Made Simple. *Phys. Rev. Lett.* **1996,** *77,* 3865-3868.
23. Becke, A. D. Density-functional exchange-energy approximation with correct asymptotic behaviour. *Phys. Rev. A* **1988,** *38,* 3098-3100.
24. Lee, C.; Yang, W.; Parr, R. G. Development of the Colle-Salvetti correlation-energy formula into a functional of the electron density. *Phys, Rev. B,* **1988,** *37,* 785-789.
25. Becke, A.D. Density functional thermochemistry. III. The role of exact exchange. *J. Chem. Phys,* **1993,** *98,* 5648-5652.
26. Stephens, P. J.; Devlin, F. J.; Chabalowski, C. F.; Frisch, M. J. *Ab initio* calculation of vibrational absorption and circular dichroism spectra using density functional force fields. *J. Phys. Chem.,* **1994,** *98,* 11623-11627.
27. Vosko, S. H.; Wilk, L.; Nusair, M. Accurate spin-dependent electron liquid correlation energies for local spin density calculations: a critical analysis. *Can. J. Phys.,* **1980,** *58,* 1200-1211.
28. Becke, A.D. Density-functional thermochemistry. V. Systematic optimization of exchange-correlation functionals. *J. Chem. Phys,* **1997,** *107,* 8554-8560.
29. Hamprecht, F. A.; Cohen, A. J.; Tozer, D. J.; Handy, N. C. Development and assessment of new exchange-correlation functionals. *J. Chem Phys.* **1998,** *109,* 6264-6271.

30. Lange, A.; Herbert, J. M. Simple Methods To Reduce Charge-Transfer Contamination in Time-Dependent Density-Functional Calculations of Clusters and Liquids. *J. Chem. Theory Comput.* **2007,** *3,* 1680-1690.
31. Yanai, T.; Tew, D. P.; Handy, N. C. A New Hybrid Exchange-Correlation Functional Using the Coulomb-Attenuating Method (CAM-B3LYP). *Chem. Phys. Lett.* **2004,** *393,* 51−57.
32. Chai, J. D.; Head-Gordon, M. Systematic optimization of long-range corrected hybrid density functionals *J. Chem. Phys.* **2008,** *128,* 084106.
33. Zhao, Y.; Truhlar, D. G. Density Functional for Spectroscopy: No Long-Range Self-Interaction Error, Good Performance for Rydberg and Charge-Transfer States, and Better Performance on Average than B3LYP for Ground States. *J. Phys. Chem. A* **2006,** *110,* 13126-13130.
34. Zhao, Y.; Schultz, N. E.; Truhlar, D. G. Design of Density Functionals by Combining the Method of Constraint Satisfaction with Parametrization for Thermochemistry, Thermochemical Kinetics, and Noncovalent Interactions *J. Chem. Theory Comput.* **2006,** *2,* 364–382.
35. Zhao, Y.; Truhlar, D. G. The M06 suite of density functionals for main group thermochemistry, thermochemical kinetics, noncovalent interactions, excited states, and transition elements: two new functionals and systematic testing of four M06-class functionals and 12 other functionals. *Theor. Chem. Acc.* **2008,** *120,* 215–241.
36. Grimme, S. Accurate description of van der Waals complexes by density functional theory including empirical corrections. *J. Comput. Chem.* **2004,** *25,* 1463–1473.

37. Becke, A. D.; Johnson, E. R. Exchange-hole dipole moment and the dispersion interaction. *J. Chem. Phys.* **2005,** *122,* 154104.
38. Johnson, E. R.; Becke, A. D. A post-Hartree–Fock model of intermolecular interactions. *J. Chem. Phys.* **2005,** *123,* 024101.
39. Marques, M. A. L.; Gross, E. K. U. Time-dependent Density Functional Theory. *Ann. Rev. Phys. Chem.* **2004,** *55,* 427-455.
40. Runge, E.; Gross, E. K. U. Density-Functional Theory for Time-Dependent Systems. *Phys. Rev. Lett.* **1984,** *52,* 997-1000.
41. Jamorski, C.; Casida, M. E.; Salahub, D. R. Dynamic polarizabilities and excitation spectra from a molecular implementation of time-dependent density functional response theory: N_2 as a case study. *J. Chem. Phys.* **1999,** *314,* 291-299.
42. Casida, M. E. Recent Advances in Density Functional Methods. *World Scientific,* Singapore, **1995.**
43. Hirata, S.; Head-Gordon, M. Time-dependent density functional theory within the Tamm-Dancoff approximation. *Chem. Phys. Lett.* **1999,** *314,* 291-299.
44. Peach, M. J. G.; Benfield, P.; Helgaker, T.; Tozer, D. J. Excitation Energies in Density Functional Theory: An Evaluation and a Diagnostic Test. *J. Chem. Phys.* **2008,** *128,* 044118.
45. Gilbert, A. T. B.; Besley, N. A.; Gill, P. M. W. Self-Consistent Field Calculations of Excited States Using the Maximum Overlap Method (MOM). *J. Phys. Chem. A* **2008,** *112,* 13164-13171.
46. Besley, N. A.; Gilbert, A. T. B.; Gill, P. M. W. Self-consistent-field calculations of core excited states *J. Chem. Phys.* **2009,** *130,* 124308.

47. Robinson, D.; Besley, N. A. Modelling the Spectroscopy and Dynamics of Plastocyanin. *Phys. Chem. Chem. Phys.* **2010,** *12*, 9667−9676.

48. Ershova, O. V.; Besley, N. A. Theoretical Calculations of the Excited State Potential Energy Surfaces of Nitric Oxide. *Chem. Phys. Lett.* **2011,** *513*, 179−183.

49. Ziegler, T.; Rauk, A.; Baerends, E. J. Calculation of Mulitplet Energies by Hartree-Fock-Slater Method. *Theor. Chim. Acta* **1977,** *43*, 261−271.

50. Stanton, J. F.; Bartlett, R. J. The equation of motion coupled-cluster method. A systematic biorthogonal approach to molecular excitation energies, transition probabilities, and excited state properties. *J. Chem. Phys.* **1993,** *98*, 7029-7039.

51. Roos, B. O. The CASSCF Method and its Application in Electronic Structure Calculations. *Adv. Chem. Phys.* **1987,** *69*, 399−445.

52. Andersson, K.; Malmqvist, P.-Å; Roos, B. O.; Sadlej, A. J.; Wolinski, K. Second-order perturbation theory with a CASSCF reference function. *J. Phys. Chem.* **1990,** *94*, 5483−5488.

53. Brooks, B. R.; Bruccoleri, R. E.; Olafson, B. D.; States, D. J.; Swaminathan, S.; Karplus, M. CHARMM: A program for macromolecular energy, minimization, and dynamics calculations. *J. Comput. Chem.* **1983,** *4*, 187-217.

54. Weiner, S. J.; Kollman, P. A.; Nguyen, D. T.; Case, D. A. An all atom force field for simulations of proteins and nucleic acids. *J. Comput. Chem.* **1986,** *7*, 230-252.

55. Jorgensen, W. L.; Chandrasekhar, J.; Madura, D.; Impey, R. W.; Klein, M. L. Comparison of simple potential functions for simulating liquid water. *J. Chem. Phys.* **1983,** *79*, 926–935.

56. Schlegel, H. B. *Ab Initio* Molecular Dynamics with Born-Oppenheimer and Extended Lagrangian Methods Using Atom Centered Basis Functions. *Bull. Korean Chem. Soc.* **2003,** *24,* 837-842.
57. Woodcock, H. L.; Hodošček, M.; Gilbert, A. T. B.; Gill, P. M.W.; Schaefer, H. F.; Brooks, B. R. Interfacing Q-Chem and CHARMM to perform QM/MM reaction path calculations. *J. Comput. Chem.* **2007,** *28,* 1485-1502.
58. Haugland R. P. *The Handbook. A guide to Fluorescent Probes and Labelling Technologies,* Invitrogen, Eugene, OR, 10th edn, **2005.**
59. Treibs, A.; Kreuzer, F. H., Difluorboryl Complexes of Di-and Tripyrrylmethene. *Justus Liebigs Ann. Chem.* **1968,** *718,* 208−223.
60. Loudet, A.; Burgess, K. BODIPY Dyes and Their Derivatives: Syntheses and Spectroscopic Properties. *Chem. Rev.* **2007,** *107,* 4891−4932.
61. Benniston, A. C.; Copley, G. Lighting the Way Ahead With Boron Dipyrromethene (Bodipy) Dyes. *Phys. Chem. Chem. Phys.* **2009,** *11,* 4124−4131.
62. Böens, N.; Verbelen, B.; Dehaen, W. Postfunctionalization of the BODIPY Core: Synthesis and Spectroscopy. *Eur. J. Org. Chem.* **2015,** *30,* 6577-6595.
63. Jiao, L.; Yu, C.; Li, J.; Wang, Z.; Wu, M.; Hao, E. β-Formyl-BODIPYs from the Vilsmeier− Haack Reaction. *Eur. J. Org. Chem.* **2009,** *74,* 7525–7528.
64. Jiao, L.; Yu, C.; Liu, M.; Wu, Y.; Cong, K.; Meng, T.; Wang, Y.; Hao, E. Synthesis and Functionalization of Asymmetrical Benzo-Fused BODIPY Dyes. *Eur. J. Org. Chem.* **2010,** *75,* 6035–6038.
65. Yu, C.; Jiao, L.; Yin, H.; Zhou, J.; Pang, W.; Wu, Y.; Wang, Z.; Yang, G.; Hao, E. α-/β-Formylated Boron–Dipyrrin (BODIPY) Dyes: Regioselective Syntheses and Photophysical Properties. *Eur. J. Org. Chem.* **2011,** *28,* 5460–5468.

66. Jiao, L.; Pang, W.; Zhou, J.; Wei, Y.; Mu, X.; Bai, G.; Hao, E. Regioselective Stepwise Bromination of Boron Dipyrromethene (BODIPY) Dyes. *J. Org. Chem.* **2011,** *76*, 9988–9996.

67. Buyukcakir, O.; Bozdemir, O. A.; Kolemen, S.; Erbas, S.; Akkaya, E. U. Tetrastyryl-Bodipy Dyes: Convenient Synthesis and Characterization of Elusive Near IR Fluorophores. *Org. Lett.* **2009,** *11*, 4644–4647.

68. Haefele, A.; Zedde, C.; Retailleau, P.; Ulrich, G.; Ziessel, R. Boron Asymmetry in a BODIPY Derivative. *Org. Lett.* **2010,** *12*, 1672–1675.

69. Bura, T.; Retailleau, P.; Ulrich, G.; Ziessel, R. Highly Substituted Bodipy Dyes with Spectroscopic Features Sensitive to the Environment. *J. Org. Chem.* **2011,** *76*, 1109–1117.

70. Lakshmi, V.; and Ravikanth, M. Synthesis of Sterically Crowded Polyarylated Boron-Dipyrromethenes. *J. Org. Chem.* **2011,** *76*, 8466–8471.

71. Rohand, T.; Baruah, M.; Qin, W.; Böens, N.; Dehaen, W. Functionalisation of fluorescent BODIPY dyes by nucleophilic substitution. *Chem. Commun.* **2006,** *3*, 266–268.

72. Rohand, T.; Qin, W.; Böens, N.; Dehaen, W. Palladium-Catalyzed Coupling Reactions for the Functionalization of BODIPY Dyes with Fluorescence Spanning the Visible Spectrum. Eur. *J. Org. Chem.* **2006,** *20*, 4658–4663

73. Bañuelos, J.; Arroyo-Córdoba, I. J.; Valois-Escamilla, I.; Alvarez-Hernández, A.; Peña-Cabrera, E.; Hu, R.; Tang, B. Z.; Esnal, I.; Martínez, V.; López Arbeloa, I. Modulation of the photophysical properties of BODIPY dyes by substitution at their *meso* position. *RSC Adv.* **2011,** 677–684.

74. Sobenina, L. N.; Vasil'tsov, A. M.; Petrova, O. V.; Petrushenko, K. B.; Ushakov, I. A.; Clavier, G.; Meallet-Renault, R.; Mikhaleva, A. I.; Trofimov, B.

A. General Route to Symmetric and Asymmetric *meso*-CF_3-3(5)-Aryl(hetaryl)- and 3,5-Diaryl(dihetaryl)-BODIPY Dyes. *Org. Lett.* **2011,** *13,* 2524–2527.

75. Awuah, S. G.; Polreis, J.; Biradar, V.; You, Y. Singlet Oxygen Generation by Novel NIR BODIPY Dyes. *Org. Lett.* **2011,** *13,* 3884–3887.
76. Choi, S.; Bouffard, J.; Kim, Y. Aggregation-induced emission enhancement of a *meso*-trifluoromethyl BODIPY *via* J-aggregation. *Chem. Sci.*, **2014,** *5,* 751–755.
77. Schmitt, A.; Hinkeldey, B.; Wild M.; Jung, G. Synthesis of the core compound of the BODIPY dye class: 4,4'-difluoro-4-bora-(3a,4a)-diaza-s-indacene. *J. Fluoresc.* **2009,** *19,* 755–758.
78. Sathyamoorthi, G.; Boyer, J. H.; Allik, T. H.; Chandra, S. Laser active cyanopyrromethene–BF_2 complexes. *Heteroat. Chem.* **1994,** *5,* 403–407.
79. Bañuelos, J.; Martín, V.; Gómez-Durán, C. F.; Arroyo Córdoba, I, J.; Peña-Cabrera, E.; García-Moreno, I.; Costela, A.; Pérez-Ojeda, M. E.; Arbeloa T.; López Arbeloa, I. New 8-Amino-BODIPY Derivatives: Surpassing Laser Dyes at Blue-Edge Wavelengths. *Chem. Eur. J.* **2011,** *17,* 7261–7270.
80. Gómez-Durán, C. F. A.; García-Moreno, I.; Costela, A.; Martín, V.; Sastre, R.; Bañuelos, J.; López Arbeloa, F.; López Arbeloa I.; Peña-Cabrera, E. 8-PropargylaminoBODIPY: unprecedented blue-emitting pyrromethene dye. Synthesis, photophysics and laser properties. *Chem. Commun.* **2010,** *46,* 5103–5105.
81. Osorio-Martínez, C. A.; Urías-Benavides, A.; Gómez-Durán, C. F. A.; Bañuelos, J.; Esnal, I.; López Arbeloa, I.; Peña-Cabrera, E. 8-AminoBODIPYs: Cyanines or Hemicyanines? The Effect of the Coplanarity of the Amino Group on Their Optical Properties. *J. Org. Chem.* **2012,** *77,* 5434−5438.

82. Roacho, R. I.; Metta-Magaña, A.; Portillo, M. M.; Peña-Cabrera, E.; Pannell, K. H. 8-Amino-BODIPYs: Structural Variation, Solvent-Dependent Emission, and VT NMR Spectroscopic Properties of 8-R_2N-BODIPY. *J. Org. Chem.*, **2013,** *78*, 4245–4250.

83. Leen,V.; Yuan, P.; Wang, L.; Böens, N.; Dehaen, W. Synthesis of *Meso*-Halogenated BODIPYs and Access to *Meso*-Substituted Analogues. *Org. Lett.* **2012,** *14*, 6150–6153.

84. Böens, N.; Wang, L.; Leen,V.; Yuan, P.; Verbelen, B.; Dehaen, W.; Van der Auweraer, M.; De Borggraeve, W. D.; Van Meervelt, L.; Jacobs, J.; Beljonne, D.; Tonnelé, C.; Lazzaroni, R.; Ruedas-Rama, M. J.; Orte, A.; Crovetto, L.; Talavera E. M.; Alvarez-Pez, J. M. 8-HaloBODIPYs and Their 8-(C, N, O, S) Substituted Analogues: Solvent Dependent UV–Vis Spectroscopy, Variable Temperature NMR, Crystal Structure Determination, and Quantum Chemical Calculations. *J. Phys. Chem. A*, **2014,** *118*, 1576–1594.

85. Misra, R.; Dhokale, B.; Jadhav, T.; Mobin, S. M. meso-Aryloxy and meso-arylaza linked BODIPY dimers: synthesis, structures and properties. *New. J. Chem.* **2014,** *38*, 3579–3585.

86. Misra, R.; Dhokale, B.; Jadhav, T.; Mobin, S. M. Heteroatom-Connected Ferrocenyl BODIPYs: Synthesis, Structure, and Properties. *Organometallics*, **2014,** *33*, 1867–1877.

87. Wang, L.; Zhang, Y.; Xiao, Y. *meso*-Alkoxy BODIPYs with a good balance between larger Stokes shifts and higher fluorescence quantum yields. *RSC Adv.* **2013,** *3*, 2203–2206.

88. Flores-Rizo, J. O.; Esnal, I.; Osorio-Martínez, C. A.; Gómez-Durán, C. F. A.; Bañuelos, J.; López Arbeloa, I.; Pannell, K. H.; Metta-Magaña, A. J.; Peña-

Cabrera, E. 8-Alkoxy- and 8-Aryloxy-BODIPYs: Straightforward Fluorescent Tagging of Alcohols and Phenols. *J. Org. Chem.* **2013,** *78,* 5867–5877.

89. Zhang, M.; Hao, E.; Xu, Y.; Zhang, S.; Zhu, H.; Wang, Q.; Yu, C.; Jiao, L. One-pot efficient synthesis of pyrrolylBODIPY dyes from pyrrole and acyl chloride. *RSC Adv.* **2012,** *2,* 11215–11218.
90. Bañuelos-Prieto, J.; Agarrabeitia, A. R.; García-Moreno, I.; López-Arbeloa, I.; Costela, A.; Infantes, L.; Perez-Ojeda, M. E.; Palacios-Cuesta, M.; Ortiz, M. J. Controlling Optical Properties and Function of BODIPY by Using Asymmetric Substitution Effects. *Chem. Eur. J.* **2010,** *16,* 14094–14105.
91. Dhokale, B.; Jadhav, T.; Mobin, S. M.; Misra, R. *Meso* enamine substituted BODIPYs. *Chem. Commun.* **2014,** *50,* 9119–9121.
92. Partridge, W. P.; Laurendeau, N. M.; Johnson, C. C.; Steppel, R. N. Performance of Pyrromethene 580 and 597 in a commercial Nd:YAG-pumped dye-laser system. *Opt. Lett.* **1994,** *19,* 1630-1632.
93. Jagtap, K. K.; Maity, D. K.; Ray, A. K.; Dasgupta, K.; Ghosh, S. H. High efficiency dye laser with low fluorescence yield pyrromethene dyes: experimental and theoretical studies. *Appl. Phys. B* **2011,** *103,* 917-924.
94. García-Moreno, I.; Amat-Guerri, F.; Liras, M.; Costela, A.; Infantes, L.; Sastre, R.; López Arbeloa, F.; Bañuelos Prieto, J.; López Arbeloa, I. Structural Changes in the BODIPY Dye PM567 Enhancing the Laser Action in Liquid and Solid Media. *Adv. Funct. Mater,* **2007,** *17,* 3088-3098.
95. Gupta, M.; Kamble, P.; Rath, M. C.; Naik, D. B.; Ray, A. K. High laser efficiency and photostability of pyrromethene dyes mediated by nonpolar solvent. *Appl. Opt.* **2015,** *54,* 7013-7019.

96. Zhang, D.; Martín, V.; García-Moreno, I.; Costela, A.; Pérez-Ojeda, M. E.; Xiao, Y. Development of excellent long-wavelength BODIPY laser dyes with a strategy that combines extending π-conjugation and tuning ICT effect. *Phys. Chem. Chem. Phys.* **2011,** *13,* 13026–13033.
97. Duran-Sampedro, G.; Agarrabeitia, A. R.; Garcia-Moreno, I.; Costela, A.; Bañuelos, J.; Arbeloa, T.; López Arbeloa, I.; Chiara, J. L.; Ortiz, M. J. Chlorinated BODIPYs: Surprisingly Efficient and Highly Photostable Laser Dyes. *Eur. J. Org. Chem.* **2012,** *32,* 6335–6350.
98. Irie, M. Diarylethenes for Memories and Switches. *Chem. Rev.* **2000,** *100,* 1685-1716.
99. Fukaminato, T. Single-molecule fluorescence photoswitching: Design and synthesis of photoswitchable fluorescent molecules. *J. Photochem. Rev.* **2011,** *3*, 177–208.
100. Kollmansberger, M.; Rurack, K.; Resch-Genger, U.; Rettig, W.; Daub, J. Design of an efficient charge-transfer processing molecular system containing a weak electron donor: spectroscopic and redox properties and cation-induced fluorescence enhancement. *Chem. Phys. Lett.* **2000,** *329*, 363-369.
101. Golovkova, T. A.; Kozlov, D. V.; Neckers, D. C. Synthesis and Properties of Novel Fluorescent Switches. *J. Org. Chem.* **2005,** *70*, 5545-5549.
102. Trieflinger, C.; Rurack, K.; Daub, J. "Turn ON/OFF your LOV light": Borondipyrromethene–Flavin Dyads as Biomimetic Switches Derived from the LOV Domain. *Angew. Chem. Int. Ed.* **2005,** *44,* 2288-2291.
103. Li, D.; Zhang, H.; Wang, Y. Four-coordinate organoboron compounds for organic light-emitting diodes (OLEDs). *Chem. Soc. Rev.* **2013,** *42*, 8416-8433.

104. Santra, M.; Moon, H.; Park, M. H.; Lee, T. W.; Kim, Y. K.; Ahn, K. H. Dramatic Substituent Effects on the Photoluminescence of Boron Complexes of 2-(Benzothiazol-2-yl)phenols. *Chem. Eur. J.* **2012,** *18,* 9886–9893.

105. Bozdemir, O. A.; Cakmak, S. E.; Ekiz, O. O.; Dana, A.; Akkaya, E. U. Towards Unimolecular Luminescent Solar Concentrators: Bodipy-Based Dendritic Energy-Transfer Cascade with Panchromatic Absorption and Monochromatized Emission. *Angew. Chem. Int. Ed.* **2011,** *50,* 10907–10912.

106. Spiegel, J. D.; Kleinschmidt, M.; Larbig, A.; Tatchen, J.; Marian, C. M. Quantum-Chemical Studies on Excitation Energy Transfer Processes in BODIPY-Based Donor–Acceptor Systems. *J. Chem. Theor. Comp.* **2015,** *11,* 4316-4327.

107. Erten-Ela, S.; Yilmaz, M. D.; Icli, B.; Dede, Y.; Icli, S.; Akkaya, E. U. A Panchromatic Boradiazaindacene (BODIPY) Sensitizer for Dye-Sensitized Solar Cells. *Org. Lett.* **2008,** *10,* 3299-3302.

108. Hattori, S.; Ohkubo, K.; Urano, Y.; Sunahara, H.; Nagano, T.; Wada, Y.; Tkachenko, N. V.; Lemmetyinen, H.; Fukuzumi, S. Charge Separation in a Nonfluorescent Donor−Acceptor Dyad Derived from Boron Dipyrromethene Dye, Leading to Photocurrent Generation. *J. Phys. Chem. B* **2005,** *109,* 15368-15375.

109. Kamkaew, A.; Lim, S. H.; Lee, H. B.; Kiew, L. V.; Chung, L. Y.; Burgess, K. BODIPY dyes in photodynamic therapy. *Chem. Soc. Rev.* **2013,** *42,* 77-88.

110. Rurack, K.; Trieflinger, C.; Koval'chuck, A.; Daub, J. An Ionically Driven Molecular IMPLICATION Gate Operating in Fluorescence Mode. *Chem. Eur. J.* **2007,** *13,* 8998–9003.

111. Basarić, N.; Baruah, M.; Qin, W.; Metten, B.; Smet, M.; Dehaen, W.; Boens N. Synthesis and spectroscopic characterisation of BODIPY® based fluorescent off–on indicators with low affinity for calcium. *Org. Biomol. Chem.* **2005,** *3,* 2755-2761.

112. Duan, W.; Wei, H.; Cui, T.; Gao, B. A membrane permeable fluorescent Ca2+ probe based on bis-BODIPY with branched PEG. *J. Mater. Chem. B* 2015, *3,* 894-898.

113. Mei, Y.; Bentley, P. A.; Wang, W. A selective and sensitive chemosensor for Cu^{2+} based on 8-hydroxyquinoline. *Tetrahedron Lett.* **2006,** *47,* 2447-2449.

114. Yu, X.; Jia, X.; Yang, X.; Liu, W.; Qin, W. Synthesis and photochemical properties of BODIPY-functionalized silica nanoparticles for imaging Cu^{2+} in living cells. *RSC Adv.* **2014,** *4,* 23571-23579.

115. Que, E. L.; Domaille, D. W.; Chang, C. Metals in Neurobiology: Probing Their Chemistry and Biology with Molecular Imaging. *J. Chem. Rev.* **2008,** *108,* 1517-1549.

116. Kursunlu, A. N.; Deveci, P.; Guler, E. Synthesis and spectroscopic–electrochemical properties of novel ratiometric Hg (II) chemosensor containing Bodipy and the N-phenylaza-15-crown-5 moiety. *J. Luminescence,* **2013,** *136,* 430-436.

117. Xiao, H.; Li, J.; Wu, K.; Yin, G.; Quan, Y.; Wang, R. A turn-on BODIPY-based fluorescent probe for Hg(II) and its biological applications. *Sensor. Actuat. B-Chem.* **2015,** *213,* 343-350.

118. Saha, S. K.; Ghosh, K. R.; Hao, W.; Wang, Z. Y.; Ma, J.; Chiniforooshanb Y.; Bock, W. J. Highly sensitive and selective fluorescence turn-on detection of lead

ion in water using fluorene-based compound and polymer. *J. Mater. Chem. A* **2014,** *2,* 5024-5033.

119. Boens, N.; Leen, V.; Dehaen, W. Fluorescent indicators based on BODIPY. *Chem. Soc. Rev.* **2012,** *41,* 1130-1172.

120. Yin, Z.; Tam, A. Y.; Wong, K. M.; Tao, C.; Li, B.; Poon, C.; Wua, L.; Yam, V. W. Functionalized BODIPY with various sensory units – a versatile colorimetric and luminescent probe for pH and ions. *Dalton Trans.* **2012,** *41,* 11340-11350.

121. Shaw, J.; Epand, R. F.; Epand, R. M.; Li, Z.; Bittman, R.; Yip, C. M. Correlated Fluorescence-Atomic Force Microscopy of Membrane Domains: Structure of Fluorescence Probes Determines Lipid Localization. *Biophys. J.* **2006,** *90,* 2170-2178.

122. Karolin, J.; Johansson, L. B. Å.; Strandberg, L.; Ny, T. Fluorescence and Absorption Spectroscopic Properties of Dipyrrometheneboron Difluoride (BODIPY) Derivatives in Liquids, Lipid Membranes, and Proteins. *J. Am. Chem. Soc.* **1994,** *116,* 7801-7806.

123. Bergström, F.; Hägglöf, P.; Karolin, J.; Ny, T.; Johansson L. B. A. The use of site-directed fluorophore labeling and donor–donor energy migration to investigate solution structure and dynamics in proteins. *Proc. Natl. Acad. Sci. U.S.A.* **1999,** *96,* 12477-12481.

124. Yee, M.; Fas, S. C.; Stohlmeyer, M. M.; Wajndless, T. J.; Cimprich, K. A. A cell-permeable, activity-based probe for protein and lipid kinases. *J. Biol. Chem.* **2005,** *280,* 29053-29059.

125. Ehrenschwender, T.; Wagenknecht, H. Synthesis and Spectroscopic Characterization of BODIPY-Modified Uridines as Potential Fluorescent Probes for Nucleic Acids. *Synthesis* **2008,** *22*, 3657-3662.

126. Li, Z.; Mintzer, E.; Bittman, R. First Synthesis of Free Cholesterol−BODIPY Conjugates. *J. Org. Chem.* **2006,** *71,* 1718-1721.

127. Hölttä-Vuori, M.; Uronen, R.-L.; Repakova, J.; Salonen, E.; Vattulainen, I.; Panula, P.; Li, Z.; Bittman, R.; Ikonen, E. BODIPY-Cholesterol: A New Tool to Visualize Sterol Trafficking in Living Cells and Organisms. *Traffic,* **2008,** *9,* 1839–1849.

128. Marks, D. L.; Bittman, R.; Pagano, R. E. Use of Bodipy-labeled sphingolipid and cholesterol analogs to examine membrane microdomains in cells. *Histochem. Cell Biol.* **2008,** *130,* 819-832.

129. Emmerson, P. J.; Archer, S.; El-Hamouly, W.; Mansour, A.; Akil, H.; Medzihradsky, F. Synthesis and characterization of 4,4-difluoro-4-bora-3a,4a-diaza-s-indacene (BODIPY)-labeled fluorescent ligands for the mu opioid receptor. *Biochem. Pharmacol.* **1997,** *54,* 1315-1322.

130. Zhang, X.; Xiao, Y.; Qi, J.; Qu, J.; Kim, B.; Yue, X.; Belfield, K. D. Long-Wavelength, Photostable, Two-Photon Excitable BODIPY Fluorophores Readily Modifiable for Molecular Probes. *J. Org. Chem.* **2013,** *78,* 9153–9160.

131. Zhang, X.; Wang, C.; Jin, L.; Han, Z.; Xiao, Z. Photostable Bipolar Fluorescent Probe for Video Tracking Plasma Membranes Related Cellular Processes. *ACS Appl. Mater. Interfaces,* **2014,** *6,* 12372–12379.

132. Işit, M.; Guliyev, R.; Kolemen, S.; Altay, Y.; Senturk, B.; Tekinay, T.; Akkaya, E. U. Designing an Intracellular Fluorescent Probe for Glutathione: Two

Modulation Sites for Selective Signal Transduction. *Org. Lett.* **2014,** *16,* 3260–3263.

133. Ferguson, C. G.; Bigman, C. S.; Richardson, R. D.; van Meeteren, L. A.; Moolenar, W. H.; Prestwich, G. D. Fluorogenic Phospholipid Substrate to Detect Lysophospholipase D/Autotaxin Activity. *Org. Lett.* **2006,** *8,* 2023-2026.
134. Wagner, R. W.; Lindsey, J. S. Boron-dipyrromethene dyes for incorporation in synthetic multi-pigment light-harvesting arrays. *Pure Appl. Chem.* **1996,** *68,* 1373-1380.
135. El-Khouly, M. E.; Fukuzumi, S.; D'Souza, F. Photosynthetic Antenna–Reaction Center Mimicry by Using Boron Dipyrromethene Sensitizers. *Chem. Phys. Chem.* **2014,** *15,* 30–47.
136. Boens, N.; Leen, V.; Dehaen, W.; Wang, L.; Robeyns, K.; Qin, W.; Tang, X.; Beljonne, D.; Tonnelé, C.; Paredes, J. M.; Ruedas-Rama, M. J.; Orte, A.; Crovetto, L.; Talavera, E. M.; Alvarez-Pez, J. M. Visible Absorption and Fluorescence Spectroscopy of Conformationally Constrained, Annulated BODIPY Dyes. *J. Phys. Chem. A* **2012,** *116,* 9621-9631.
137. López Arbeloa, F.; López Arbeloa, T.; López Arbeloa, I.; García-Moreno, I.; Costela, A.; Sastre, R.; Amat-Guerri, F. Photophysical and lasing properties of pyrromethene 567 dye in liquid solution.: Environment effects. *Chem. Phys.* **1998,** *236,* 331-341.
138. Catalán, J. Toward a Generalized Treatment of the Solvent Effect Based on Four Empirical Scales: Dipolarity (SdP, a New Scale), Polarizability (SP), Acidity (SA), and Basicity (SB) of the Medium. *J. Phys. Chem. B,* **2009,** *113,* 5951–5960.

139. Filarowski A.; Kluba M.; Cieślik-Boczula, K.; Koll, A.; Kochel, A.; Pandey, L.; De Borggraeve, W. M.; Van der Auweraer, M.; Catalán, J.; Boens, N. Generalized solvent scales as a tool for investigating solvent dependence of spectroscopic and kinetic parameters. Application to fluorescent BODIPY dyes. *Photochem. Photobiol. Sci.* **2010,** *9,* 996–1008.

140. Lee, J-S.; Kang, N-Y.; Kim, Y. K.; Samanta, A.; Feng, S.; Kim, H. K.; Vendrell, M.; Park, J. H.; Chang, Y-T. Synthesis of a BODIPY Library and Its Application to the Development of Live Cell Glucagon Imaging Probe. *J. Am. Chem. Soc.* **2009,** *131,* 10077-10082.

141. Gabe, Y.; Urano, Y.; Kikuchi, K.; Kojima, H.; Nagano, T. Highly Sensitive Fluorescence Probes for Nitric Oxide Based on Boron Dipyrromethene Chromophore - Rational Design of Potentially Useful Bioimaging Fluorescence Probe. *J. Am. Chem. Soc.* **2004,** *126,* 3357-3367.

142. Prieto, J. B.; López Arbeloa, F.; Martínez Martínez, V.; López Arbeloa, T.; López Arbeloa, I. Structural and spectroscopic characteristics of Pyrromethene 567 laser dye. A theoretical approach. *Phys. Chem. Chem. Phys.* **2004,** *6,* 4247-4253.

143. Ma, C.; Liang, W.; Jiang, D.; Hong, Z.; Qing, L.; Yan, Y. Theoretical study of the photophysical and charge transport properties of novel fluorescent fluorine–boron compounds. *Mol. Phys.* **2010,** *108,* 667-674.

144. Laurent, A. D.; Adamo, C.; Jacquemin, D. Dye chemistry with time-dependent density functional theory. *Phys. Chem. Chem. Phys.* **2014,** *16,* 14334-14356.

145. Chibani, S.; Le Guennic, B.; Charaf-Eddin, A.; Laurent, A. D.; Jacquemin, D. Revisiting the optical signatures of BODIPY with *ab initio* tools. *Chem. Sci.* **2013,** *4,* 1950-1963.

146. Mukherjeea, S.; Thilagar, P. Effect of alkyl substituents in BODIPYs: a comparative DFT computational investigation. *RSC Adv.* **2015,** *5,* 2706-2714.

147. Chibani, S.; Jacquemin, D.; Laurent, A. D.Modelling solvent effects on the absorption and emission spectra of constrained cyanines with both implicit and explicit QM/EFP models. *Comput. Theor. Chem.* **2014,** *1040,* 321-327.

148. Le Guennic, B.; Jacquemin, D. Taking Up the Cyanine Challenge with Quantum Tools. *Acc. Chem. Res.* **2015,** *48,* 530–537.

149. Le Guennic, B.; Maury, O.; Jacquemin, D. Aza-boron-dipyrromethene dyes: TD-DFT benchmarks, spectral analysis and design of original near-IR structures. *Phys Chem. Chem. Phys.* **2012,** *14,* 157-164.

150. Robinson, D.; Besley, N. A.; Lunt, E. A. M.; O'Shea, P.; Hirst, J. D. Electronic structure of 5-hydroxyindole: from gas-phase to explicit solvation. *J. Phys. Chem. B* **2009,** *113,* 2535-2541.

151. Robinson, D.; Besley, N. A.; O'Shea P.; Hirst, J. D. Calculating the fluorescence of 5-hydroxytryptophan in proteins. *J. Phys. Chem. B* **2009,** *113,* 14521-14528.

152. Robinson, D.; Besley, N. A.; O'Shea P.; Hirst, J. D. Di-8-ANEPPS Emission Spectra in Phospholipid / Cholesterol Membranes: A Theoretical Study. *J. Phys. Chem. B* **2011,** *115,* 4160-4167.

153. Barucha-Kraszewska, J.; Kraszewski, S.; Jurkiewicz, P.; Ranseyer, C.; Hof, M. Numerical studies of the membrane fluorescent dyes dynamics in ground and excited states. *Biochimica et Biophysica acta* **2010,** *1798,* 1724-1734.

154. Baruah, M.; Qin, W.; Flors, C.; Hofkens, J.; Vallée, R. A. L.; Beljonne, D.; Van der Auweraer, M.; De Borggraeve, W. M.; Boens, N. Solvent and pH

Dependent Fluorescent Properties of a Dimethylaminostyryl Borondipyrromethene Dye in Solution. *J. Phys. Chem. A* **2006,** *110,* 5998−6009.

155. Qin, W.; Rohand, T.; Dehaen, W.; Clifford, J. N.; Driesen, K.; Beljonne, D.; Van Averbeke, B.; Van der Auweraer, M.; Boens, N. Boron Dipyrromethene Analogs with Phenyl, Styryl, and Ethynylphenyl Substituents: Synthesis, Photophysics, Electrochemistry, and Quantum-Chemical Calculations. *J. Phys. Chem. A* **2007,** *111,* 8588–8597.

156. Qin, W.; Leen, V.; Rohand, T.; Dehaen, W.; Dedecker, P.; Van der Auweraer, M.; Robeyns, K.; Van Meervelt, L.; Beljonne, D.; Van Averbeke, B.; Clifford, J. N.; Driesen, K.; Binnemans, K.; Boens, N. Energetic and Electronic Structure Analysis of Intrinsic Defects in SnO_2. *J. Phys. Chem. A* **2009,** *113,* 439–447.

157. Qin, W.; Leen, V.; Dehaen, W.; Cui, J.; Xu, C.; Tang, X.; Liu, W.; Rohand, T.; Beljonne, D.; Van Averbeke, B.; Clifford, J. N.; Driesen, K.; Binnemans, K.; Van der Auweraer, M.; Boens, N. 3,5-Dianilino Substituted Difluoroboron Dipyrromethene: Synthesis, Spectroscopy, Photophysics, Crystal Structure, Electrochemistry, and Quantum-Chemical Calculations. *J. Phys. Chem. C* **2009,** *113,* 11731–11740.

158. Röhrig, U. F.; Frank, I.; Huttler, J.; Laio, A.; VandeVondele, J.; Rothlisberger, U. QM/MM Car-Parrinello Molecular Dynamics Study of the Solvent Effects on the Ground State and on the First Excited Singlet State of Acetone in Water. *Chem. Phys. Chem.* **2003,** *4,* 1177-1182.

159. Langer, H.; Doltsinis, N. L.; Marx, D. Excited-state dynamics and coupled proton-electron transfer of guanine. *Chem. Phys. Chem.* **2005,** *6,* 1734-1737.

160. Frank, I.; Damianos, K. Excited state dynamics in pyrrole–water clusters: First-principles simulation. *Chem. Phys.* **2008,** *343,* 347-352.

161. Lu, H.; Zhang, S.; Liu, H.; Wang, Y.; Shen, Z.; Liu, C.; You, X. Experimentation and Theoretic Calculation of a BODIPY Sensor Based on Photoinduced Electron Transfer for Ions Detection. *J. Phys. Chem. A* **2009,** *113,* 14081-14086.

162. Heradón, B.; Chana, A.; Alonso, M.; Amat-Guerri, F.; Liras, M.; Maestro, M. A. 8-Aryl substituted boron-dipyrromethene dyes: crystal structures and computational studies. *J. Mol Struct.* **2004,** *697,* 29-40.

163. Meyer, J.; Wadewitz, A.; Lokamani; Toher, C.; Gresser, R.; Leo, K.; Riede, M.; Moresco, F.; Cuniberti, G. Molecules for organic electronics studied one by one. *Phys. Chem. Chem. Phys.* **2011,** *13,* 14421-14426.

164. Widmark, P.-O.; Malmqvist, P.-Å.; Roos, B. O. Density matrix averaged atomic natural orbital (ANO) basis sets for correlated molecular wave functions. *Theor. Chim. Acta* **1990,** *77,* 291-306.

165. Karlström, G.; Lindh, R.; Malmqvist, P.-Å; Roos, B. O.; Ryde, U.; Veryazov, V.; Widmark, P.-O.; Cossi, W.; Schimmelpfennig, B.; Neogrády, P. Seijo, L. MOLCAS: a program package for computational chemistry. *Comp. Mater. Sci.* **2003,** *28,* 222-239.

166. Arroyo, I. J.; Hu, R.; Merino, G.; Tang, B. Z.; Peña-Cabrera, E. J. Org. Chem. 2009, 74, 5719–5722.

167. Tram, K.; Yan, H.; Jenkins, H.A.; Vassiliev, S.; Bruce, D. The synthesis and crystal structure of unsubstituted 4,4-difluoro-4-bora-3a,4a-diaza-s-indacene (BODIPY). *Dyes Pigm.* **2009,** *82,* 392–395.

168. Hudgins, P.M.; Weiss, G.B. *J.* Differential effects of calcium removal upon vascular smooth muscle contraction induced by norepinephrine, histamine and potassium. *Pharmacol. Exo. Ther.,* **1968,** *159,* 91-97.

169. Kofuji, P; Newman, E.A. Potassium buffering in the central nervous system. *Neuroscience,* **2004,** *129,* 1043-1054.

170. Stanton, B.A.; Biemesderfer, D.; Wade, J.B.; Giebisch, G. Structural and functional study of the rat distal nephron: Effects of potassium adaptation and depletion. *Kidney Int.,* **1981,** *19,* 36-48.

171. Gadsby, D. C.; Niedergerke, R.; Page, S. Do Intracellular Concentrations of Potassium or Sodium Regulate the Strength of the Heart Beat? *Nature,* **1971,** *232,* 651-653.

172. Mitchell, J.E.; Pyle, R.L.; Eckert, E.D.; Hatsukami, D.; Lentz, R. Electrolyte and other physiological abnormalities in patients with bulimia. *Psychol. Med.,* **1983,** *13,* 273-278.

173. MacGregor, L.C.; Matschinsky, F.M. Altered Retinal Metabolism in Diabetes. *J. Biol. Chem.,* **1986,** *261,* 4052-4058.

174. Frant, M. S.; Ross, J. W. Potassium ion specific electrode with high selectivity for potassium over sodium. *Science,* **1970**, *167,* 987-988.

175. Rurack, K. Flipping the light switch 'ON' – the design of sensor molecules that show cation-induced fluorescence enhancement with heavy and transition metal ions. *Spectrochim. Acta A,* **2001,** *57,* 2161-2195.

176. de Silva, A.P.; Gunaratne, H.Q.N.; Gunnlaugsson, T.; Huxley, A.J.M.; McCoy, C.P.; Rademacher, J.T.; Rice, T.E. Signaling Recognition Events with Fluorescent Sensors and Switches. *Chem. Rev.,* **1997,** *97,* 1515-1566.

177. Meuwis, K.; Boens, N.; De Schryver, F. C.; Gallay, J.; Vincent, M. Photophysics of the Fluorescent K^+ Indicator PBFI. *Biophys. J.,* **1995,** *68,* 2469-2473.

178. Jezek, P.; Mahdi, F.; Garlid, K. D. Reconstitution of the beef heart and rat liver mitochondrial K^+/H^+ (Na^+/H^+) antiporter. Quantitation of K^+ transport with the novel fluorescent probe, PBFI. *J. Biol. Chem.* **1990,** *265,* 10522-10526.

179. He, H.; Mortellaro, M. A.; Leiner, M. J. P.; Fraatz, R. J.; Tusa, J. K. A fluorescent sensor with high selectivity and sensitivity for potassium in water. *J. Am. Chem. Soc.* **2003,** *125,* 1468-1469.

180. Fan, L.-J.; Zhang, Y.; Murphy, C. B.; Angell, S. E.; Parker, M. F. L.; Flynn, B. R.; Jones, W. E. Fluorescent Conjugated Polymer Molecular Wire Chemosensors for Transition Metal Ion Recognition and Signaling. *Coord. Chem. Rev.* **2009,** *253,* 410−422.

181. Keawwangchai, T.; Morakot, N.; Wanno, B. Fluorescent Sensors Based on BODIPY Derivatives for Aluminium Ion Recognition: An Experimental and Theoretical Study. *J. Mol. Model.* **2013,** *19,* 1435−1455.

182. Werner, H.-J.; Knowles, P. J. An Efficient Internally Contracted Multiconfiguration Reference Configuration Interaction Method. *J. Chem. Phys.* **1988,** *89,* 5803−5814.

183. Celani, P.; Werner, H.-J. Multireference Perturbation Theory for Large Restricted and Selected Active Space Reference Wave Functions. *J. Chem. Phys.* **2000,** *112,* 5546−5557.

184. M.; Suwinska, K.; Eichen, Y. Sensitive and Selective PET-Based Diimidazole Luminophore for Zn^{II} Ions: A Structure−Activity Correlation. *Inorg. Chem.* **2006,** *45,* 5315−5320.

185. Bañuelos, J.; López Arbeloa, F.; Arbeloa, T.; Salleres, S.; Amat-Guerri, F.; Liras, M.; López Arbeloa, I. Photophysical Study of New Versatile

Multichromophoric Diads and Triads with BODIPY and Polyphenylene Groups. *J. Phys. Chem. A* **2008,** *112,* 10816−10822.

186. Lee, H.; Hancock, R. D.; Lee, H.-S. Role of Fluorophore-Metal Interaction in Photoinduced Electron Transfer (PET) Sensors: Time-Dependent Density Functional Theory (TDDFT) Study. *J. Phys. Chem. A* **2013,** *117,* 13345−13355.

187. Hehre, W. J.; Ditchfield, R.; Pople, J. A. Self-Consistent Molecular Orbital Methods. XII. Further Extensions of Gaussian-Type Basis Sets for use in Molecular Orbital Studies of Organic Molecules. *J. Chem. Phys.* **1972,** *56,* 2257−2261.

188. Rassolov, V.; Pople, J. A.; Ratner, M.; Windus, T. L. 6-31G* Basis Set for Atoms K Through Zn. *J. Chem. Phys.* **1998,** *109,* 1223−1229.

189. Becke, A. A new mixing of Hartree–Fock and local density-functional theories *J. Chem. Phys.,* **1993,** *98,* 1372.

190. Ershova, O. V.; Besley, N. A. Can Density Functional Theory Describe the NO($X^2\Pi$)-Ar and NO($A^2\Sigma^+$)-Ar Van der Waals Complexes? *J. Chem. Phys.* **2012,** *136,* No. 244313.

191. Hanson-Heine, M. W. D.; George, M. W.; Besley, N. A. Calculating Excited State Properties Using Kohn-Sham Density Functional Theory. *J. Chem. Phys.* **2013,** *138,* No. 064101.

192. Shao, Y.; Gan, Z.; Epifanovsky, E.; Gilbert, A. T. B.; Wormit, M.; Kussmann, J.; Lange, A. W.; Behn, A.; Deng, J.; Feng, X.; et al. Advances in Molecular Quantum Chemistry Contained in the QChem 4 Program Package. *Mol. Phys.* **2015,** *113,* 184−215.

193. Briggs, E. A.; Besley, N. A.; Robinson, D. QM/MM Excited State Molecular Dynamics and Fluorescence Spectroscopy of BODIPY. *J. Phys. Chem. A* **2013,** *117,* 2644−2650.

194. Marcus, R. A. On the Theory of Oxidation-Reduction Reactions Involving Electron Transfer. V. Comparison and Properties of Electrochemical and Chemical Rate Constants. *J. Phys. Chem.* **1963,** *67,* 853−857.

195. Marcus, R. A.; Sutin, N. Electron Transfers in Chemistry and Biology. *Biochim. Biophys. Acta* **1985,** *811,* 265−322.

196. Hsu, C.-P. The Electronic Couplings in Electron Transfer and Excitation Energy Transfer. *Acc. Chem. Res.* **2009,** *42,* 509−518.

197. Subotnik, J. E.; Vura-Weis, J.; Sodt, A. J.; Ratner, M. A. Predicting Accurate Electronic Excitation Transfer Rates via Marcus Theory with Boys or Edmiston-Ruedenberg Localized Diabatization. *J. Phys. Chem. A* **2010,** *114,* 8665−8675.

198. Manna, A. K.; Dunietz, B. D. Communication: Charge-Transfer Rate Constants in Zinc-Porphyrin-Porphyrin-Derived Dyads: A Fermi Golden Rule First-Principles-Based Study. *J. Chem. Phys.* **2014,** *141,* No. 121102.

199. Kristyan, S.; Pulay, P. Can (semi)local density functional theory account for the London dispersion forces? *Chem. Phys. Lett.* **1994,** *229,* 175–180.

200. Hobza, P; Sponer, J.; Reschel, T. Density functional theory and molecular clusters. *J. Comput. Chem.* **1995,** *16,* 1315–1325.

201. Perez-Jorda, J. M.; and Becke, A. D. A density-functional study of van der Waals forces: rare gas diatomics *Chem. Phys. Lett.* **1995,** *233,* 134–137.

202. Sinnokrot, M. O.; Sherrill, C. D. High-Accuracy Quantum Mechanical Studies of π-π Interactions in Benzene Dimers *J. Phys. Chem. A* **2006,** *110,* 10656–10668.

203. Jurecka, P.; Sponer, J.; Cerny, J.; Hobza, P. Benchmark database of accurate (MP2 and CCSD(T) complete basis set limit) interaction energies of small model complexes, DNA base pairs, and amino acid pairs *Phys. Chem. Chem. Phys.* **2006,** *8,* 1985–1993.

204. Morgado, C. A.; Jurecka, P.; Svozil, D.; Hobza, P.; Sponer, J. Reference MP2/CBS and CCSD(T) quantum-chemical calculations on stacked adenine dimers. Comparison with DFT-D, MP2.5, SCS(MI)-MP2, M06-2X, CBS(SCS-D) and force field descriptions *Phys. Chem. Chem. Phys.* **2010,** *12,* 3522–3534.

205. von Lilienfeld, O. A.; Tavernelli, I.; Röthlisberger, U.; Sebastiani, D. Optimization of Effective Atom Centered Potentials for London Dispersion Forces in Density Functional Theory *Phys. Rev. Lett.* **2004**, *93,* 153004.

206. Grimme, S.; Antony, J.; Schwabe, T.; Mück-Lichtenfeld, C. Density functional theory with dispersion corrections for supramolecular structures, aggregates, and complexes of (bio)organic molecules *Org. Biomol. Chem.* **2007,** *5,* 741–758.

207. Foster, M. E.; Sohlberg, K. Empirically corrected DFT and semi-empirical methods for non-bonding interactions *Phys. Chem. Chem. Phys.* **2010,** *12,* 307–322.

208. Grimme, S. Density functional theory with London dispersion corrections. *Comput. Mol. Sci.*, **2011,** *1,* 211–228.

209. Dion, M.; Rydberg, H.; Schröder, E.; Langreth, D. C.; Lundqvist, B. I. Van der Waals Density Functional for General Geometries *Phys. Rev. Lett.* **2004,** *92,* 246401.

210. Grimme, S. Semiempirical hybrid density functional with perturbative second-order correlation *J. Chem. Phys.* **2006,** *124,* 034108.

211. Vydrov, O. A.; van Voorhis, T. Nonlocal van der Waals Density Functional Made Simple *Phys. Rev. Lett.* **2009,** *103,* 063004.

212. Tkatchenko, A.; Scheffler, M. Accurate Molecular Van Der Waals Interactions from Ground-State Electron Density and Free-Atom Reference Data *Phys. Rev. Lett.* **2009,** *102,* 073005.

213. Marom, N.; Tkatchenko, A.; Rossi, M.; Gobre, V. V.; Hod, O.; Scheffler, M.; Kronik, L. Dispersion Interactions with Density-Functional Theory: Benchmarking Semiempirical and Interatomic Pairwise Corrected Density Functionals *J. Chem. Theory Comput.* **2011,** *7,* 3944–3951.

214. Elstner, M.; Hobza, P.; Frauenheim, T.; Suhai, S.; Kaxiras, E. Hydrogen bonding and stacking interactions of nucleic acid base pairs: A density-functional-theory based treatment *J. Chem. Phys.* **2001,** *114,* 5149–5155.

215. Wu, Q.; Yang, W. Towards extending the applicability of density functional theory to weakly bound systems *J. Chem. Phys.* **2001,** *115,* 8748–8757.

216. Zimmerli, U.; Parrinello, M.; Koumoutsakos, P. Dispersion corrections to density functionals for water aromatic interactions *J. Chem. Phys.* **2004,** *120,* 2693–2699.

217. Jurecka, P.; Cerny, J.; Hobza, P.; Salahub, D. Density functional theory augmented with an empirical dispersion term. Interaction energies and geometries of 80 noncovalent complexes compared with *ab initio* quantum mechanics calculations *J. Comput. Chem.* **2007,** *28,* 555–569.

218. Becke, A. D.; Kannemann, F. O. Nonempirical density-functional theory for van der Waals interactions *Can. J. Chem.* **2010,** *88,* 1057–1062.

219. Kannemann, F. O.; Becke, A. D. van der Waals Interactions in Density-Functional Theory: Intermolecular Complexes *J. Chem. Theory Comput.* **2010,** *6*, 1081–1088.

220. Fukuda, R.; Ehara, M. Properties of liquid clusters in large-scale molecular dynamics nucleation simulations. *J. Chem. Phys.* ***2013,*** *139*, 074303.

221. Ershova, O. V.; Klos, J.; Harris, J. P.; Gardner, A. M.; Tamé-Reyes, V. M.; Andrejava, A.; Alexander, M. H.; Besley, N. A.; Wright, T. G. Interaction of the NO 3pπ Rydberg state with Ar: Potential energy surfaces and spectroscopy *J. Chem. Phys.* **2013,** *138*, 214313.

222. Halkier, A.; Helgaker, T.; Jørgensen, P.; Klopper, W.; Koch, H.; Olsen, J.; Wilson, A. K. Basis-set convergence in correlated calculations on Ne, N_2, and H_2O *Chem. Phys. Lett.* **1998,** *286*, 243–252.

223. Perdew, J. P.; Burke, K.; Ernzerhof, M. Generalized Gradient Approximation Made Simple *Phys. Rev. Lett.* **1997,** *78*, 1396.